Fusion-fission studies of compound nuclei around mass 215

Thesis submitted to the University of Calicut for the award of the Degree of

Doctor of Philosophy in Physics

by

Jagdish Gehlot

Under the guidance of

Prof. A M Vinodkumar

Department of Physics
University of Calicut, Calicut

July 2019

UNIVERSITY OF CALICUT
DEPARTMENT OF PHYSICS
Calicut University P.O. Malappuram (Dt.), Kerala, India - 673635

Dr. A. M. VINODKUMAR
Professor & Head

Tel : 0494 – 2407415, 416
Mobile: 9645078924
Email : amv@uoc.ac.in,
phyhod@uoc.ac.in

19th February 2020

CERTIFICATION OF SUPERVISOR

This is to certify that all the corrections/suggestions from the adjudicators have been incorporated in this thesis.

Calicut University

Prof. (Dr.) A. M. Vinodkumar

CERTIFICATE

This is to certify that the thesis entitled **Fusion-fission studies of compound nuclei around mass 215**, is a record of bonafide research work carried out by Mr. Jagdish Gehlot under my guidance, at Department of Physics, University of Calicut and IUAC, New Delhi. No part of the work reported in this thesis has been presented for the award of any degree from any institution.

Prof. A M Vinodkumar

Dedicated to
My Teachers,
Family & Friends

DECLARATION

I hereby declare that this thesis entitled **Fusion-fission studies of compound nuclei around mass 215** is a bonafide record of research work carried out by me under the guidance of Dr. A.M. Vinodkumar (Professor, Department of Physics, University of Calicut) and that no part of this thesis has been presented before the award of any other degree or diploma.

Calicut University Jagdish Gehlot

Date:

Abstract

Evaporation residue cross sections for the ^{16}O + ^{203}Tl and ^{16}O + ^{205}Tl reactions were measured at laboratory energies in the range of 82-113 MeV using the HYbrid Recoil mass Analyzer (HYRA) at IUAC, New Delhi. Transmission efficiency of the separator was estimated using a calibration reaction ^{16}O + ^{197}Au and by simulating the evaporation residues angular distributions. Statistical model calculations were performed for both the measured systems using HIVAP. These calculations overestimate the experimental evaporation residue cross sections. This could be attributed to the presence of non compound nuclear fission. An estimation of non compound nuclear fission contribution was carried out. Comparison with neighboring systems shows that a slight change in the entrance channel or the compound nucleus properties makes a large difference in evaporation residue cross sections.

Acknowledgments

I feel myself privileged to thank my thesis supervisor Prof. A. M. Vinodkumar for his guidance, patience and able help throughout the tenure of my thesis work. His ideas and enthusiasm towards the Nuclear Physics have always been a source of inspiration for me. The discussion with him always paved me a way to cross the hurdles related to my research work.

I would like to express my gratitude to Dr. N. Madhavan for the support and encouragement he provided ever since I joined IUAC. The knowledge about the experimental Nuclear Physics, Mass separators, the data analysis and his valuable suggestions have always helped me to gain in depth understanding of the subject all these years.

I would like to express my gratitude towards Dr. S. Nath for his help in making me learn the data analysis as well as experimental techniques. I am thankful to him for the fruitful discussions we had. His consistent motivation to successfully complete this thesis is also acknowledged.

Dr. A. Jhingan's guidence in the development and learning of various detector systems, especially the multi wire proportional counter and associated electronics is gratefully acknowledged. I owe all my knowledge about detectors and data acquisition to him.

The technical support received form Mr. T. Varughese had been a key to the successful and timely setting up of the experimental facilities. His help with the technical drawings and mechanical setups is gratefully acknowledged.

I would like to thank Prof. A. V. Yeremin for giving me a chance to visit FLNR, Dubna and work there during the testing of the separator SHELLS. This gave me the chance to have an exposure of the contemporary measurement techniques.

I am indebted to Dr. A. K. Sinha for intense discussions and valuable suggestions during the course of this work. His words of encouragement have always motivated me to perform better.

I am indebted to Prof. B. R. S. Babu for the critical reading of the manuscripts and for the fruitful discussions about the interpretation of the results.

I thank all the faculties and staff members of Department of Physics, University of Calicut for their help and encouragement.

My sincere thanks to Mr. S. R. Abhilash for his help and support in the target fabrication. I am thankful for the timely help received from Mr. S. Ojha and Prof. D. Mehta in target characterizations.

I would like to thank my collaborators Prof. I. Mazumdar, Mr. V. I. Chepigin and Mr. L. Chelnokov for their active participation in the experiment.

Help received from Dr. T. Banerjee, Mr. M. M. Hosamani, Dr. A. Shamlath, Mr. P.

V. Laveen, Mr. M. Shareef, Ms. P. Jisha, Ms. P. Sandya Devi and Ms. G. Naga Jyothi are acknowledged for their support during the beam time.
The help received from Mr. E. T. Subramaniyam, Mrs. Kusum Rani, Mr. S. Venkataramanan and Mrs. Arti Gupta regarding the nuclear electronics is thankfully acknowledged.
I would like to thank Dr. A. Roy, Dr. D. Kanjilal and Prof. A. C. Pandey for their encouragement and cooperation to continue my research work.
I take this opportunity to thank my senior colleagues Dr. S. Chopra, Dr. P. Sugathan, Dr. S. Murlithar, Dr. R. P. Singh, Dr. Rakesh Kumar and Mrs. K. S. Golda for their help at different stages of my work.
The accelerator user committee of IUAC, New Delhi is thankfully acknowledged for allotting me beam time to perform the experiments.
I would like to thank the staff of the vacuum laboratory, the target laboratory, the data support laboratory, the beam transport laboratory and the IUAC workshop for their timely support related to my experiments in different ways which has led to the successful completion of my research work. The operating staff of IUAC pelletron are gratefully acknowledged for the smooth operation of the accelerator during the experiments.
Needless is to mention the moral support of Dr. E. Prasad throughout this work. The scientific discussions with him as well as his constant encouragement are thankfully acknowledged.
The unconditional friendship of Mr. M. P. Dabi, Mr. Vikram Jani, Mr. Yogesh Muleva, Mr. Ashutosh Rai, Mr. Yashwant Sharma, Dr. Krishna Kumar Pandey and Mr. P. Patra has always been a source of inspiration for me. I always cherish their heartening company.
The perpetual help, support and encouragement received from my family members have been a driving force for me throughout my life and especially during these years of my PhD life. I thank my parents, my in-laws and my wife for their constant support, without that it was never possible to complete this endeavor and to my lovely daughter *Gauri*, who has been a constant motivation to me for completing this project.
At last, I would like to thank the almighty for making me able to successfully complete this endeavor.

Contents

List of Figures

List of Tables

Chapter 1

Introduction

The invention of particle accelerators has been a turning point in the nuclear physics research. In its early days, the nuclear physics research was focused at studying the ground state properties of the nuclei. The nuclear reactions would in general involve the lighter particles like neutron, proton etc. as projectile. With the invention of heavy particle accelerators, it was possible to populate and study the nuclei with higher excitation and angular momenta. With energetic heavy ions from these accelerators, one could produce the nuclei beyond naturally available stable nuclei via nuclear fusion reactions. Heavy ion fusion reactions are particularly important as they are the most successful mechanisms for superheavy element (SHE) production [1–3].

Heavy ion fusion-fission reaction dynamics has been an active field of study for the past several decades and it still has surprises, especially for the heavier nuclei (A $\geq$200 amu) around the barrier. With the increasing mass, energy and angular momenta, the nuclear reaction dynamics changes dramatically. In heavier mass region the reaction mechanism is no more a simple fusion of the nuclei and their fission into nearly equal masses. There exists the non-compound nuclear processes like quasifission, fast fission etc. which reduce the probability of complete fusion. At the same time there are non conclusive evidences suggesting the effect of shell closures (proton or neutron) on reaction dynamics. This makes the reaction dynamics in heavy mass region an interesting subject.

1.1 Nuclear reactions

Two nuclei in the vicinity of each other, experience an interaction potential which has an outer repulsive barrier and an inner attractive core. If the projectile has a sufficient energy to overcome the repulsive barrier, it can fuse and later it can decay via various decay modes. A nuclear reaction in general can be represented as $A(a,b)B$ or $a + A \rightarrow$

$B + b$, where a and A are the projectile and the target respectively. b and B are the ejected particle and the residual nucleus respectively. There could be possibly multiple exit channels after the collision.

Heavy ion collisions display different phenomena depending upon the quantities like mass, energy and angular momentum etc. Classically these collisions can be described in terms of their trajectories using the impact parameter b. Impact parameter is the perpendicular distance between the centre of force and the incident projectile direction. Each trajectory is uniquely determined by its impact parameter. Hence one can classify different reaction mechanisms using typical impact parameters. Fig. 1.1 illustrates different collision processes as a function of impact parameter. Collisions with very large impact parameters are generally known as distant collisions. They corresponds to the sub-barrier energies and are responsible for elastic scattering or at the most Coulomb excitations. With a smaller impact parameter $b \sim b_{gr}$, generally known as grazing impact parameter, the nuclei start experiencing the nuclear interaction. The reactions associated with such impact parameters are known as direct reactions, which involves only few degrees of freedom. These are also called quasi-elastic collisions and include transfer reactions and inelastic excitations. At impact parameters $b < b_{gr}$, which correspond to the projectile energies above the Coulomb barrier, the colliding nuclei keep their identity up to a net exchange of few nucleons, but a major fraction of the kinetic energy and the angular momentum are transferred from the relative motion to the intrinsic excitation of the collision partners. These collisions are generally called deep inelastic collisions (DIC). In this process the system remains together for a partial revolution only and retains a dinuclear shape with a little mass exchange between the partners. Although the kinetic energy becomes completely relaxed. Finally, the central trajectories with even smaller impact parameter ends up in the target i.e. the projectile and the target fuse completely (fusion reaction) and form a compound nucleus (CN). A complete transfer of mass, energy and angular momentum occurs and the composite system completes several rotations during which it equilibrates in all degrees of freedom.

The CN thus produced is *hot* and *rotating* i.e. it is highly excited and have large angular momentum. It can not stay in the excited state for a longer period of time and de-excites via various decay modes. The excitation energy of the CN is sum of the energy available in centre of mass frame (internal energy) and the reaction Q-value. The angular momentum distribution is generated by the range of impact parameters contributing to fusion. Other than excitation energy and angular momentum, the decay mode of CN is decided by the statistical factors and is completely independent of the entrance channel. The main decay modes are particle emission or fission. At higher energies and angular momenta, fission dominates the particle evaporation. At

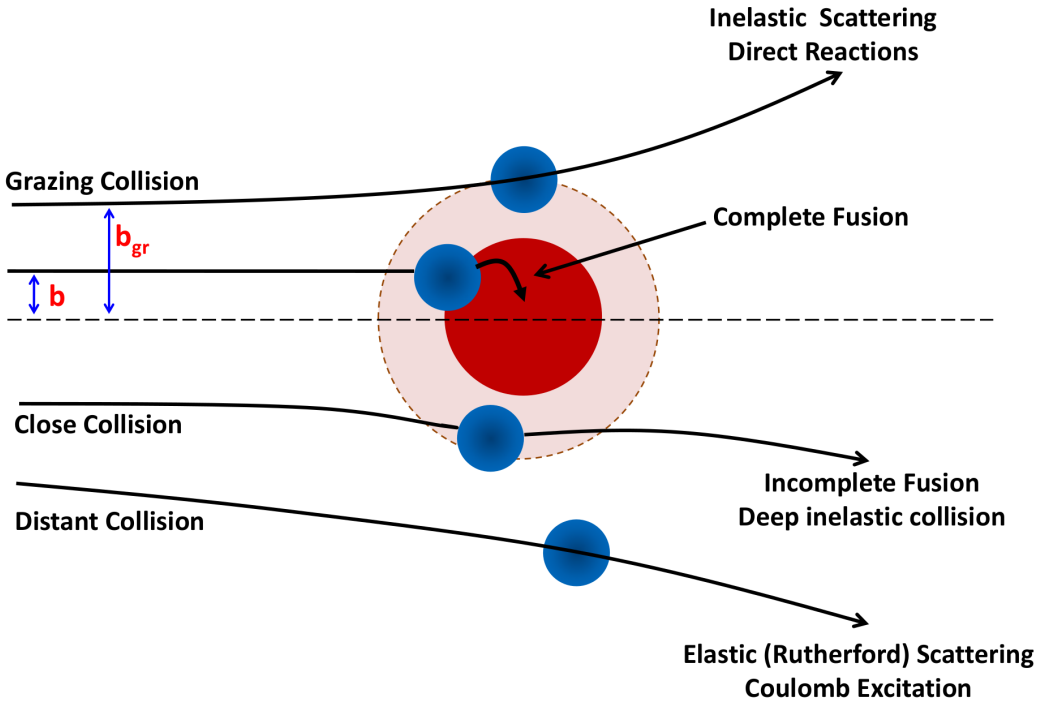

Figure 1.1: Schematic illustration of different processes in ion collision as a function of impact parameter.

higher angular momentum the centrifugal force increases and reduces the depth of the attractive potential pocket. Beyond a certain value of angular momentum (critical angular momentum), this attractive pocket vanishes and the system re-separates, soon after the capture. A further increase in the angular momentum gives rise to non-compound nucleus processes and inelastic processes.

1.2 Heavy ion fusion-fission reactions

Fusion is the process in which two or more nuclei join to form a new, heavier nucleus. The importance of the fusion lies in the sole existence of the universe, as fusion of hydrogen nuclei into helium is the key process for the energy generation in stars like Sun. Fusion is marked by the formation of a composite system called compound nucleus, which is not stable on macroscopic time scale but stays together for a time long enough in nuclear time scale.

1.2.1 Formation of the compound nucleus (CN) and its decay

When projectile and target nuclei approach each other during a nuclear reaction, after surpassing the Coulomb repulsion, there occurs a significant density overlap and the nucleons interact strongly which each other. The composite system attains energy equilibration. Classically when the system overcomes the repulsive Coulomb potential, it is captured in the attractive energy pocket. This leads to the fusion of the reaction partners and forms a compound nucleus (CN). The energy carried in by the entrance channel is shared among all the nucleons from both the colliding nuclei. This equilibrated system i.e. CN exists for a time longer compared to the time the projectile would take to pass by the target in the absence of interactions. CN life time ranges from 10^{-19} s to 10^{-16} s whereas the *flying-by-time* of the projectile is of the order of 10^{-21} s.

The excited CN carries an angular momentum, equal to the sum of the angular momentum of the relative motion in the entrance channel and the spins of the initial collision partners. The CN releases its excitation energy and the angular momentum via decay into smaller fragments. For compound nuclei at energies corresponding to the incident laboratory energies $E < 10\ MeV$ per nucleon of the projectile, two main decay channels are

(i) Evaporation: It is the emission of light particles like neutrons, protons or α-particles from the excited CN. A bound residual nucleus with a little lesser mass than the CN is remaining and is called *evaporation residue (ER)*. The process of particle evaporation is normally accompanied by γ-emission. The ER contains all the nucleons from the colliding nuclei except the few evaporated ones. Since protons and alpha particles have to tunnel through the Coulomb barrier, charged particle emission is inhibited compared to neutron evaporation for CN closer to stability. As the CN evaporates neutrons and moves further to the neutron deficient side, the separation energy for neutrons increases and the proton separation energy decreases. This makes the proton and alpha emissions to compete with neutron evaporation and generally the former takes over. Due to the very high density of states in the highly excited compound nucleus, the evaporated particles have a statistical energy distribution. These evaporated particles lower the excitation energy of the CN by around 5-8 MeV, and the angular momentum by 1-2 $\hbar$. Particle emission continues until the CN excitation energy is less than the particle separation energy above the yrast line.

(ii) Fission: In this process the CN splits into two halves of nearly equal size. Fission is accompanied by particle evaporation out of the fissioning nucleus. These are called pre-scission particles. Similarly the fission fragments can decay further by evaporation.

The emitted particles are termed as post-scission particles.

Evaporation is the dominant process for lighter systems and the ER production rate is a measure of the fusion cross section (fusion-evaporation). There is a competition between evaporation and fission for medium heavy-systems and for heavy systems the fission is the dominant mode of CN decay. In this case the fusion cross-section is essentially determined by the fission cross-section (fusion-fission). In general the sum of ER cross-section and fission cross-section gives the fusion cross section. For projectile energies $E > 10\ MeV$ per nucleon the processes like pre-equilibrium particle emission and projectile break-up occur which lead to an incomplete transfer of linear momentum. At still higher energies multifragmentation can take place i.e. the compound nucleus can break up into several pieces.

Mass and the angular momentum of the CN are the main factors which affect its stability. In general if the CN mass < 120, it decays into very asymmetric masses i.e. light particle emission. For CN mass in between 120 and 300, decay into symmetric masses (i.e. fusion-fission) is favoured. For CN mass > 300, it is unstable even in its ground state. A nucleus with non-zero angular momentum experiences centrifugal forces and is less stable than a nucleus with no angular momentum. Above a certain angular momentum, the nucleus will not even fuse to form a CN. The composite system immediately re-separates in to fission-like fragments.

1.2.2 Nucleus-nucleus interaction: fusion above Coulomb barrier

Classically a nuclear fusion is supposed to take place, if the energy of the relative motion of projectile and target is greater than their interaction barrier. This interaction consists of a long range repulsive Coulomb part and a short range attractive nuclear part. Combination of both the parts produce a hump called Coulomb barrier, and a attractive pocket after surpassing the Coulomb barrier (see Fig. 1.2). If the system has entered this attractive pocket, it is captured and will fuse. Angular momentum is the third component, which is of centrifugal nature. It increases the barrier height and makes the attractive pocket shallow, and the system tries to escape from it making the fusion less probable. The barrier is termed as one-dimensional barrier, as the nucleus-nucleus separation is the only degree of freedom. In the classical assumption, the projectile can either get scattered elastically of the target or can undergo a fusion with it to form a CN.

$$V_{Total} = V_{Coulomb} + V_{Nuclear} + V_{Centrifugal} \tag{1.1}$$

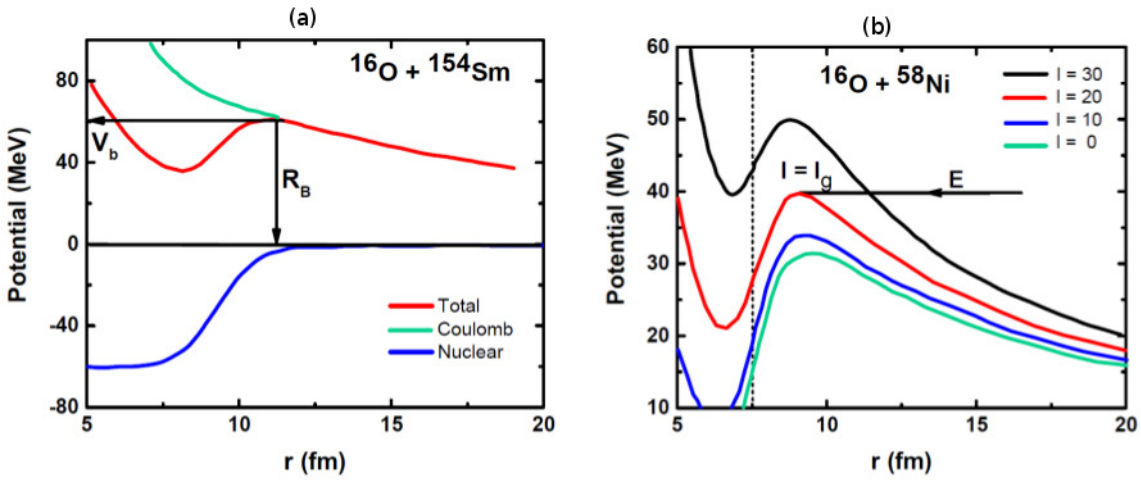

Figure 1.2: Schematic representation of (a) nucleus-nucleus interaction potential and (b) effect of the increasing angular momentum.

The effective potential which a projectile with energy E and impact parameter b experiences while moving in the field of the Coulomb and nuclear scattering potential is given by,

$$V_b(r) = V(r) + E\frac{b^2}{r^2} \tag{1.2}$$

The impact parameter associated with the trajectory of the particle having energy E, equal to the barrier height of the effective potential, is called *grazing impact parameter* b_{gr} and the corresponding radial distance is known as *barrier radius* R_B.

$$E = V_B + E\frac{b_{gr}^2}{R_B^2} \tag{1.3}$$

which implies,

$$b_{gr} = R_B\sqrt{1 - \frac{V_B}{E}} \tag{1.4}$$

In this classical picture, only projectiles with impact parameter $b < b_{gr}$ will fuse with the target and those with $b > b_{gr}$ will be reflected by the potential. The total fusion cross section, σ_F, is given by,

$$\sigma_F = \pi b_{gr}^2 \tag{1.5}$$

Substituting for b_{gr},

$$\sigma_F(E) = \pi R_B^2 \Big(1 - \frac{V_B}{E}\Big) \tag{1.6}$$

In the quantum counterpart of this classical picture, called sharp cut off model, all partial waves with angular momentum l less than the *grazing angular momentum* $l_{gr}(= kb_{gr})$ are absorbed. Here k is the wave number. Partial waves with $l > l_{gr}$ remain unaffected by the nuclear potential. Therefore the fusion cross section in the sharp cut off model is given by,

$$\sigma_F(E) = \frac{\pi}{k^2} \sum_{l=0}^{\infty} (2l+1) T_l \tag{1.7}$$

with the transmission coefficient T_l

$$T_l = \begin{cases} 0 & \text{if } l > l_{gr} \\ 1 & \text{if } l < l_{gr} \end{cases}$$

In the classical limit with $l >> 1$, Eqn. 1.7 becomes

$$\sigma_F(E) = \frac{\pi}{k^2} l_{gr}^2 = \pi b_{gr}^2 \tag{1.8}$$

As already discussed the CN is formed only for an impact parameter $b < b_{gr}$. However, the CN becomes unstable against prompt fission for angular momenta more than a critical angular momentum, l_{crit}. The fusion can happen if the impact parameter b is smaller than a critical value b_{crit}, ($= l_{crit}$ / k). The cut-off is decided by b_{gr} or b_{crit}, whichever is smaller. Hence,

$$\sigma_F = \begin{cases} \pi b_{gr}^2 & \text{if } b_{gr} < b_{crit} \\ \pi b_{crit}^2 & \text{if } b_{gr} > b_{crit} \end{cases}$$

Apart from the impact parameter and angular momentum the fusion depends upon the density overlap of the interacting nuclei. Therefore, even if the impact parameter is less than the cut-off limit (b_{gr} or b_{crit}, whichever is smaller), the collision doesn't ensure the CN formation if sufficient density overlap is not achieved. Thus the reaction heads towards the fusion if the relative distance between the interacting nuclei is less than a *critical distance*. This critical distance may be appreciably smaller than the barrier radius. Trajectories which cross the barrier, but do not penetrate closer than the critical distance lead to direct or other deep-inelastic processes. The concept of critical distance is introduced for considering the non-compound nuclear processes taking place along with the fusion.

1.2.3 Sub-barrier fusion: barrier penetration

In classical assumptions, fusion is possible only when the system overcomes the Coulomb barrier i.e. the transmission coefficient will have a value $T_l = 1$ (complete fusion) for above barrier energies and $T_l = 0$ (no transmission, and therefore no fusion) for sub-barrier energies. However, at energies below the Coulomb barrier, quantum mechanical effects [4, 5] plays a role and influence the fusion cross section. Depending on the relative kinetic energy, the two nuclei will undergo fusion either by passing over the barrier or by a quantum mechanical tunneling through the barrier.

The fusion cross section at an energy E is given by the summation over the partial waves,

$$\sigma_F = \frac{\pi\hbar^2}{2\mu E}\sum_{l=0}^{\infty}(2l+1)T_l \tag{1.9}$$

μ is the reduced mass. The transmission coefficient T_l is given by the Hill-Wheeler formula [6]

$$T_l = \frac{1}{1+exp\Big[\frac{2\pi}{\hbar\omega_l}(V_B(l)-E_{cm})\Big]} \tag{1.10}$$

where $V_B(l)$ is the barrier height for l^{th} partial wave and $\hbar\omega_l$ is the corresponding barrier curvature. Generally it is assumed that the barrier position and curvature are independent of the angular momentum. Hence,

$$\hbar\omega_l = \hbar\omega_0$$
$$V_l = V_0 + \hbar^2 l(l+1)/2\mu R^2 \tag{1.11}$$

The summation in Eq. 1.9 can be replaced by integration to obtain the total fusion cross section, given by Wong's formula [7]

$$\sigma_F = \frac{R_B^2 \hbar\omega_0}{2E_{cm}} ln\Big\{1 + exp\Big[\frac{2\pi}{\hbar\omega_0}(E_{cm} - V_B)\Big]\Big\} \tag{1.12}$$

For relatively small values of E_{cm} ($E_{cm} << V_B$), this equation can be represented as

$$\sigma_F = \frac{R_B^2 \hbar\omega_0}{2E_{cm}} exp\Big[\frac{2\pi}{\hbar\omega_0}(E_{cm} - V_B)\Big] \tag{1.13}$$

This is known as one dimensional barrier penetration model (1D-BPM). The above expression shows that fusion cross section decreases exponentially with decrease in energy below the Coulomb barrier. Though further enhancements with respect to 1D-BPM were observed in below barrier fusion cross sections due to coupling of various degrees of freedom.

1.2.4 Statistical model

In the process of CN formation, the composite system, after the capture, follows a long dynamical path during which it equilibrates in all degrees of freedom. For lighter projectiles in asymmetric reactions, overcoming the Coulomb barrier is sufficient for the CN formation, as the angular momentum and the excitation energy brought in are not so high. However, for heavier projectiles and symmetric reactions it doesn't assure CN formation. The CN formed in a heavy ion reaction is excited and has high angular momentum. It tries to go to the ground state by releasing its energy via different decay modes. At higher excitation energies, particle evaporation and fission are the prominent decay channels. During evaporation, particles like neutrons, protons, α-particles and some times cluster of nucleons are emitted. The evaporation is possible from the CN itself or from the decay products (evaporation residue or fission fragments). During fission, the CN splits up into two fragments of nearly equal size. This process is also accompanied by evaporation of nucleons. The evaporation and fission continue till the

excitation energy becomes less than the particle separation energy and fission barrier. After this, gamma emission takes over the decay process.

The decay of the CN is successfully described by the statistical model. The statistical model follows the assumption that all capture leads to equilibrium. Once the CN is formed all decay channels that are *open* are *on the average*, equally likely to be populated. *Open* channel means a particular final state, specified by all quantum numbers including the magnetic quantum number, which can be reached from the initial state without the hindrance of barrier penetration. The statistical model says that the probability of decay to a particular channel (or group of channels n) is $1/N$ (or n/N), where N is the total number of open channels. In any given measurement at a specific beam energy E and $E + \Delta E$, individual channels will not exhibit the same cross section or probability of population, rather the cross sections will be distributed about a mean value. The number of nucleons are finite in a nucleus but the number of possible configurations are very large and increases exponentially with excitation energy. Even with the lowest excitation energies, there are a number of levels to which a CN can decay and there are a number of ways in which this decay can take place. This complexity necessitates the use of statistical models in describing the decay of a CN.

1.2.5 Non-compound nuclear proscesses

The composite system trapped inside the potential energy pocket, not necessary to always form a CN. Experimental observations suggest that depending upon the parameters like energy, angular momentum, mass asymmetry of the entrance channel etc., the dinuclear system can either equilibrates in all degrees of freedom to form a CN or re-separates before the complete equilibration. These unequilibrated processes are generally called non-compound nucleus processes. These processes include quasifission, fast fission etc. Quasifission is the non-equilibrium process originating due to the compact saddle point configuration of the system compared to the contact configuration. Fast fission is the non-equilibrium process which is dominant at higher energies. This process occurs when the fission barrier vanishes as a result of large angular momentum. The potential trap in the nucleus-nucleus interaction potential, also might disappear at such high angular momentum and the system will not have sufficient time to equilibrate before the re-separation. Fig. 1.3 illustrates the processes like compound nucleus formation, evaporation, fission, quasifission and fast fission.

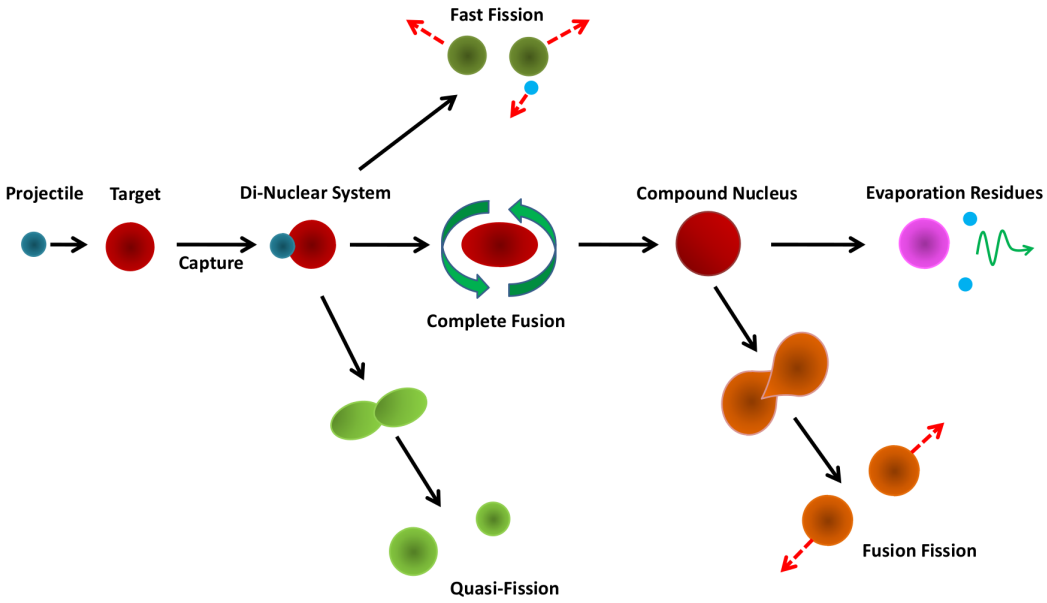

Figure 1.3: Schematic representation of the processes like compound nucleus formation, evaporation, fission, quasifission and fast fission.

1.3 Motivation of the present work

The one-dimensional barrier penetration model explains the nuclear fusion quite reasonably. However, enhanced fusion cross-sections were observed below the Coulomb barrier. The enhancement of experimental reaction cross-section was found to be due to the coupling of the internal degrees of freedom, such as static deformation of the collision partners, collective surface vibrations and transfer channels etc., with the relative motion [8, 9]. The tunnelling through the barrier and subsequent capture are enhanced by the coupling of these internal degrees of freedom around the barrier.

It was observed that at higher excitation energies, the pre-scission neutron, charge particle and giant dipole resonance (GDR) γ-decay multiplicities exceed the statistical model predictions [10]. Inclusion of dissipation or viscosity effects into the Bohr-Wheeler formalism [11] is required to explain these higher multiplicities. These effects reduce the fission and increase the particle and gamma emission in the pre-saddle region and thereby, the ER cross-section. However, often the ER cross sections can not be reproduced with the same strength of dissipation [12, 13]. Usually a smaller dissipation strength is required to reproduce the ER data in comparison with that required for pre-scission multiplicity data. For a number of systems, the fission is enhanced by reducing the height of the liquid drop model (LDM) fission barrier to fit the ER

cross-sections [14, 15].

As per the CN hypothesis, the dinuclear system follows a long dynamical path during which it equilibrates in all degrees of freedom or re-separates into fission-like fragments. The CN which de-excites via particle evaporation or gamma emission and survives fission, ends up as various evaporation residues (ER). Formation of these ERs depends on the capture probability, CN formation probability and its survival probability against fission. ER cross-section is given as

$$\sigma_{ER} = \sigma_{cap} \times P_{CN} \times P_{surv} \tag{1.14}$$

where σ_{cap} is capture cross-section, P_{CN} is CN formation probability and P_{surv} is its survival probability against fission. For light and very asymmetric systems, merely overcoming the capture barrier is sufficient for CN formation but this is not the case for heavier systems, as they may re-separate before CN formation giving rise to non compound nuclear processes.

While explaining the reaction excitation function, any deviation from the standard statistical model predictions is generally attributed to either the presence of proton or neutron shell closure in the compound nucleus or to the contribution from non compound nuclear fission (NCNF). Studying both these effects is important, as they are the factors affecting the formation and survival of the super heavy elements. While shell effects are known to give extra stability against fission, NCNF reduces the probability of complete fusion. Around $A = 200$ amu mass region and beyond, CN fission and NCNF co-exist and it is very difficult to experimentally disentangle these processes, as they have overlapping experimental signatures [16]. Generally NCNF processes are observed with comparatively symmetric reactions. However, recent studies show a probability of these effects with asymmetric systems also in the heavier mass region. A recent systematic analysis of existing ER cross-section data in the mass region of 170 - 220 amu [17], identified the approximate boundaries from where the average fusion probability $\langle \mathrm{P}_{CN} \rangle$ deviates from unity i.e. the NCNF processes starts appearing.

Effects of proton and neutron shell closures ($Z = 82$ and/or $N = 126$) on survival of ER against fission [18–22], fission fragment angular anisotropy [23, 24], mass distribution [25], quasifission [26] and other observables like alpha decay [27] have been studied. ERs, being the true signatures of CN formation, can be used to explore the onset of NCNF and also the dissipative and shell effects. There are still several unanswered questions requiring further studies to get a complete picture of the nuclear reaction dynamics leading to a better understanding of SHE formation. SHE, having sub pico

barn formation cross section, are practically not suitable for systematic investigation of reaction mechanism. However, one can study the process in the vicinity of heaviest naturally occurring stable nuclei. Therefore the knowledge acquired through understanding the NCNF or the effect of N or Z shell closure on fusion-fission dynamics is of great importance in the formation of long-lived heavy nuclei and hence superheavy elements.

1.4 Present study

Evaporation residue measurements in the mass region beyond $A = 200$ amu, can give useful information regarding the stabilizing effects of $N = 126$ shell closure as well as NCNF. We proposed to measure the total ER cross-section and the individual evaporation channels (viz. 3n, 4n, 5n etc.) for the reactions ^{16}O + ^{203}Tl and ^{16}O + ^{205}Tl producing the CN ^{219}Ac and ^{221}Ac respectively. The measurements are proposed at energies around and above the Coulomb barrier. The total ER cross-section can be measured by direct detection of ERs at the focal plane of a mass separator using a multi wire proportional counter or a large area silicon detector. The individual channel selection for ERs is proposed via decay alpha tagging at the focal plane of the mass separator.

Motivation behind the total ER cross section measurement is to explore the effect of NCNF on fusion-fission dynamics in this mass region. Experimental ER cross-section in comparison with statistical model calculations, would provide the information regarding the NCNF processes in these reactions. As the general assumptions does not expect NCNF in such asymmetric systems. However, recent studies speculate these effects even with asymmetric reactions in this mass region. It will be useful to explore it experimentally.

The purpose of individual channel ER cross section measurements is to establish the the stabilizing effect of $N = 126$ shell closure, if any, against fission. Both these reactions after complete fusion will form excited compound nuclei above $N = 126$ shell closure, which after few neutron evaporation, forms ERs with certain neutron numbers. This is interesting to see the enhancement in cross-section of a particular evaporation channel (viz. 2n or 3n etc.), which produces an ER with shell closure, as compared to others channels, in the same reaction, over a range of excitation energies. Also it would be interesting to compare the cross sections for a particular channel say 4n, over similar excitation energy range, in both the reactions. In ^{16}O + ^{203}Tl, 4n evaporation would produce ER with $N = 126$ and in ^{16}O + ^{205}Tl it will produce an ER with neutron number away from the shell ($N = 128$). A comparison for different neutron evaporation

cross sections in the above systems might bring out the stabilizing effect of $N = 126$ neutron shell, if any.

1.5 Plan of the thesis

In the present thesis we aim to study the heavy ion fusion-fission reactions in heavy mass region in the vicinity of A $\sim$ 215. We tried to explore the phenomena like shell closure or NCNF which makes the experimental ER cross-sections to deviate from the predictions of the statistical model. With this motivation the evaporation residue cross section measurements for ^{16}O + ^{203,205}Tl reactions in the laboratory energy 82 to 113 MeV are carried out.

Following the general introduction and literature survey in chapter 1, in chapter 2, we discuss the experimental setup, detectors and electronics used in the present study. Chapter 3 gives the information regarding target fabrication and characterizations. In chapter 4, we present the data analysis and results of ER measurements for the two reactions. Finally in Chapter 5 the works presented in this thesis are summarized and the scope of future works are highlighted.

Bibliography

[1] S. Hofmann and G. Münzenberg, Rev. Mod. Phys. **72**, 733 (2000).

[2] J. H. Hamilton, S. Hofmann, and Y. T. Oganessian, Annu. Rev. Nucl. Part. Sci. **63**, 383 (2013).

[3] Y. T. Oganessian and V. K. Utyonkov, Reports on Progress in Physics **78**, 036301 (2015).

[4] G. Gamow, Z. Phys **51**, 204 (1928).

[5] G. Gamow, Z. Phys **52**, 510 (1929).

[6] D. L. Hill and J. A. Wheeler, Phys. Rev **89**, 1102 (1953).

[7] C. Y. Wong, Phys. Rev. Lett **31**, 766 (1973).

[8] M. Dasgupta, D. Hinde, N. Rowley, and A. Stefanini, Annu. Rev. of Nucl. and Parti. Sci. **48**, 401 (1998).

[9] M. Beckerman, Reports on Progress in Physics **51**, 1047 (1988).

[10] M. Thoennessen and G. F. Bertsch, Phys. Rev. Lett. **71**, 4303 (1993).

[11] N. Bohr and J. A. Wheeler, Phys. Rev. **56**, 426 (1939).

[12] I. Dioszegi, N. Shaw, I. Mazumdar, A. Hatzikoutelis, and P. Paul, Phys. Rev. C **61**, 024613 (2000).

[13] P. Nadtochy, E. Ryabov, A. Gegechkori, Y. A. Anischenko, and G. Adeev, Phys. Rev. C **85**, 064619 (2012).

[14] R. N. Sagaidak, G. N. Kniajeva, I. M. Itkis, M. G. Itkis, N. A. Kondratiev, E. M. Kozulin, I. V. Pokrovsky, A. I. Svirikhin, V. M. Voskressensky, A. V. Yeremin, *et al.*, Phys. Rev. C **68**, 014603 (2003).

[15] R. N. Sagaidak and A. N. Andreyev, Phys. Rev. C **79**, 054613 (2009).

[16] D. J. Hinde, R. du Rietz, and M. Dasgupta, EPJ Web of Conferences **17**, 04001 (2011).

[17] T. Banerjee, S. Nath, and S. Pal, Phys. Rev. C **91**, 034619 (2015).

[18] Y. Le Beyec *et al.*, Nucl. Phys. A **192**, 405 (1972).

[19] D. Vermeulen, H. G. Clerc, and C. C. Sahm, Z. Phys. A **318**, 157 (1984).

[20] D. Ackermann *et al.*, Eur. Phys. J. A **20**, 151 (2004).

[21] A. N. Andreyev, D. Ackermann, S. Antalic, I. G. Darby, S. Franchoo, F. P. Heßberger, S. Hofmann, M. Huyse, P. Kuusiniemi, B. Lommel, B. Kindler, R. Mann, G. Münzenberg, R. D. Page, S. Saro, B. Sulignano, B. Streicher, K. V. d. Vel, P. V. Duppen, and D. R. Wiseman, Phys. Rev. C **72**, 014612 (2005).

[22] J. Gehlot, S. Nath, T. Banerjee, I. Mukul, R. Dubey, A. Shamlath, P. V. Laveen, M. Shareef, M. M. Shaikh, A. Jhingan, N. Madhavan, T. Rajbongshi, P. Jisha, and S. Pal, Phys. Rev. C **99**, 061601 (2019).

[23] A. Shrivastava, S. Kailas, A. Chatterjee, A. M. Samant, A. Navin, P. Singh, and B. S. Tomar, Phys. Rev. Lett. **82**, 699 (1999).

[24] K. Mahata, S. Kailas, A. Shrivastava, A. Chatterjee, P. Singh, S. Santra, and B. S. Tomar, Phys. Rev. C **65**, 034613 (2002).

[25] A. Chaudhuri, T. K. Ghosh, K. Banerjee, S. Bhattacharya, J. Sadhukhan, S. Kundu, C. Bhattacharya, J. K. Meena, G. Mukherjee, A. K. Saha, M. A. Asgar, A. Dey, S. Manna, R. Pandey, T. K. Rana, P. Roy, T. Roy, V. Srivastava, P. Bhattacharya, D. C. Biswas, B. N. Joshi, K. Mahata, A. Shrivastava, R. P. Vind, S. Pal, B. R. Behera, and V. Singh, Phys. Rev. C **92**, 041601(R) (2015).

[26] M. Morjean, D. J. Hinde, C. Simenel, D. Y. Jeung, M. Airiau, K. J. Cook, M. Dasgupta, A. Drouart, D. Jacquet, S. Kalkal, C. S. Palshetkar, E. Prasad, D. Rafferty, E. C. Simpson, L. Tassan-Got, K. Vo-Phuoc, and E. Williams, Phys. Rev. Lett. **119**, 222502 (2017).

[27] A. N. Andreyev, M. Huyse, P. Van Duppen, C. Qi, R. J. Liotta, S. Antalic, D. Ackermann, S. Franchoo, F. P. Heßberger, S. Hofmann, I. Kojouharov, B. Kindler, P. Kuusiniemi, S. R. Lesher, B. Lommel, R. Mann, K. Nishio, R. D. Page, B. Streicher, S. Šáro, B. Sulignano, D. Wiseman, and R. A. Wyss, Phys. Rev. Lett. **110**, 242502 (2013).

Chapter 2

Experimental setup

In this chapter, the details of the experimental facilities, detectors, electronic setup, measurement and procedures for the present study are given. In the present work we have measured the ER cross sections for ^{16}O + ^{203}Tl and ^{16}O + ^{205}Tl reactions. The measurements were carried out using heavy ion beam provided by 15 UD tandem accelerator at Inter University Accelerator Centre (IUAC), New Delhi using the gas filled separator HYbrid Recoil mass Analyzer (HYRA). The accelerator facility, mass separators, detectors and electronics, used in the present study are discussed further.

2.1 15 UD tandem accelerator

Measurements were carried out at 15 UD Pelletron accelerator facility of IUAC, New Delhi (India) [1, 2]. The IUAC Pelletron is an electrostatic tandem accelerator. A tandem accelerator utilizes the terminal high voltage twice in sequence in order to obtain output energies of two or more times of that available in a single acceleration.

The Pelletron accelerator column is installed in vertical configuration in a 26.5 meter long and 5.5 meter diameter steel tank. A high voltage terminal is located at the tank centre. The terminal can be charged to a very high voltage ranging from 4 MV to 15 MV. A potential gradient is maintained through the accelerating tube by placing 15 units of 1 MV on either side of the terminal. The areas before and after the terminal is called low energy and high energy sections respectively. Two shorted units with no potential gradient commonly known as dead sections, are also provided, one on either side of the terminal for housing the vacuum pumps and other beam handling components. Fig. 2.1 shows an schematic diagram of the IUAC Pelletron accelerator.

IUAC Pelletron uses a Multi Cathode Source of Negative Ions by Cesium Sputtering (MCSNICS). The singly charged negative ions are pre accelerated upto $\sim$ 200 keV

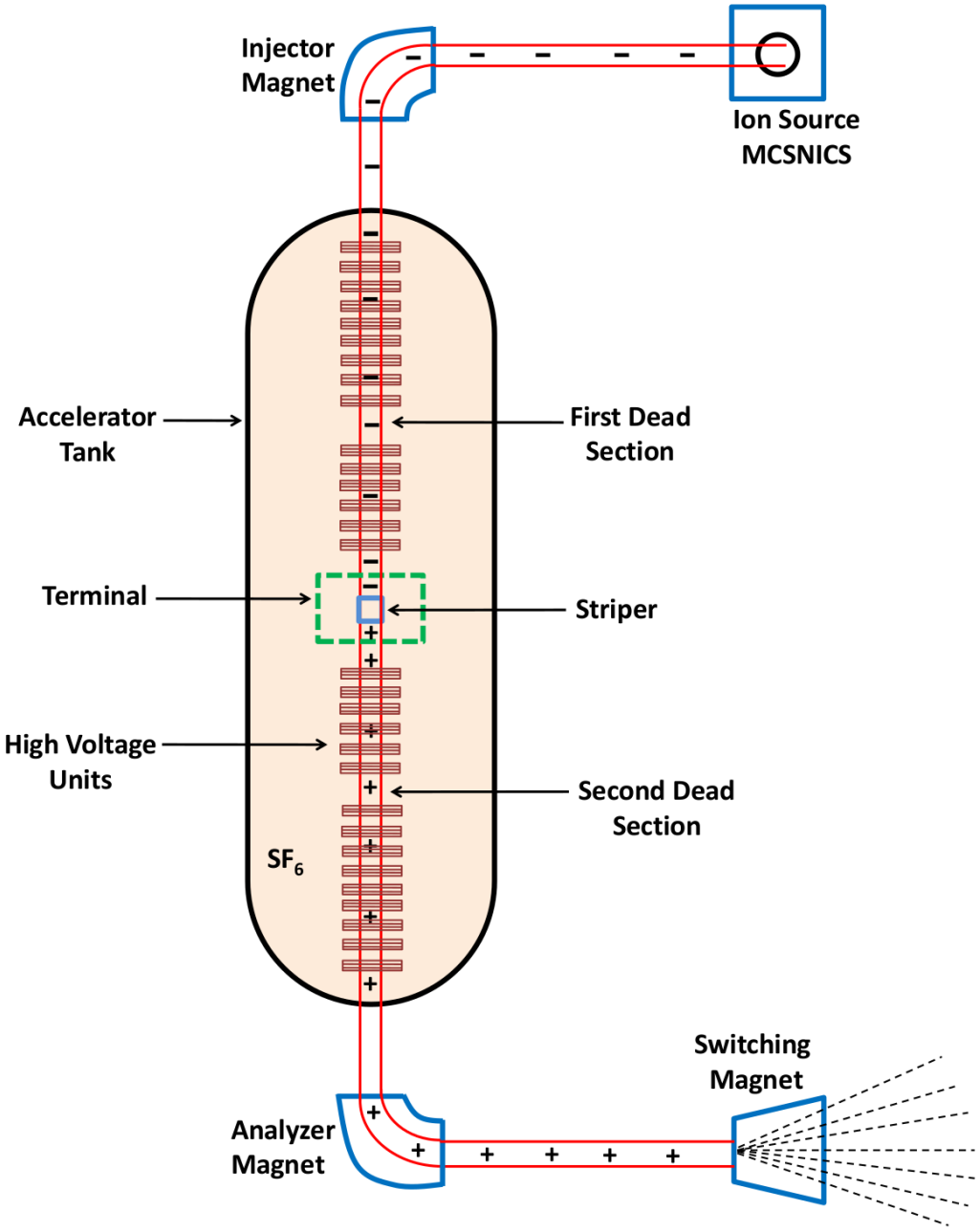

Figure 2.1: Schematic diagram of the 15 UD tandem accelerator at IUAC, New Delhi.

and injected to the vertical accelerator tube, after mass selection using a 90° bending injector magnet. These ions are accelerated towards the high voltage terminal and gain an energy (in MeV)

$$E = (E_{inj} + V) \tag{2.1}$$

where E_{inj} is the energy of the ion before injection to the accelerating tank (gained in pre-acceleration) and V is the terminal potential in MV. At terminal there is a stripper, which is usually a thin film of carbon or a dilute gas medium, which strips the electrons from the incoming negative ions and converts them into positive ions. The charge state distribution of these ions depends upon mass and velocity of the ions being accelerated. These positive ions are repelled by the positive terminal and get accelerated again. Out of this charge distribution, ions with a particular charge state are selected using a 90° bending dipole magnet called Analyzer magnet, based on their energy, mass and charge state. The total energy (in MeV) of the ion after the terminal is

$$E = [E_{inj} + V + qV] \tag{2.2}$$

or

$$E = [E_{inj} + V(1 + q)] \tag{2.3}$$

where q is the charge state of the ion after the terminal. Sometimes a second stripper is also used to increase the ion charge state and hence its energy. The second stripper is always a foil stripper located in the high energy dead section, situated after six units from the terminal. Then the total energy (in MeV) gained becomes

$$E = [E_{inj} + V(1 + q_1\frac{6}{15} + q_2\frac{9}{15})] \tag{2.4}$$

or

$$E = [E_{inj} + V(1 + 0.4 \times q_1 + 0.6 \times q_2)] \tag{2.5}$$

where q_1 and q_2 are the ion charge states after first and second strippers respectively. This accelerated beam of ions with well defined energy, mass and charge state is then put into the experimental beam line using a switcher magnet with multiple ports for different experimental facilities.

Depending upon the experimental requirements, the accelerator can provide continuous or a pulsed beam. The pulsing system comprises of chopper, buncher and a travelling wave deflector (TWD). These components are placed between injector magnet and the tank top, i.e. in the pre-acceleration stage. The chopper chops off the beam at regular intervals by making use of a pair of plates in which a radio frequency field is applied. The buncher bunches these chopped beam pulses by compressing them in time and finally TWD decides the repetition rate of the beam pulses by selectively removing these pulses at regular interval. This off course reduces the effective current intensity of the beam.

2.2 Recoil separators

Recoil separators [3, 4] are the instruments, comprising of electromagnetic components like quadrupoles, magnetic and (or) electrostatic dipoles, used for beam rejection and mass analysis of the reaction products in a nuclear reaction.

2.2.1 Need of recoil separators

In a nuclear reaction experiment, an energetic primary beam is bombarded on a thin target foil and as a result we encounter various species of particles. These species are intense unreacted primary beam, fusion products of beam with the target, fusion products from unwanted reactions like those of the beams with target backing or with impurities in the target material, knocked off target like particles for an head on collision as well as products from incomplete fusion or transfer reactions. We are mostly interested in complete fusion-evaporation reactions. The basic task of the recoil separators is to spatially separate these different species emerging from the target area.

The yield of the particles of our interest (complete fusion-evaporation residue recoils), is peaked near 0° i.e. in beam direction, in a narrow cone angle. They are mixed in with other particle species, mostly scattered primary beam particles. In order to achieve the maximum separation of beam and evaporation residues, the beam particles are blocked at an early stage of the separator. Also these particles of interest are generally much less ($\sim$ 10 to 12 orders of magnitude less) than the incident beam. Hence, it is a very difficult task to separate them from this beam like and target like background and to detect them.

If one needs to increase the production rate of reaction products then either the target thickness or the beam intensity has to be increased. If the target thickness is increased too much, the reaction products may not come out of the target due to

excessive energy loss in the target. Usually a target thickness of the order of few hundred μg/cm^2 is optimum for nuclear reaction experiments. However, if the beam intensity is increased enormously, almost all the beam particles will come out of the target (as the stopping power of light, energetic beam particles is much less than the heavy, slower reaction products). Any detector put in its path will be damaged. Neither the gas detectors nor the semiconductor detectors can handle these forward focused reaction products in the absence of a recoil separators. Reduction of beam current will not serve the purpose, as it will reduce the production rate. Therefore the recoil separators are deployed for
(i) beam rejection,
(ii) mass analysis of reaction products,
(iii) transportation of the reaction products to a background free area (i.e. focal plane of the separator) and
(iv) final focusing of these products at the focal plane detector, so that it can detect all the particles of interest.

2.2.2 Characteristics of recoil separators

An ideal recoil separator should be capable of best possible rejection of the unwanted products like primary beam. It should be capable of space focusing (both vertical and horizontal). It should have a large solid angle of acceptance, large mass dispersion, good mass resolution, no energy dispersion at final point, large energy and mass acceptances and large transmission efficiency.

In general there are two types of recoil mass separators, one is vacuum mode recoil mass separators (involving magnetic and/or electric fields) and another is gas filled magnetic separator. Electrostatic elements can not be operated in gas atmospheres, hence gas filled separators use magnets only. Consequently the separation in the gas filled devices relies on differences in the magnetic rigidity of the particles.

All the above said characteristics cannot be simultaneously fulfilled by any one type of separator. Hence the choice of the type of recoil mass separator depends entirely on the reaction mechanism/kinematics and the requirements of the experiment.

2.2.3 Vacuum mode separators

Vacuum mode separators [5] use electric and/or magnetic fields for the particle separation. Separation of the desired and undesired species can be based on different properties in which they differ, e.g. mass, mass to charge ratio, velocity, momentum, kinetic energy, or angular distribution of these particles.

For separation of particles on the basis of their momentum one uses magnetic deflector. To separate the particles on the basis of their energy, an electrostatic deflector is used and an $\vec{E} \times \vec{B}$ filter is used to separate the particles according to their velocity. For mass identification one needs at least two of the three parameters viz. velocity, momentum and energy. In addition, magnetic quadrupole lenses are used for focusing the ions, and magnetic multipoles (usually sextupoles and octupoles) are used to correct higher order aberrations. The separation is based on the basic principles of Coulomb and Lorentz forces, which a charged particle experiences while traversing the electric and magnetic fields respectively.

After the bombardment of primary beam on a target in a nuclear reaction, most of the unreacted beam particles, the reaction products and some of the target nuclei come out with almost original momentum at different angles around the primary beam direction. The lighter and more energetic primary beam and the heavier and less energetic reaction products have the same momentum. Hence they can be separated only on the basis of their energy or velocity which requires an electrostatic deflector or a $(\vec{E} \times \vec{B})$ filter respectively.

The electrostatic deflector basically consists of two coaxial, cylindrical plates, one of which is the anode and the other is the cathode. If the energy of the positive ions entering the energy filter is too large, those ions will not be deflected much by the radial electric field and will collide with anode plate. If the energy is very small, the ions will get deflected more and collide with cathode plate. The ions can move along the central trajectory of radius of curvature ρ only when the energy is such that it satisfies the equation

$$q.E = \frac{m.v^2}{\rho} \tag{2.6}$$

or

$$E.\rho = \frac{m.v^2}{q} = \frac{2T}{q} \tag{2.7}$$

where E is the electric field between deflector plates, m is mass, v is velocity, q is charge state and T is the kinetic energy of the particle. The quantity $E.\rho$ is called electric rigidity, which is a measure of the difficulty in the deflection of the ion from its path using an electric field.

Similarly the magnetic dipole consists of two electromagnetic poles with opposite polarity. The field direction is orthogonal to the direction of motion of the ions. The ions entering the perpendicular magnetic field of uniform flux density B will follow a circular path, with radius ρ as the force is always normal to the magnetic field.

$$q(\vec{v} \times \vec{B}) = qvB = \frac{m.v^2}{\rho} \tag{2.8}$$

or

$$B.\rho = \frac{m.v}{q} = \frac{P}{q} \tag{2.9}$$

$B.\rho$ is the magnetic rigidity, which is a measure of the difficulty in the deflection of the ion from its path using a magnetic field. Where ρ is the radius of curvature of the particle's trajectory, m, v and q are the mass, velocity and charge state respectively, of the ion.

Using the combination of electric dipole and magnetic dipole, the particles can be separated as per their m/q ratio. The ions having same m/q ratio (but different m values) will be focused at the same point at the detector plane. This is called m/q ambiguity and it can be resolved by time of flight (TOF) method. For example, if two ions have same momentum then the lighter one will have more velocity and less time of flight. Similarly the heavier one will have less velocity and more time of flight. Thus by measuring the time of flight the ions are identified. However, the ions with the same mass number but different atomic numbers (isobaric nuclei) will have identical trajectories, if they have same energy and same charge state. Such ions are therefore not separated by the spectrometer. Heavy Ion Reaction Analyzer (HIRA), at IUAC New Delhi is one good example of a vacuum mode recoil separator [6].

2.2.3.1 Advantages and disadvantages of vacuum mode separators

Vacuum mode separators have good mass resolution i.e. the particles are well separated as per their m/q ratio, following well defined trajectories. They are capable of good beam rejection for asymmetric reactions and for normal kinematics. However, they have poor efficiency due to charge state dispersion, as all the charge states can not be transmitted through the limited size aperture of beam transportation tube. Also it is affected by the kinematics and the particle evaporation from compound nucleus leading to large cone angle and energy spread especially for heavy residues produced

using lighter beam.

The transmission efficiency can be improved by using inverse kinematics because of the following reasons:
(i) In inverse kinematics, i.e. a heavy projectile on a lighter target, the scattering is in a smaller cone angle resulting in most of the particles being within the angular acceptance of the spectrometer. In addition, the path of the compound nucleus, due to its higher momentum, will not be affected by alpha, proton or neutron emission.
(ii) As the compound nucleus moves with higher energy as compared to that in normal kinematics, the energy loss in target is smaller and hence the fractional energy deviation from mean energy is narrow so that most of the particles are within the energy acceptance of the spectrometer.
(iii) Also in inverse kinematics, the mean charge state of evaporation residues (ERs) is higher due to higher ER energy which results in a smaller fractional change for adjacent charge states so that more than one charge state can be accepted within the m/q acceptance of the separator (e.g. a change of 1 in 10 units of charge state is 10% whereas the same change in 25 is only 4%). Thus we see that inverse kinematics provides larger transmission efficiency.

However, inverse kinematics has some drawbacks in heavy residue formation. The projectile energy required to overcome the Coulomb barrier is higher in inverse kinematics as compared to normal kinematics. The projectile energy E_P in the laboratory frame of reference, is used in two parts i.e.

$$E_P = E_{CN} + E_{int} = E_P \frac{M_P}{(M_P + M_T)} + E_P \frac{M_T}{(M_P + M_T)} \tag{2.10}$$

where E_{CN} is the energy of motion of centre of mass (CM) system in the laboratory frame (i.e. kinetic energy of compound nucleus), E_{int} is internal energy of the compound nucleus (also known as the energy available in centre of mass ie $E_{c.m.}$). M_P and M_T are projectile and target masses respectively. This internal energy causes reaction to take place overcoming the Coulomb barrier and along with the Q-value of the reaction causes particle and/or gamma evaporation. One can see from Eqn. 2.10 that for any projectile-target combination, the energy available as E_{int} is much less in inverse kinematics as compared to normal kinematics. Hence, if we use inverse kinematics, we need larger, high energy accelerators to overcome the large Coulomb barrier. Therefore usually normal kinematics is used in heavy nuclei formation which suffers from poor transmission. In order to achieve better transmission, with normal kinematics itself, gas filled separators (GFS) are used especially in heavy element search/production.

2.2.4 Gas Filled separators

As shown in the previous section, the ions travelling through a perpendicular magnetic field are dispersed according to their magnetic rigidity (B.ρ). Since in gas filled separators [7], as the name suggests, the magnetic field region is filled with a dilute gas. The ions undergo atomic collisions with the gas molecules in which electrons can be lost or captured, changing the charge state of the ions. If the number of charge changing collisions is sufficiently high, their charge state fluctuates around average or mean charge state q_m. The ions will closely follow the trajectory determined by the mean magnetic rigidity corresponding to the mean charge state of the ion. Fig. 2.2 shows the ion trajectories in (a) vacuum mode magnetic field region and (b) gas filled magnetic region.

The mean charge state q_m of the ions, depends on the atomic number Z and is roughly proportional to its velocity v as $\sim v\ Z^{\frac{1}{3}}$; i.e. the mean magnetic rigidity

$$B\rho \propto \frac{mv}{q_m} \propto \frac{m}{Z^{\frac{1}{3}}} \tag{2.11}$$

where m and v are the mass and velocity of the ion.

Ghiorso et al. [8], gave an approximate formula for the magnetic rigidity in gas

$$B\rho = 0.0227\frac{A}{Z^{\alpha}} \tag{2.12}$$

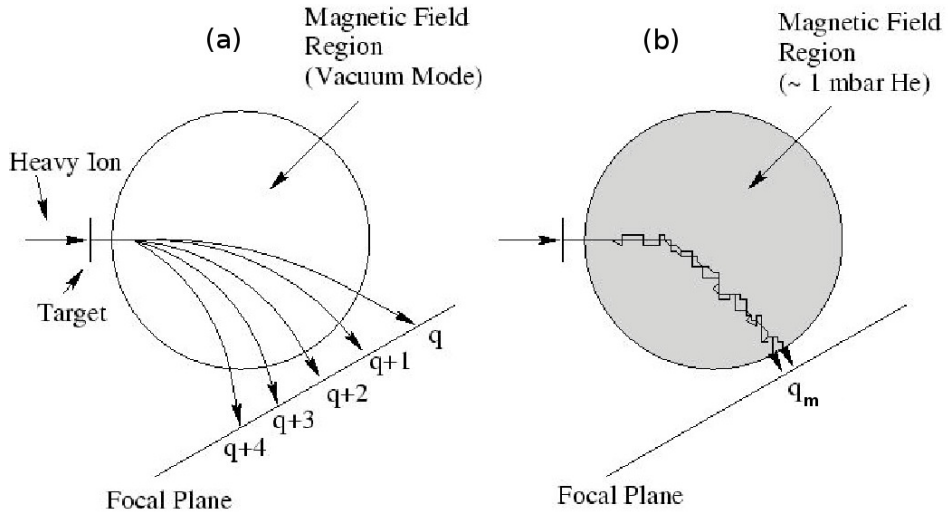

Figure 2.2: Ion path in (a) vacuum mode magnetic field and (b) gas filled magnetic region.

where $B\rho$ is the magnetic rigidity in Tesla meter (Tm), A and Z are the mass number and proton number of the ion respectively and $\alpha = \frac{1}{3}$. This formula is approximately valid in the velocity region

$$1 < \frac{v}{v_0} < Z^{\frac{2}{3}}$$

. Here v_0 is the Bohr velocity 2.19×10^6 m/s. Thus the magnetic rigidity is almost independent of the velocity and initial charge state distribution of the ions. Therefore the corresponding trajectories will be determined by the mass number A and atomic number Z of the ion. Thus charge focusing as well as velocity focusing takes place in a gas-filled separator, leading to high charge and momentum acceptances.

In general, the average or mean charge state q_m depends on v, Z and the type and pressure of the separator filling gas. Here, two competing processes will determine the degree of separation of ion trajectories, namely the charge-changing collisions and the broadening due to angular and energy straggling. There is the added problem of continuous reduction in the energy of ions in the gas medium which changes the magnetic rigidity. The gas pressure has to be optimized in the separator to get the smallest width or best resolution. The choice of the filling gas is important and depends on the reaction to be studied. Most of the devices are filled with He at < 1 Torr for conventional fusion studies. Dubna Gas Filled Recoil separator (DGFRS) is an exception, which use H_2 as the filling gas. H_2 requires higher field strength and leads to somewhat worse resolution but separation of transfer products is better with H_2. For accelerator mass spectrometry (AMS) applications (where relatively energetic ions are used and high resolution is needed) N_2 gas at ~ 10 mbar is used to achieve the required charge exchange statistics.

The gas filled separators are mostly used in the separation of evaporation residues of heavy and very heavy elements, from unwanted background. Gas-filled separators, alone or coupled to a detector array, offer an efficient, fast, compact and relatively inexpensive solution for nuclear structure studies. As a new application the gas-filled separator is used as a pre-separator in the study of chemical properties of the heaviest elements. Other uses are systematic study of fusion evaporation cross sections and for AMS measurements.

2.2.4.1 Rejection of primary beam in GFS

Using gas filled recoil separators, one can achieve very good primary beam rejection (in normal kinematics, involving asymmetric projectile and target system) but a poor mass resolution. The main contaminants are the target-like particles and in some cases, fission fragments. e.g. if we consider a primary beam of ^{16}O ions striking a ^{184}W

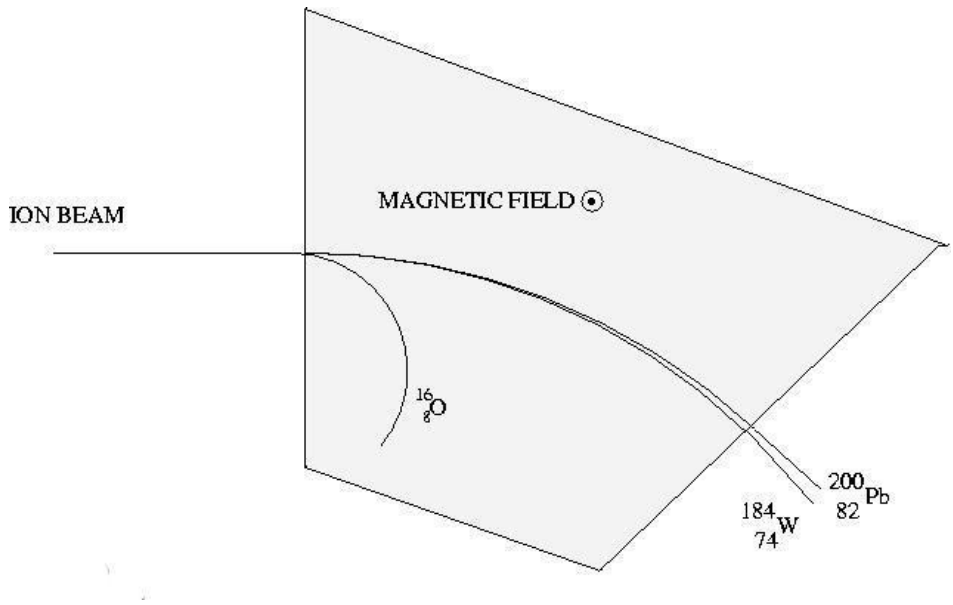

Figure 2.3: Qualitative representation of primary beam rejection in a gas filled mass separator.

target then we have scattered beam-like ^{16}O particles, target-like ^{184}W particles and the compound nucleus-like (^{200}Pb) particles which needs to be separated from the other two (see Fig. 2.3). If we calculate the quantity $\frac{m}{Z^{\frac{1}{3}}}$ (on which the magnetic rigidity depends), for each of these three particles, then for $^{16}_{8}$O

$$\frac{m}{Z^{\frac{1}{3}}} = \frac{16}{(8)^{\frac{1}{3}}} = 8 \tag{2.13}$$

for $^{200}_{82}$Pb

$$\frac{m}{Z^{\frac{1}{3}}} = \frac{200}{(82)^{\frac{1}{3}}} = 46.04 \tag{2.14}$$

for $^{184}_{74}$W

$$\frac{m}{Z^{\frac{1}{3}}} = \frac{184}{(74)^{\frac{1}{3}}} = 43.83 \tag{2.15}$$

Of these, the primary beam has lesser magnetic rigidity (i.e. by a factor of 5 or more) and the target-like nuclei have the rigidity similar (~ 90 %) to that of evaporation residues (ERs). Now if we set the magnetic field to get the $^{200}_{82}$Pb like ions at the focal plane then primary beam will be well separated but there may be a trace of target like particles also reaching the focal plane due to the comparable magnetic rigidity. The target-like particles can be distinguished from the ERs using time of flight method.

2.2.4.2 Advantages and disadvantages of gas filled recoil separators

Due to charge state focusing in a GFS, the discrete trajectories corresponding to different charge states coalesce around a trajectory defined by the mean charge state q_m of the ion. If a fine slit is put after the separator, a considerable part of the total flux will pass through it. Thus it gives a better transmission efficiency.

Vacuum mode separators are restricted to smaller gap size, due to limitations on maximum achievable electric field, which results in smaller angular acceptance and hence smaller transmission than GFS. Magnetic elements can have comparatively larger gap sizes, 0.40 m or more, and are not prohibitively expensive. The inevitable aberrations caused by such elements, is not a serious problem, as the image size and the obtainable resolution in any case is limited by multiple scattering and other effects like velocity dispersion of the average charge state.

Another advantage of gas filled separator is good primary beam rejection. The primary beam, having very less magnetic rigidity in normal kinematics, is bent maximum from its path whereas the other ions having more magnetic rigidities are bent less and a better beam rejection is achieved.

Some of the disadvantages are continuous energy loss of reaction products (by multiple collisions in the filling gas) and continuous multiple scattering. By multiple collisions, the ions are scattered and their direction changes many times. Ultimately the focusing is disturbed and the size of the image is larger. This results in a poor mass resolution. Further, due to the comparable magnetic rigidity, some of the target-like nuclei and/or fission fragments also reach to the focal plane along with the reaction products. These have to be rejected by employing special detection techniques such as TOF.

Gas filled separators use magnetic field elements only, since maintaining the required electric field in the gas atmosphere is not possible, while the pressure is ~ 1 mbar. Also scattering from the pressure window foil, used to separate the electric field region from the gas filled region, would seriously affect the performance of GFS.

2.3 HYbrid Recoil mass Analyzer (HYRA)

HYRA [9] is a dual mode, dual stage spectrometer/separator with its first stage capable of operating in gas filled mode in normal kinematics and both stages in vacuum mode, in inverse kinematics. The electromagnetic configuration of first stage of HYRA is QQ-MD-Q-MD-QQ, as shown in the Fig. 2.4, where Q stands for quadrupole and MD stands for magnetic dipole. The second stage configuration is QQ-ED-MD-QQ, where

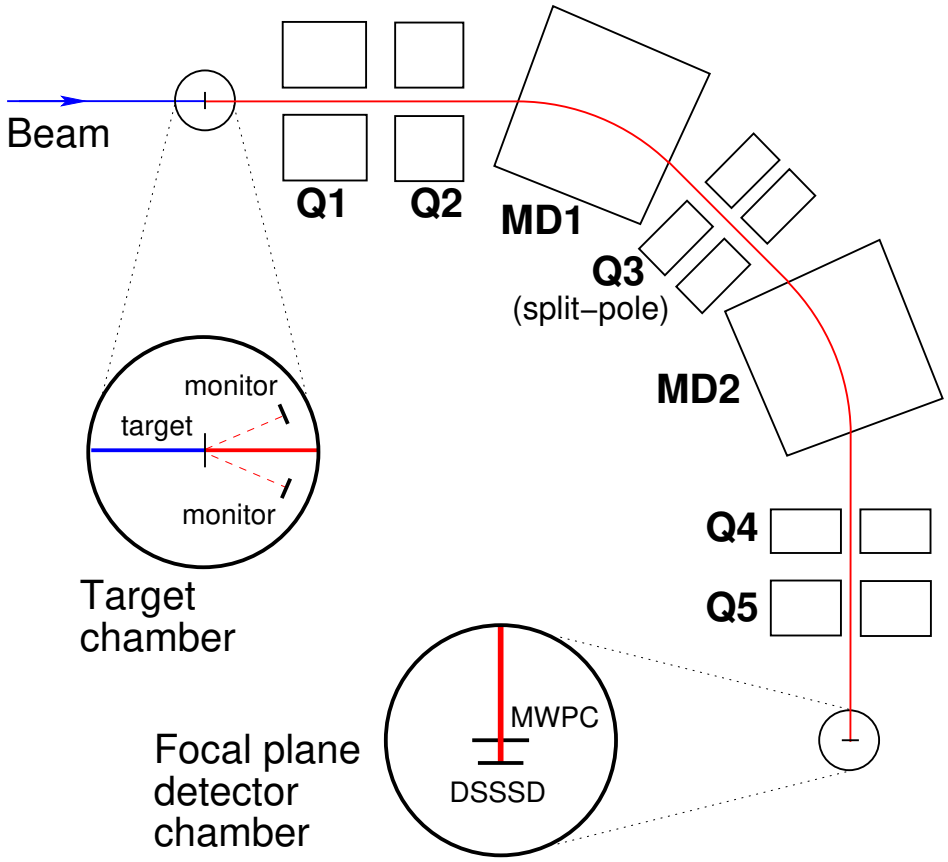

Figure 2.4: Schematic diagram of first stage of HYRA.

ED stands for electrostatic dipole. The first stage is capable of operating as momentum achromat in vacuum mode and in momentum dispersive mode in gas filled mode. The second stage will always be used in vacuum mode.

.

With two large 45° magnetic dipoles with 1.5 meter radius of curvature and 1.5 Tesla maximum magnetic field (i.e. 2.25 T-m magnetic rigidity), HYRA is capable of handling very heavy residues, and of providing a good beam rejection. The outer and inner radii of the first magnetic dipole vacuum chamber is provided with water cooled tantalum linings, in order to take away the heat produced due to excessive beam hitting. The straight through port of the same chamber is provided with a faraday cup, which is used for beam maximization, at the time of initial beam tuning.

There is a provision of sliding the quadrupole Q3 and chamber sideways, in a precise and reproducible manner on linear rails, in order to create space for focal plane detectors in gas filled mode for better transmission of low energy heavy ERs. The quadrupole Q3 is designed as split pole, with an intermediate space and port at the centre, for inserting the slits or beam stoppers, which can be used to allow selectively the ERs and stop

different charge states of primary beam. In the second stage also, the quadrupoles Q6 and Q7 have an arrangement for sideways movement, in order to create space for gamma detectors around the first focal plane in an experiment, if required. The electrostatic dipole (ED) of the second stage has curved anode and cathode plates machined from solid titanium and is capable of reaching voltages of $\pm$ 300 kV across a gap of 12 cm.

The high vacuum region of the beam line is separated from the gas filled region of the separator by a thin pressure window foil, which is normally a diamond like carbon foil [10] or Nickel foil [11] in this case. The whole spectrometer up to the detector window foil, is filled with Helium at $\sim$ 0.15 Torr. The gas pressure in the magnetic field region is maintained by a feed back loop. The Helium gas is inserted into the chamber through a solenoid valve, and continuously pumped out using a rotary pump. The solenoid valve is controlled through an MKS gas pressure controller having a set point for gas pressure. The actual gas pressure in the chamber is measured by a Beratron pressure gauge which sends the signal to the gas pressure controller. The controller compares the actual pressure with the set point and accordingly controlls the solenoid valve. After a few initial pressure fluctuations, the input and output of the gas attains an equilibrium and a continuous flow of helium gas at a required pressure, is maintained. The photograph of the first stage of HYRA, which was used in our measurements is shown in Fig. 2.5. Full layout of the separator HYRA, which will be used for other experiments is shown in Fig. 2.6.

Figure 2.5: Photograph of the first stage of HYRA.

Figure 2.6: Full layout of HYRA.

2.4 Detection system

The conventional detection system of HYRA, for ER measurements, consists of two silicon surface barrier detectors in the target chamber, kept at equal angles, for beam normalization. At focal plane a multi wire proportional counter (MWPC) is deployed, followed by a position sensitive silicon detector. In addition to this, occasionally germanium detectors or array of spin detectors (NaI) are placed at target site for ER gated gamma spectroscopy or ER gated spin distribution studies respectively. Sometimes the germanium detectors are placed around the focal plane detector, for isomer decay experiments.

2.4.1 Working of silicon surface barrier detector

A semiconductor detector is basically a reverse biased diode as shown in fig. 2.7. In its fully biased condition, the depletion region is maximum. Any radiation or particle entering the detector medium imparts its energy to the medium, which is used for ionization of the medium atoms. The charge produced is collected at the respective ends of the detector. The signal is processed normally through a charge sensitive pre-amplifier.

Semiconductor detectors have certain advantages over gas detectors. Average energy required for one electron-hole pair generation in semiconductor detectors is much less than that required for a gas detector. Due to this they give a better energy resolution. Also because of their greater density and hence stopping power, they are compact in size. At the same time they have certain disadvantages also. Some of the semiconductor detectors e.g. germanium detectors require cooling, whereas silicon detectors can work

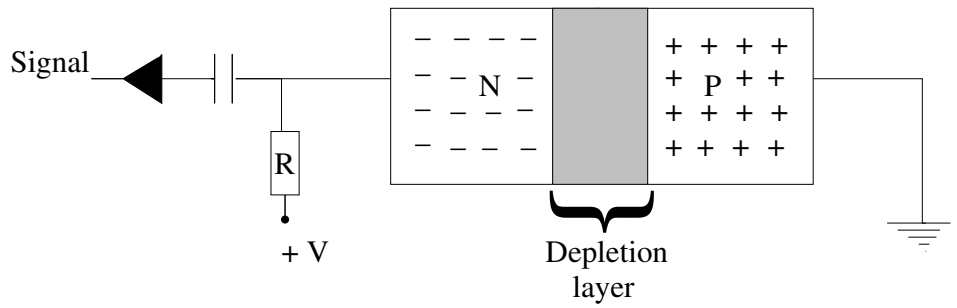

Figure 2.7: Schematic diagram of a semiconductor detector.

at room temperature. Also due to their crystal structure, semiconductor detectors are more prone to radiation damage and hence, have limited lifetime. Their detector medium can not be replenished unlike gas detectors. This makes them much costlier than the gas detectors. For charge particle detection, mostly silicon detectors are used. Different types of silicon detectors are silicon diode detectors, surface barrier detectors, ion-implanted detectors or diffused junction diodes categorized based on their methods of fabrication.

At times, it is important to have the position information of the incoming ions or ERs in our case, apart from energy and timing. For this one needs the position sensitive detectors. For position sensing purpose, there are two types of detectors using different methods of obtaining position information. One uses the continuous readout with a resistive charge division method and another uses a discrete array of readout elements. There are detectors which can provide one dimensional or two dimensional position information using these techniques. An schematic of a one-dimensional position sensitive detector with resistive charge division is shown in Fig. 2.8, along with a simplified circuit shown below. The detector has a uniform, resistive anode on the front and a low resistive back cathode. While passage of a charged particle through the detector, the amount of charge collected at contact B will be proportional to the energy E of the particle. Also it will be proportional to the resistance between the point of implantation of the charged particle and the other end, i.e.

$$Q_B = E.\frac{x}{L} \tag{2.16}$$

where x is the distance of point of incidence of the charged particle from the contact A, and L is the dimension of the resistive electrode. The charge signal on the back side of the detector (at point C) is proportional to the energy. Dividing signal at contact B with the total energy signal at C, will give

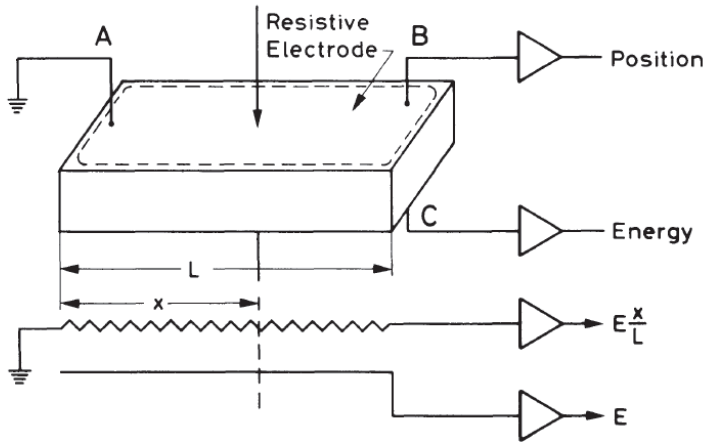

Figure 2.8: Schematic diagram of a position sensitive detector using resistive charge division [12].

$$x = L.\frac{Q_B}{Q_C} \tag{2.17}$$

In a similar manner, the position information from a two-dimensional detector is obtained, if the position signals are taken from all the four corners.

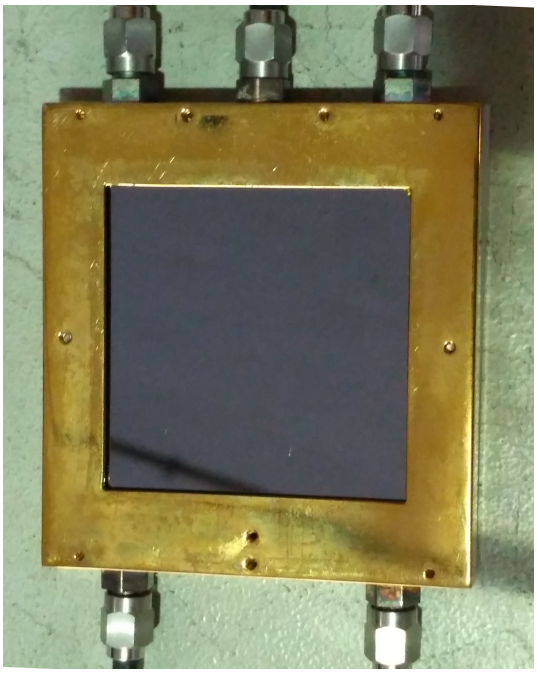

Figure 2.9: Photograph of a position sensitive silicon detector with resistive layer.

Fig. 2.9 shows one such detector of 5 $\times$ 5 cm^2 active area, which is in general a

limit to their size due to the difficulty in growing large area silicon wafers. The four connectors at the corners are for position signals, taken from the four corners of the front resistive anode. The top middle connector is for energy signal taken from the back. The semiconductor medium of the detector and the resistive layer on the front electrode should be highly uniform and homogeneous for the position signals to be linear. Also, correct shaping of the output signals is required and signal electronics for all the signals have to be properly gain matched. With proper care, nonlinearities could be less than 1% of the detector dimension and the spatial resolutions of the order of $\sim$ 250 μm, which is apparently the inherent limit of these detectors.

Unlike the continuous readout type detector, the discrete-type detector consists a series of individual electrode strips placed on a single semiconductor base. In this each strip behaves like a separate detector. Fig. 2.10 illustrates a simple one dimensional configuration. These detectors are also known as strip detectors while the two-dimensional discrete devices are called matrix detectors.

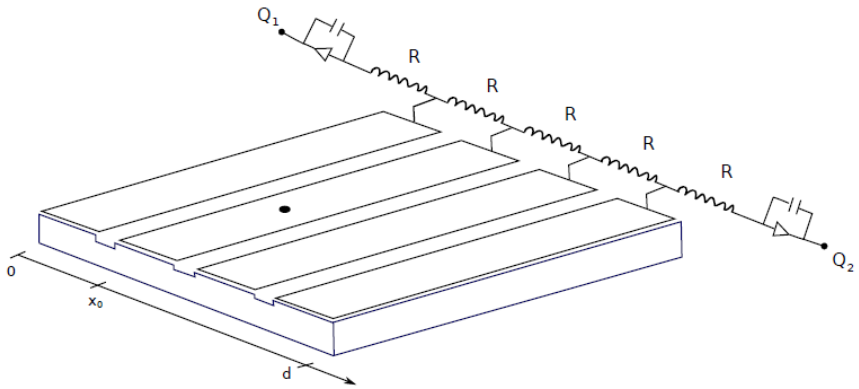

Figure 2.10: Schematic diagram of a strip detector [12].

Each electrode strip in discrete-detector acts as a separate detector and requires individual readout electronics e.g. preamplifier, amplifier etc. This makes it quite expensive and cumbersome. In the discrete-detectors, the signals may be processed through an external resistive network connected to the electrodes, to minimize the electronics, as shown in Fig. 2.10 and Fig. 2.11. However, after connecting an external readout circuit for resistive division of the charge, the discrete detector essentially becomes a continuous detector. However, discrete detectors give better timing and energy resolutions. The spatial resolutions is limited by the strip width only. Typical widths of these strips have been of the order of 0.2 - 0.4 mm. Fig. 2.12 shows one such detector.

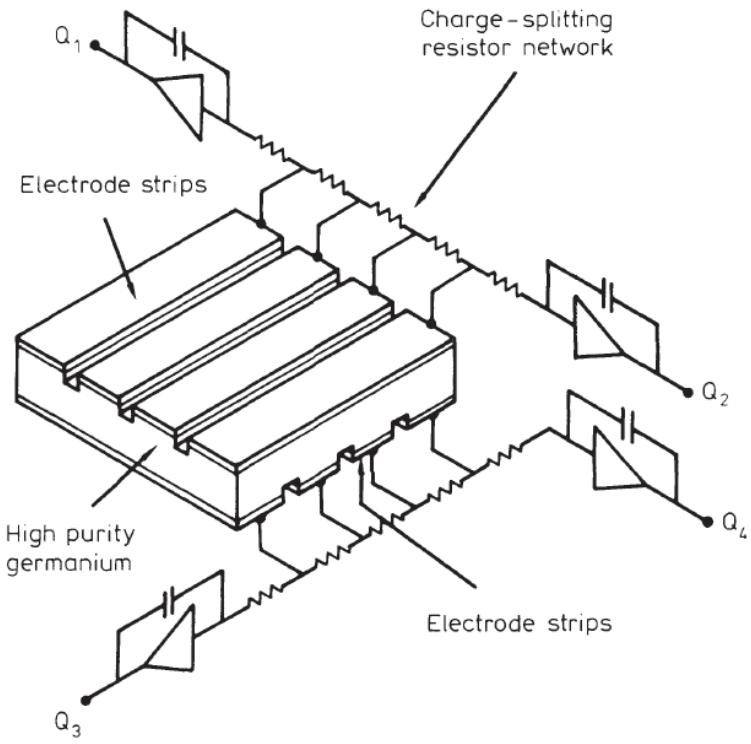

Figure 2.11: Schematic diagram of a two-dimensional strip detector [12].

Figure 2.12: Photograph of a strip detector.

2.4.2 Working of a gas detector

Gas detectors or gaseous ionization detectors were the first electrical devices developed for the detection of radiation. These devices are based on the direct collection of the charge carriers produced in a gas by passing radiation. The three basic gas devices, i.e. , the ionization chamber, the proportional counter and the Geiger-Muller counter are actually the same device working under different operating voltages and exploiting different phenomena. The basic configuration of a gas detector (Fig. 2.13) consists of a container, with conducting walls and a thin entrance window for radiation entrance. The container is filled with a suitable gas.

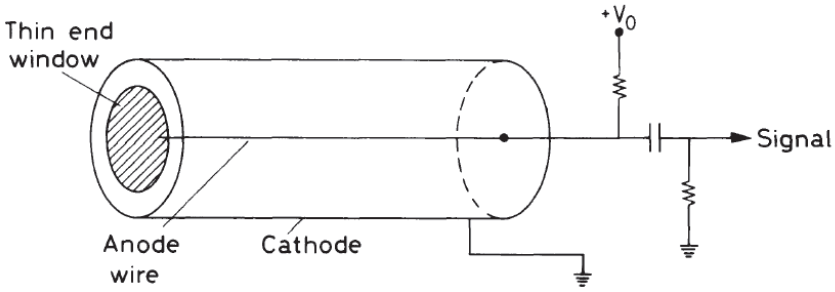

Figure 2.13: Basic configuration of a simple gas ionization detector [12].

When radiation penetrates the entrance window and reaches the gas medium, a certain number of electron-ion pairs will be created. The number of electron-ion pairs created is proportional to the energy deposited in the counter. Under the influence of the applied field, the electrons and the ions will be accelerated towards the anode and cathode respectively, where they are collected to give a charge or current signal.

The strength of the signal observed depends on the strength of the applied electric field as shown in Fig. 2.14 which shows the charge collected as number of ions versus applied voltage V. In absence of any applied electric field (i.e. at zero voltage), the electron-ion pairs generated will recombine under the influence of their own Coulomb attraction. As the field strength is increased, it slowly surpasses the Coulomb attraction and more and more number of charge carriers are collected before they can recombine. At certain voltage, all the electron-ion pairs generated will be collected and further increasing the voltage will have no effect on the signal strength. This corresponds to the first plateau of the curve. The gas device working in this flat region (II) is termed as ionization chamber as they utilize the charge carriers produced directly by the incident radiation. The signal current is very small. Ionization chambers are used generally as

monitoring instruments for large fluxes of radiation.

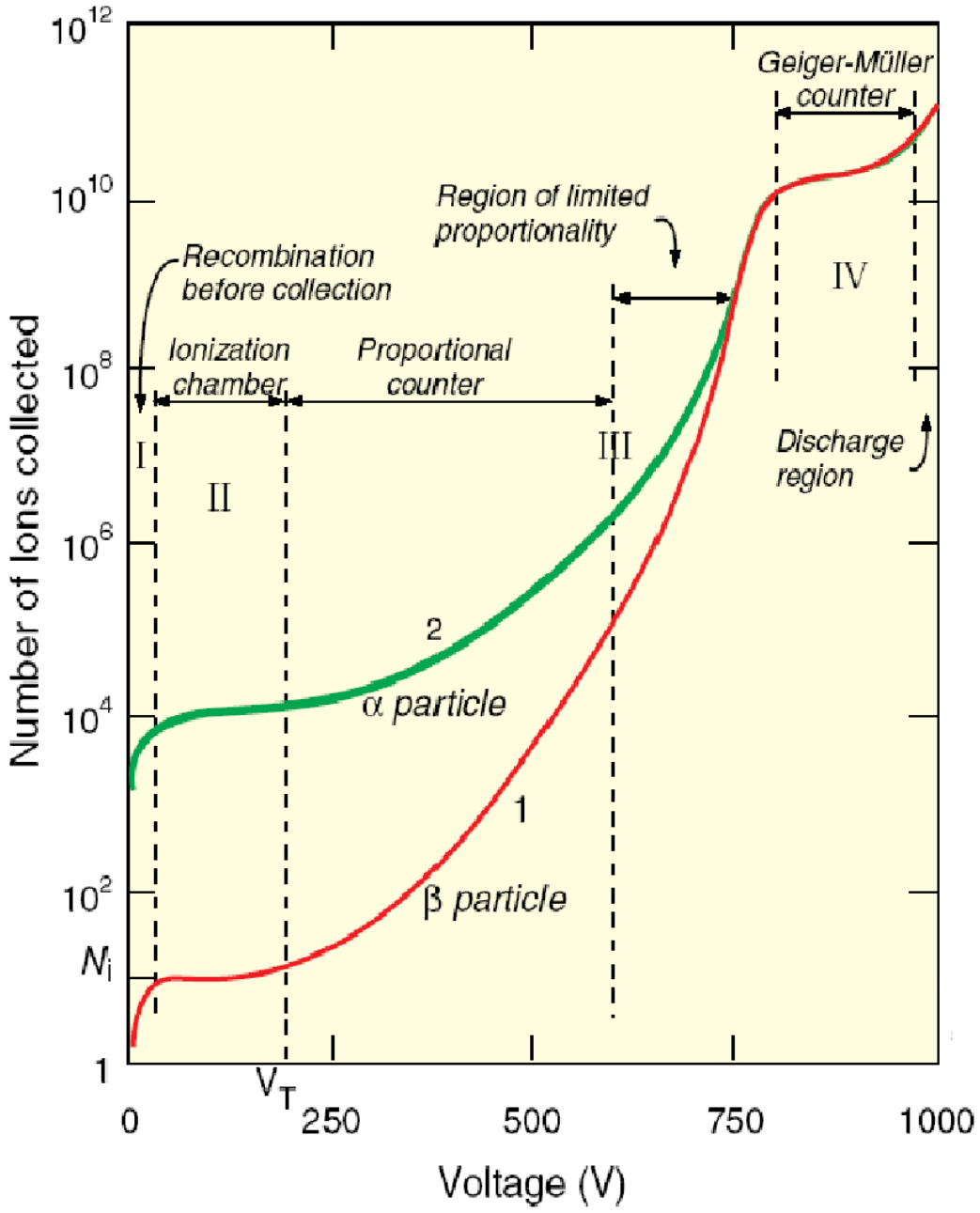

Figure 2.14: Number of ions collected versus applied voltage in a single wire gas chamber [12].

Increasing the voltage beyond region II, again increases the signal current. Here the field is strong enough to accelerate the electrons (produced in primary ionization) to create secondary and tertiary ionization and so on, which results in an avalanche or cascade. The electric field being strongest near the anode, the avalanche takes place quickly and almost entirely within a few radii of anode wire. Still the number of

electron-ion pairs in the avalanche is proportional to the number of primary electrons with a multiplication factor as high as 10^6, depending upon the working voltage V. This region of proportional multiplication extends up to point III. A detector operating in this region is called proportional chamber.

On further increasing the voltage beyond point III, the total amount of ionization produced via multiplication becomes so large that the space charge created distorts the electric field about the anode and the proportionality begins to be lost. This region is termed as region of limited proportionality and is not good for working of any device.

Further increase in the voltage triggers a chain reaction of many avalanches spread out along the entire length of the anode wire, instead of a single, localized avalanche at some point along the anode wire (as in a proportional counter). The source of these secondary avalanches are the photons emitted by de-exciting molecules traveling to other parts of the detector to cause further ionization. The output current becomes completely saturated and is independent of the energy of the initial event. A quenching gas mixed in the detector gas can help in stopping this discharge, by absorbing these photons and drain their energy into other channels. Detectors operating in this region are known as Geiger-Muller (GM) or breakdown counters. The Geiger voltage region is characterized by a plateau over which the signal strength exhibit a very little variation. The width of the plateau depends on the effectiveness of the quencher in the gas. generally, the working voltage of a GM counter is chosen to be in the middle of the plateau so that any variations due to voltage drift can be minimized.

Any further increase in the voltage, beyond the plateau will cause a continuous breakdown even without a radiation. This region, of course, is to be avoided to prevent damage to the counter.

A filling gas for proportional counters should have low working voltage, high gain, good proportionality and high rate capability. In general, all these properties are not met by a single gas, therefore a mixture of gases is used. In conventional proportional counters a commonly used mixture is 90% Ar and 10% methane (CH_4). This mixture is also known as P10 gas. Another often used detector gas is isobutane.

For nuclear reaction experiments we mostly use proportional counters. Just like semiconductor detectors, they can also be made position sensitive. This can be done by resistive charge division or introducing delay line chain. The method of charge division is analogous to that already discussed for silicon detectors. The charge collected at either end of a resistive anode wire is divided in proportion to the length of the wire from the point at which the charge is injected to the other end (see Fig. 2.15).

The proportional counter can be made position sensitive, by making multi wire

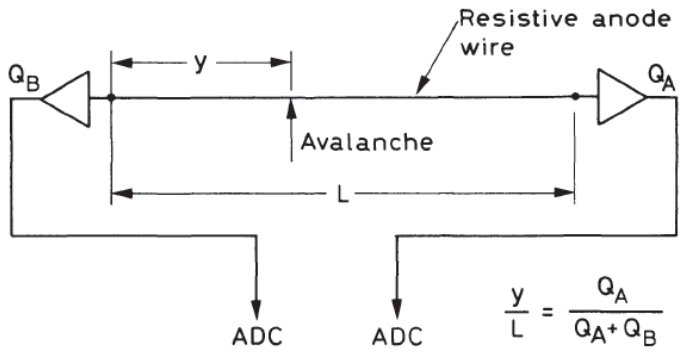

Figure 2.15: Charge division method for position readout in multi wire proportional counter [12].

proportional counter. This is analogous to putting multiple proportional counters in a single container. Basically multiple wire anodes are connected by a resistive chain or a delay line chain as shown in the Fig. 2.16. In this technique, external delay lines are coupled to the cathode or anode planes of the chamber. Using the anode signal or some other triggering signal as a start, the time difference between the arrival of the signals at both the ends of the delay line are measured. This then yields the two coordinates of the avalanche. Signals from one anode plane give X coordinate and the signals from an orthogonal mounted second frame can give coordinates in Y.

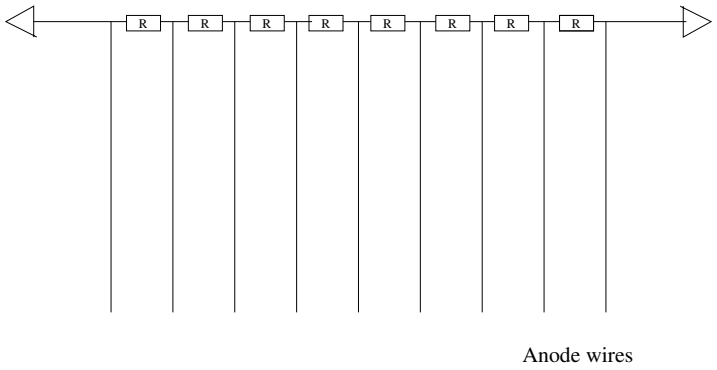

Figure 2.16: Resistive chain or delay line for position information in multi wire proportional counter.

2.4.3 Fabrication and testing of multi wire proportional counter

During the course of this work, a multi wire proportional counter with an active area 150 $\times$ 50 mm^2 was developed and fabricated [13]. It is of four electrode geometry, Cathode, X position electrode, anode and Y position electrode. Fig. 2.17 shows a schematic of the detector geometry.

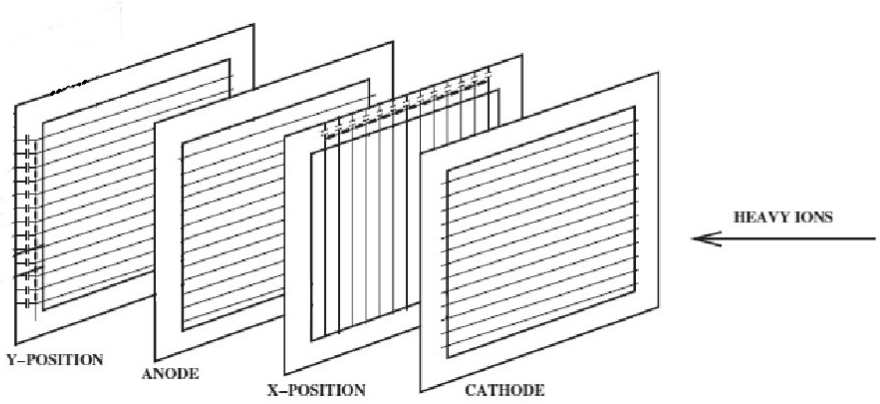

Figure 2.17: Schematic representation of the multi wire proportional counter with four electrodes.

The inter electrode gap was kept 3.2 mm. Electrodes were wire frames, made from 20 μm diameter gold plated tungsten wires with an inter wire spacing of 50 mill (1.27 mm). Thus X position frame has 120 wires and Y position frame has 40 wires. Every two adjacent wires were shorted together. A fixed delay of 2 ns was provided between these sets of shorted wires using delay line chips. Each chip had 10 taps and a delay of 2 ns per tap. End to end delay in X position frame is 120 ns and in Y position frame it is 40 ns. Position information is derived from these wire frames by taking the timing signals through both the ends. Isobutane gas was used as the detector medium. A 0.5 μm thick mylar foil was used as detector window foil. Fig. 2.18 shows a photograph of the developed multi wire proportional counter. This detector [13] is presently installed at the focal plane of the vacuum mode separator HIRA [6], and has been successfully used in several in beam experiments. A detector with quite similar geometry and dimensions [14], earlier installed at the focal plane of the gas filled separator HYRA, was used for the present study.

During the initial testing of the newly fabricated detector, it was operated at isobutane pressure $\sim$ 5 mbar (at the inlet) and anode and cathode bias +460 V and -200 V, respectively. The detector was tested with an ^{241}Am alpha source placed in front of it at a distance of around 265 mm. The MWPC has total of six output signals,

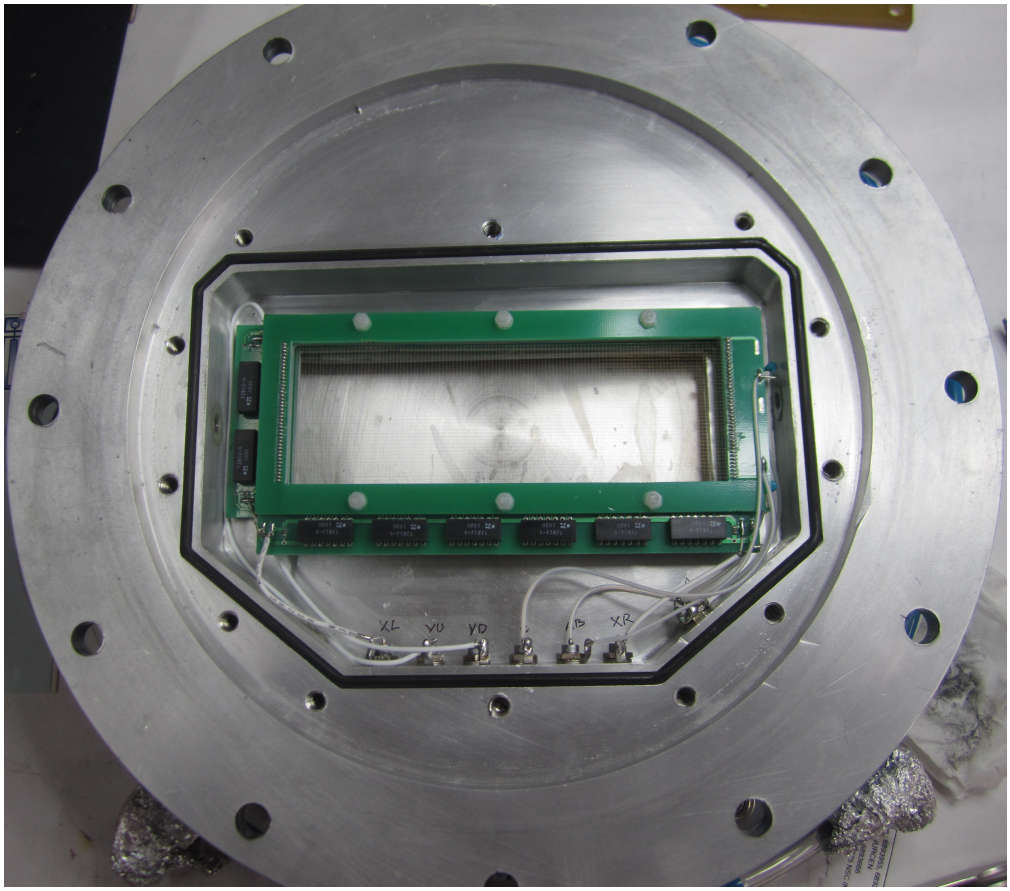

Figure 2.18: Photograph of the developed multi wire proportional counter.

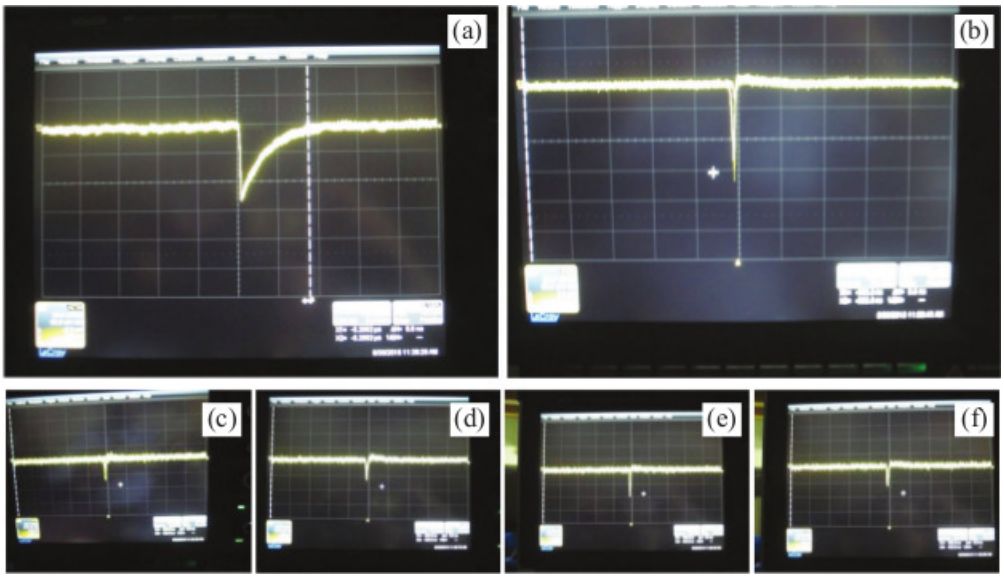

Figure 2.19: Multi wire proportional counter signals (a) cathode, (b) anode, (c) X-left, (d) X-right, (e) Y-up, and (f) Y-down, at preamplifier level.

anode, cathode, two X position signals X-left (XL) and X-right (XR) from both ends of the X position electrode, similarily two Y position signals Y-up (YU) and Y-down (YD) from the two ends of Y position electrode. Fig. 2.19 shows the detector signals at preamplifier level. The detector signals at preamplifier level were quite strong and clean. With alpha source and the above said operating parameters, the anode signal was$\sim$300 - 400 mV, cathode $\sim$200 mV and position signals were $\sim$ 30-40 mV.

Fig. 2.20 shows the two dimensional position spectra with X and Y positions on either axis, with an alpha source placed in front of the MWPC. It can be seen that the detector is uniformly illuminated.

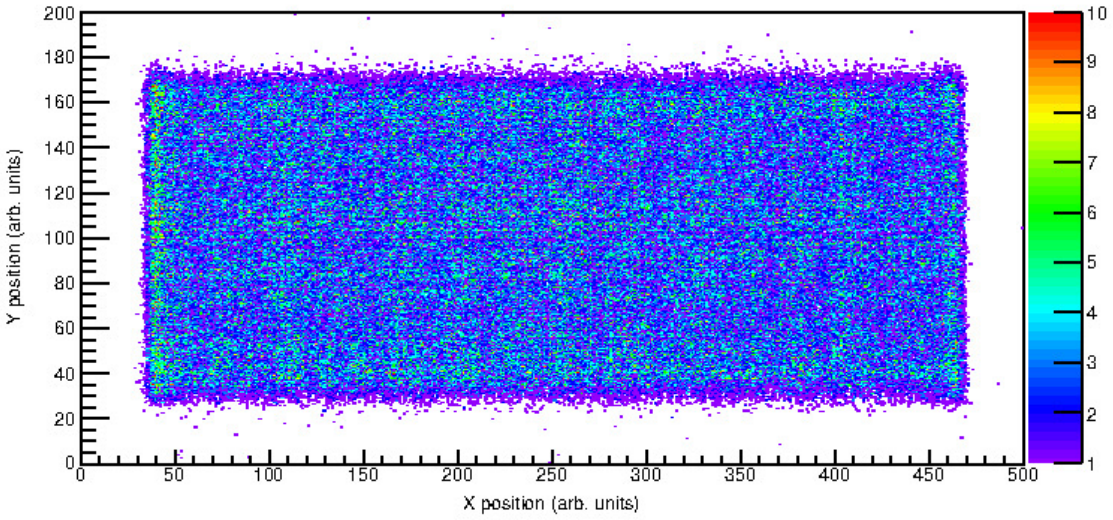

Figure 2.20: Two dimensional position spectrum with an alpha source placed in front of the multi wire proportional counter.

The detector had been tested for position resolution using ^{241}Am alpha source. A mask having 1 mm diameter holes with 5 mm separation in X and Y direction was placed before the detector, approximately 5 mm from the detector electrodes. Am^{241} alpha source was placed approximately 265 mm from the mask. Fig. 2.21 show the two dimensional position spectra (with X and Y positions on either axis) with an alpha source placed in front of the MWPC, and the mask placed in between the source and the detector respectively.

In two dimensional spectrum with the mask, one can see the particles passing through holes are reproducing the mask, and the detector is almost uniformly illuminated. Fig. 2.22 shows X and Y individual position spectra collected with mask. A position resolution in X and Y direction could be estimated using these individual position spectra. Position resolution in X was estimated to be $\sim$ 1.6 mm and in Y $\sim$ 1.7 mm.

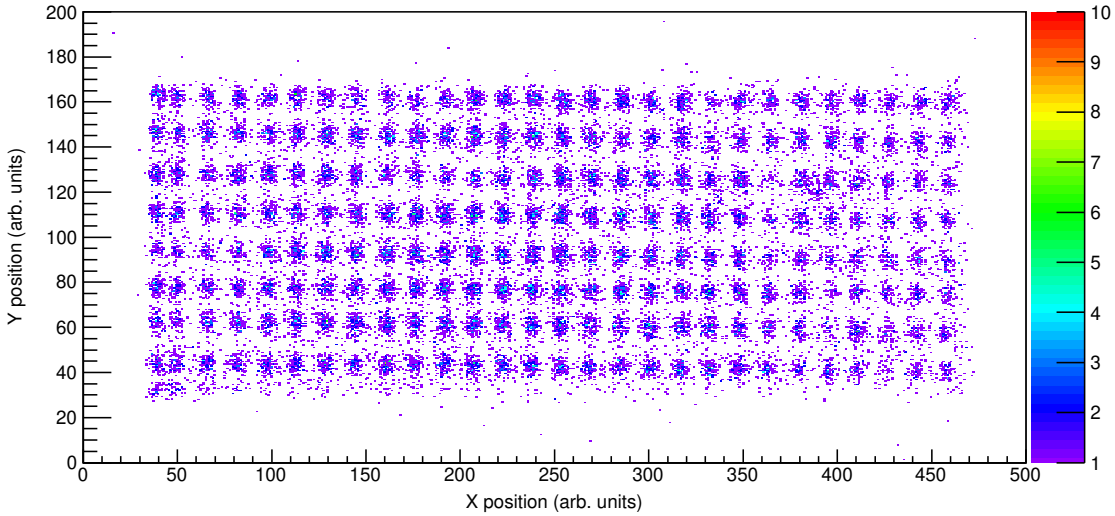

Figure 2.21: Two dimensional position spectrum with a mask placed in between alpha source and the multi wire proportional counter.

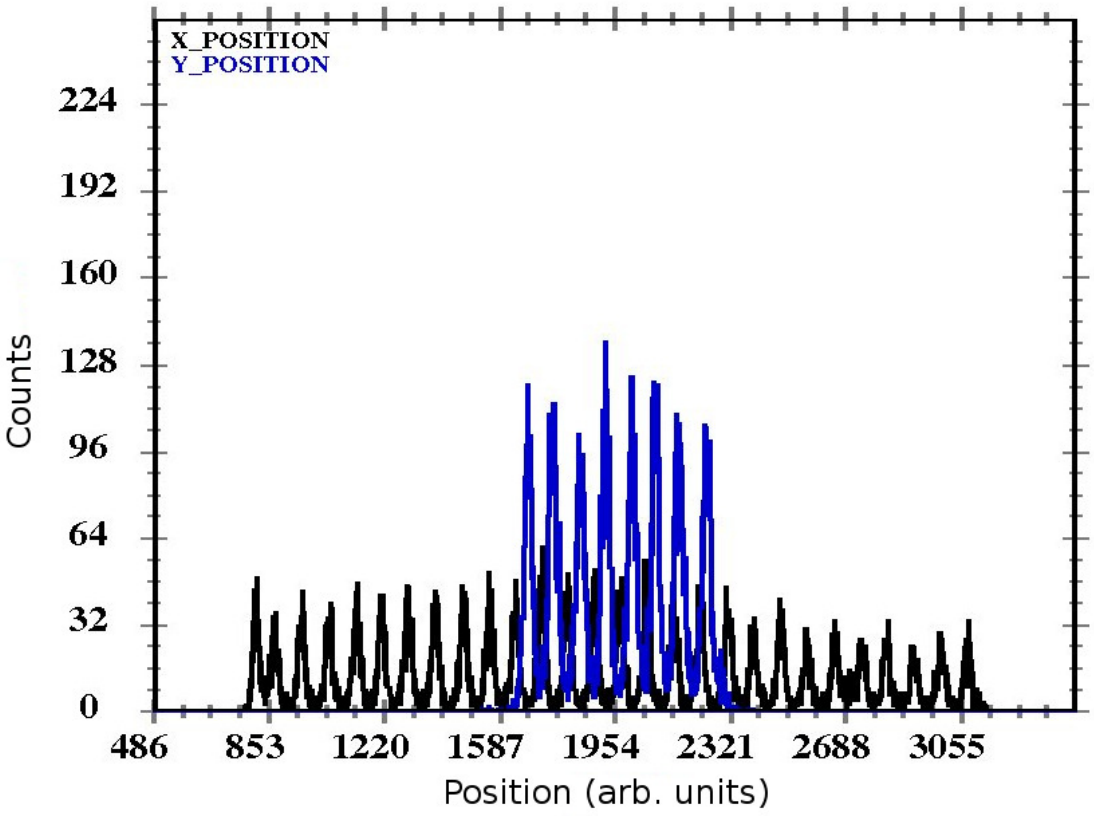

Figure 2.22: X and Y position spectra using a mask before multi wire proportional counter.

2.4.4 Electronics

Monitor detector signals were processed through ORTEC made 142IH pre-amplifiers. IUAC inhouse developed dual channel spectroscopy amplifier cum discriminator module [15] was used to amplify the monitor detector signals and generate individual timing signals, which were used along with other signals for generating the master strobe for data acquisition.

The MWPC has total of six output signals, anode, cathode, XL, XR, YU and YD. Anode is the fastest signal, so taken as timing start, and is processed through a non inverting fast current sensitive pre-amplifier ORTEC VT120A. All four position signals are processed through the IUAC in house developed ORTEC VT120B equivalent fast current sensitive pre-amplifiers [16] of inverting type. This detector being a transmission type detector, the cathode signal gives the energy loss (ΔE) information instead of total energy. The cathode signal was processed through ORTEC made 142IH charge

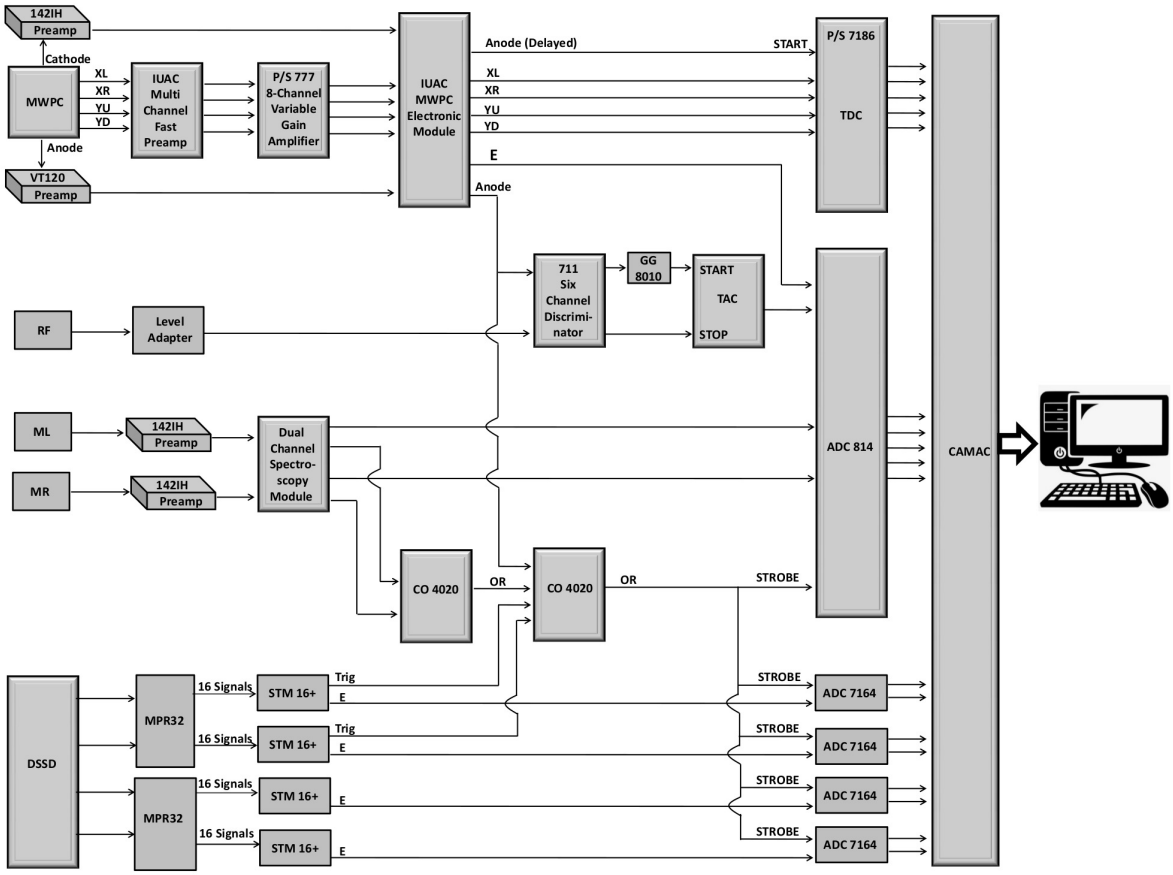

Figure 2.23: Electronic circuit diagram for the data acquisition.

sensitive pre-amplifier. Cathode bias was given through the same 142IH charge sensitive pre-amplifier. Anode bias was supplied directly to the detector, as the preamplifier VT120A doesn't have a inbuilt biasing circuit. After pre-amplification, all the position signals are amplified through a Phillips Scientific made variable gain amplifier 777. Anode signal being stronger, generally doesn't require further amplification. Further all the timing signals (anode and all the position signals) are fed to an IUAC made MWPC electronic module [17], which is in fact a combination of compact multi channel constant fraction discriminator (CFD) and gate and delay generator(GDG). Cathode signal is also amplified through an inbuilt shaping amplifier in the same MWPC electronic module. Sometimes a separate shaping amplifier ORTEC 571 is used for cathode signal amplification. From the output of this module, anode is taken as START for a Phillips Scientific made time to digital converter(TDC) used in common start mode. All the four position signals are used as individual STOPs. TDC records individual timings at all the four ends, for a single event, with respect to the anode. These individual timings are then utilized for constructing a realistic position spectrum of the particles reaching the focal plane MWPC. The ΔE signal along with the monitor detector signals, is recorded in IUAC made analog to digital converter (ADC) ADC814. A TOF was set among the beam pulsing RF signal and the MWPC anode using a time to analog converter (TAC). This TOF signal is recorded using the ADC814.

A double sided silicon strip (DSSD) is placed behind the MWPC. The DSSD has total 64 strips. 32 vertical strips in the front for X position and 32 horizontal strips at the back for Y position. Two multi channel charge sensitive preamplifiers MPR-32 from Mesytec, one each for front and back, were used to preamplify the DSSD energy signals. Four STM16+ shaping / timing filter amplifier with discriminator and multiplicity trigger from Mesytec were used for shaping and amplification of these signals. These signals are then recorded using four analog to digital converters (ADC) model ADC 7164 from Phillips Scientific. Each ADC 7164 can record maximum 16 signals.

For constructing a master strobe for all the five ADCs, a logical OR of anode CFD signal from MWPC electronic module and trigger of both the monitor detectors from dual channel spectroscopy cum discriminator module is constructed using ORTEC CO4020 coincidence unit. This OR signal is further ORed with the trigger from the two STM16+ modules employed for DSSD front strips to give final master strobe. This strobe is given to all the ADCs, which decides when the input signals will be digitized. This strobe is normally kept 4-5 μs wide. Any analog signal which is time aligned to fall within this gate, is digitized by the ADC. The data acquisition is carried out using a indigeneously developed data acquisition software CANDLE [18].

In a recent development, a compact multi channel fast pre-amplifier for MWPC

was developed at IUAC [19], with anode, position and cathode inputs and outputs. It operates on ± 12V DC and does not require a NIM bin. One such module is sufficient for preamplifying signals from one MWPC. Fig. 2.23 shows the block diagram of the electronic setup used with the MWPC and other detectors during the present measurements.

2.5 Experimental details

The measurements reported in this work, were carried out at the 15 UD Pelletron accelerator facility of IUAC, New Delhi (India) [1, 2]. A pulsed beam of ^{16}O was used to bombard ^{203}Tl, and ^{205}Tl targets [20, 21] of thicknesses $\sim$ 175 ± 10 μg/cm^2, and 155 ± 10 μg/cm^2 respectively with thin ($\sim$ 35 μg/cm^2) carbon backing. Experiment was carried out at laboratory projectile energies ($E_{\rm lab}$) in the range of 82–113 MeV. ERs were separated from the background events using first stage of HYRA [9] operated in gas-filled mode. Magnetic field region was filled with helium gas at a pressure of 0.15 Torr. Gas-filled region was separated from beam line vacuum using a diamond-like carbon foil of $\sim$ 3 μm thickness and 15 mm diameter. In the target chamber, two SSBD monitor detectors were placed at laboratory angle of 25°, with respect to the beam direction, in the horizontal plane, for absolute normalization of ER cross sections. At the focal plane (FP) of HYRA, an MWPC [14], having an active area of 15.0×5.0 cm^2, followed by a double sided silicon strip detector (DSSD), were used to detect the ERs. A very thin (0.5 μm) mylar foil was used as the entrance window of the MWPC, in order to minimize the ER energy loss prior to its detection in the MWPC. Effective active area of the MWPC was reduced to 11.0×5.0 cm^2, due to the size of the foil supporting flange. The MWPC was operated at $\sim$ 3 mbar of isobutane. Magnetic fields were optimized around the calculated values, at each energy point, by maximizing the ER yield at the focal plane. Time of flight (TOF) of the ERs were recorded taking MWPC anode signal as $START$ and RF signal of beam pulsing system as $STOP$. Yields of ERs were extracted from the coincidence spectrum between energy loss ΔE (from the cathode of MWPC) and TOF. Fig. 2.24 shows a typical two dimensional spectrum of ΔE vs TOF obtained at E$_{lab}$ = 97.4 MeV for ^{16}O + ^{203}Tl. The ractangular gate in the figure shows the ER events.

The DSSD was placed behind the MWPC for ER implantation and their mass identification via characteristic alpha decay. However, it was not possible to identify individual ER channels separately due to few technical limitations, e.g. the DSSD had a thick dead layer causing huge energy loss of ERs in it. ERs produced at certain beam

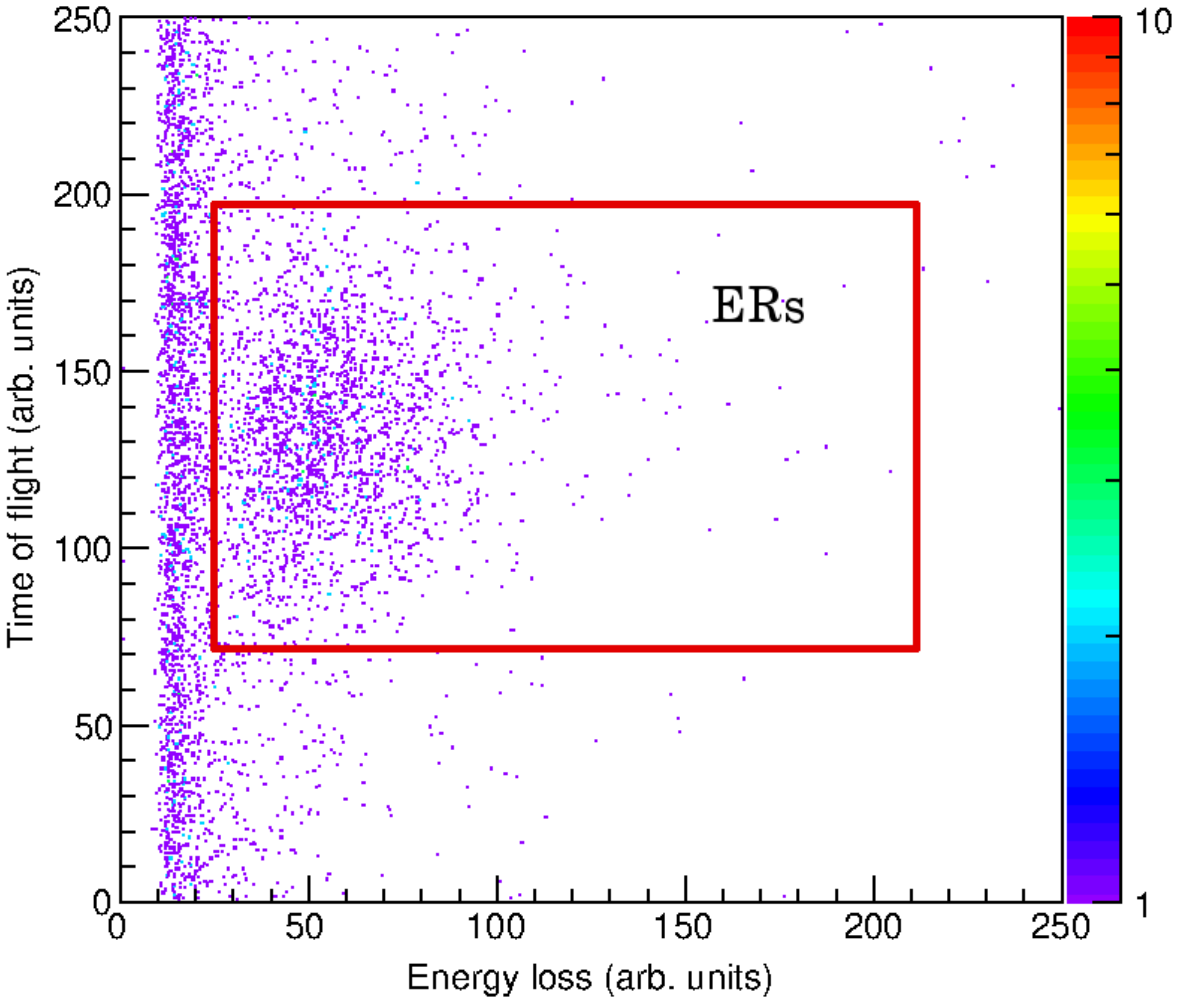

Figure 2.24: Two dimensional spectrum of ΔE vs TOF for ^{16}O + ^{203}Tl at 97.4 MeV.

energies could not penetrate the dead layer to reach the detector's active volume. Moreover, it was not possible to distinguish the ERs, their alpha decay or the delayed alpha decay of previously embedded ER (inside DSSD) or its daughter nuclei. The Alpha decay energies in these nuclei are very close. The detector and electronics resolution didn't permit to unambiguously identify them. Therefore the individual ER channel cross-sections could not be evaluated. However, for total ER cross section estimation we could extract ER events from the ΔE vs TOF spectra at each energy.

Bibliography

[1] G. K. Mehta and A. P. Patro, Nucl. Instr. and Meth **A 268**, 334 (1988).

[2] D. Kanjilal, S. Chopra, M. M. Narayanan, I. S. Iyer, V. Jha, R. Joshi, and S. K. Datta, Nucl. Instr. and Meth **A 328**, 97 (1993).

[3] J. Gehlot and N. Madhavan, Study Course Report, submitted to library, IUAC, New Delhi, **May** (2004).

[4] C. E. Dullmann, Nucl. Instr. and Meth. B **266**, 4123 (2008).

[5] C. N. Davids, Nucl. Instr. and Meth. B **204**, 124 (2003).

[6] A. K. Sinha, N. Madhavan, J. J. Das, P. Sugathan, D. O. Kataria, A. P. Patro, and G. K. Mehta, Nucl. Instr. and Meth. A **339**, 543 (1994).

[7] M. Leino, Nucl. Instr. and Meth. B **204**, 129 (2003).

[8] A. Ghiorso, S. Yashita, M. E. Leino, L. Frank, J. Kalnins, P. Armbruster, J.-P. Dufour, and P. K. Lemmertz, Nucl. Instr. and Meth. A **269**, 192 (1988).

[9] N. Madhavan, S. Nath, T. Varughese, J. Gehlot, A. Jhingan, P. Sugathan, A. K. Sinha, R. Singh, K. M. Varier, M. C. Radhakrishna, E. Prasad, S. Kalkal, G. Mohanto, J. J. Das, R. Kumar, R. P. Singh, S. Muralithar, R. K. Bhowmik, A. Roy, R. Kumar, S. K. Suman, A. Mandal, T. S. Datta, J. Chakko, A. Choudhury, U. G. Naik, A. J. Malayadri, M. Archunan, J. Zacharias, S. Rao, M. Kumar, P. Barua, E. T. Subramanian, K. Rani, B. P. A. Kumar, and K. S. Golda, Pramana -Journel of Physics **75, No.2**, 317 (2010).

[10] www.micromatter.com/FoilsforBeamStripping.aspx, .

[11] J. Gehlot, S. R. Abhilash, T. Varughese, and D. Kabiraj, Proceedings of the DAE Symp. on Nucl. Phys. **58**, 932 (2013).

[12] W. R. Leo, Techniques for Nuclear and Particle Physics Experiments, Springer-Verlag Berlin Heidelberg GmbH **Nov.** (1993).

[13] J. Gehlot, A. Jhingan, and T. Varughese, IUAC Annual report , page 92 (2015-16).

[14] A. Jhingan, P. Sugathan, S. Kalkal, G. Mohanto, T. Varughese, N. Madhavan, S. Nath, J. Gehlot, and E. T. Subramaniam, Proceedings of the DAE Symp. on Nucl. Phys. **56**, 1096 (2011).

[15] A. Gupta, S. Venkataramanan, and P. Sugathan, Proceedings of the DAE Symp. on Nucl. Phys. **58**, 928 (2013).

[16] A. Jhingan, Pramana-Journel of Physics **85**, 483 (2015).

[17] S. Venkatramanan, A. Gupta, A. Jhingan, and P. Sugathan, Proceedings of the DAE Symp. on Nucl. Phys. **56**, 1084 (2011).

[18] E. T. Subramaniam, B. P. AjithKumar, and R. K. Bhowmik, http://www.iuac.res.in/NIAS .

[19] A. Gupta, J. Gehlot, S. Nath, and S. Venkataramanan, Proceedings of the DAE Symp. on Nucl. Phys. **63**, 1078 (2018).

[20] J. Gehlot, S. R. Abhilash, S. Ojha, D. Mehta, D. Kabiraj, and A. M. Vinodkumar, Proceedings of the DAE Symp. on Nucl. Phys. **57**, 896 (2012).

[21] J. Gehlot, S. R. Abhilash, S. Ojha, D. Mehta, D. Kabiraj, and A. M. Vinodkumar, J. Radioanal. Nucl. Chem. **305**, 755 (2015).

Chapter 3

Target and window foil fabrication and Characterization

In any nuclear reaction experiment, a target of suitable thickness and purity plays a crucial role. A thick target increases the product yield but reduces the experimental resolution because of energy loss of primary beam as well as reaction products, in the target material. A thin target, on the other hand, provides better energy resolution but reduced product yield, and therefore requires a longer beam time or higher beam current. Keeping these points in mind, the target thickness should be optimum depending upon the experimental requirements. The properties of the target material, like, hardness, high melting point, chemical properties (e.g. oxidation), toxicity etc., sometimes make its preparation very challenging. The cost of the isotopic materials is also a major issue. These factors make the procedure of fabrication of a target highly important. For soft and malleable materials, the target can be rolled down to a desired thickness, however, this technique has its limitations at very low thicknesses. For hard materials and for low thicknesses, the techniques like vacuum evaporation, ion beam sputtering or electro-deposition etc. are used [1].

For experimental requirements of the present thesis work, a target of thickness $\sim$ 200 μg/cm^2 is found suitable. A self-supporting target is always a first choice for such studies. However, a target with a suitable backing is opted if it is not possible to make a self supporting target of the desired material. The backing is always preferred to be of low Z material and as thin as possible in order to minimize the energy loss and straggling of beam before reaching the actual target material. In most of the cases a thin carbon foil of few tens of μg/cm^2 thickness serves the purpose. For the present work, ^{16}O + ^{203}Tl and ^{16}O + ^{205}Tl reactions were measured using the gas filled separator HYbrid Recoil mass Analyzer (HYRA) [2] at IUAC, New Delhi, which required thin isotopic targets of Tl. Therefore, we attempted to fabricate isotopic targets of ^{203}Tl

and ^{205}Tl.

Several investigators had prepared Tl films or targets by various methods [3–19] . Most of them had used natural Tl (29.5 % ^{203}Tl, 70.5 % ^{205}Tl) as the material [3–13] and several approximations had to be made to determine whether the reaction occurred on ^{203}Tl or ^{205}Tl. Only a limited number of attempts were made with isotopic Tl material [14–19], mainly for making thick targets by molding, electro-deposition or evaporation on metal backing. Here we present a complete fabrication procedure of thin isotopic Tl transmission targets, by vacuum evaporation [20, 21].

Tl is soft and can be cut with a knife at room temperature. It has a metallic lustre, however, it quickly changes its colour (somewhat similar to lead) when exposed to air due to the build up of a heavy layer of oxide. Tl makes thallium hydroxide in presence of water. Tl is highly toxic, therefore it should be handled very carefully and its contact with eyes and skin must be avoided. For avoiding passive inhaling, a mask must be used. Our first choice was to make a self-supporting target of Tl. However, we could not succeed in floating the evaporated target film on the frame, therefore, we decided to opt for a target with thin carbon backing.

3.1 Experimental Procedure

3.1.1 Experimental set-up

Targets were prepared at the target laboratory of IUAC. A coating unit (see Fig. 3.1) with a diffusion pump was used to prepare the targets. The minimum pressure attainable in the evaporation chamber is of the order of 10^{-7} mbar. The unit is equipped with a resistive heating system as well as a 2 kW electron gun with water-cooled copper crucible. Resistive heating is used for evaporating the materials with comparatively lower melting point, however, for evaporating the materials having high melting points, an electron gun is used. For controlling the deposition to achieve the desired thickness, a manual shutter is provided with the chamber which can shadow the substrate whenever required. Further, the monitoring of the deposition rate and the thickness of the deposited layer can be done online with the help of a quartz crystal thickness monitor.

The whole setup including the chamber body, electron gun crucible, thickness monitor, feedthroughs of resistive heating set-up and diffusion pump body are maintained at low temperature by the circulation of chilled water through them. The chamber gate valve and diffusion pump have a liquid nitrogen (LN_2) trap fitted between them. This is a metal container filled with LN_2, which stops oil molecules of diffusion pump from moving towards the evaporation chamber, by condensing them and hence provides an

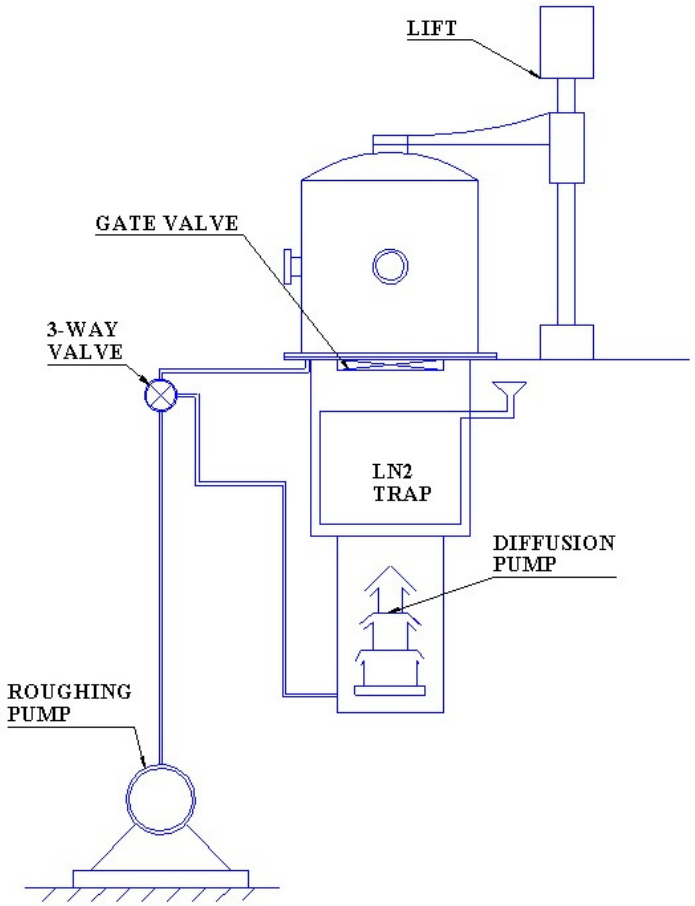

Figure 3.1: Schematic diagram of the coating unit.

oil free vacuum.

3.1.2 Preparation of carbon backing foils

The above mentioned diffusion pump based coating unit is used to prepare the carbon foils. In this process, cleaned glass slides were mounted at a distance of $\sim$ 15 cm from source. First, a layer of $\sim$ 100 nm of releasing agent ($BaCl_2$) was deposited on glass slides by resistive heating. For this a pellet of $BaCl_2$, made using hydraulic pellet press, was put in a tantalum boat and then evaporated by resistive heating. Then a layer of required thickness of carbon was evaporated over $BaCl_2$ by electron gun. The source is made of a smooth graphite rod of 5 mm thickness and 8 mm diameter. During both the deposition processes, the quartz crystal thickness monitor was used for monitoring the thickness. The set-up for carbon film deposition is shown in Fig. 3.2.

Once the deposition is completed, the chamber is allowed to cool down overnight and then opened. Carbon slides were then transferred to a tubular furnace and annealed

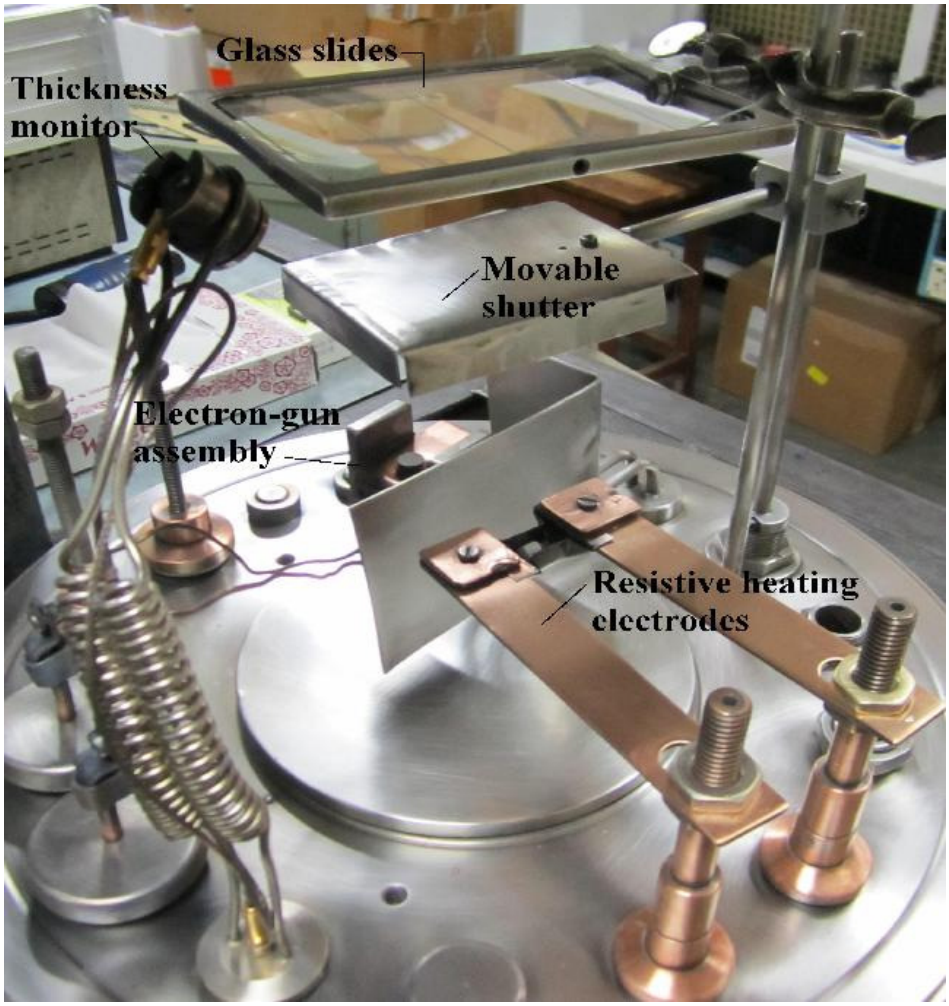

Figure 3.2: Set-up for carbon foil preparation.

at 325° C in argon atmosphere for 1 hour, to release any stress developed during the deposition. These foils were floated in warm deionized water and mounted on stainless steel target frames of 12 mm diameter. Before loading the carbon foils in the coating unit for Tl deposition, their thickness was verified by measuring energy loss of α-particles passing through them, using a ^{241}Am source. Thickness of carbon foils was found to vary between 25 to 40 μg/cm^2.

3.1.3 Preparation of isotopic thallium targets

A number of attempts were made with natural Tl material before the preparation of actual isotopic targets in order to optimize the parameters. Carbon foils were mounted at 10.3 cm above the source, with the help of stainless steel target frame holders. The chamber pressure was kept at $\sim 10^{-7}$ mbar and Tl was evaporated by resistive heating method. The material boat was heated to evaporate the material, using a low voltage

Figure 3.3: Set-up for Tl deposition on carbon foils.

high current source. A current of 140 A was applied during the evaporation and to maintain a uniform evaporation rate, the current was gradually increased from 0-140 A. The set-up for Tl evaporation on carbon films is shown in fig. 3.3.

In order to minimize the solid angle of evaporation and thus the material loss, a narrow tubular tantalum boat was used. Due to this, the quartz crystal monitor was not in the line of sight of the material boat. Therefore, we could not use the quartz crystal monitor for exact thickness monitoring during the deposition. Small changes in the monitor reading could only indicate that the material was still evaporating. Therefore, calibration of the target thickness with the amount of material loaded in the boat was required. To get the desired thickness of Tl, the quantity of natural material loaded in the boat was varied each time and the whole material was evaporated. The source to substrate distance was kept constant. After each evaporation the thickness

of Tl was measured by α-particle energy loss method, taking into account energy loss of α-particles in carbon backing. The thickness obtained in the previous measurement was used to scale the quantity of material to be loaded for next evaporation. However, the thickness could not match as per the scaling despite of keeping all other parameters constant. Tl is an oxidizing material, and it was not possible to estimate the degree of oxidation. Therefore, the method of α-particle energy loss could not give exact target thickness. The XRF technique was used to measure the thickness of natural Tl target. By scaling this result, the quantity of the isotopic Tl used in the final evaporation was determined. We consumed 41.4 mg ^{203}Tl and 38.8 mg ^{205}Tl for making a total of six isotopic targets of each kind, in one deposition. Before opening, the chamber was left overnight to cool down.

Generally in case of oxidizing targets, a capping is used for protecting it from oxidation. For this, a thin layer of carbon is deposited over the target material. For our proposed measurements, oxidation does not pose any problem. Oxygen, carbon or their fusion products with the beam are very well separated from the required heavy fusion products using the recoil ion separator like HYRA. However, one has to make sure that the chemical changes caused by the oxidation would not create a problem for target survival. We kept the natural Tl targets in air for more than a month purposefully to observe the changes in it. Due to oxidation, the colour of the targets were changed. However, it remained intact and the target material did not come out of the carbon foil. Therefore, we did not use any capping so as to avoid the energy loss and straggling of the reactions products in the same.

3.2 Characterizations of targets

The targets materials ^{203}Tl (96.54 % ^{203}Tl, 3.46 % ^{205}Tl) and ^{205}Tl (99.90 % enrichment) were procured in metal form, from ORNL, USA and ISOFLEX, USA, respectively. To find out the presence of any impurity, either in the supplied material or added inadvertently during depositions, some characterizations of the fabricated targets were carried out. For detecting low Z-materials the Rutherford back scattering (RBS) technique was used and the X-ray fluorescence (XRF) technique was employed for detecting elements with Z >13.

3.2.1 XRF Characterizations

X-ray fluorescence is the emission of characteristic secondary X-rays from a material that has been excited by bombarding with high-energy X-rays or gamma rays. The

fluorescent radiation can be analyzed by sorting the energies of the photons. Once sorted, the intensity of each characteristic radiation is directly related to the amount of each element in the material. XRF measurements of the prepared targets were carried out at the Department of Physics, Punjab University, Chandigarh.

The experimental set-up used for measurements, consisted of water cooled single window Molybdenum (Mo) anode X-ray tube (Be window of thickness 300 μm) and a 4 kW X-ray generator (PW3830, PanAnalytic, Netherland). The detection system consisted of Si(Li) detector (28.27 mm^2 $\times$ 5.5 mm, 8 μm Be window) from CANBERRA, in horizontal configuration and having a resolution of 180 eV for the Mn Kα X-rays. The targets were mounted at 45° with the detector and X-ray tube axes. Targets were bombarded with X-rays from the tube operated at 26 kV and 10 μA. Fluorescent X-ray spectra from the targets were detected in reflection mode by Si(Li) detector and collected using a PC-based multichannel analyzer (Multiport II, CANBERRA).

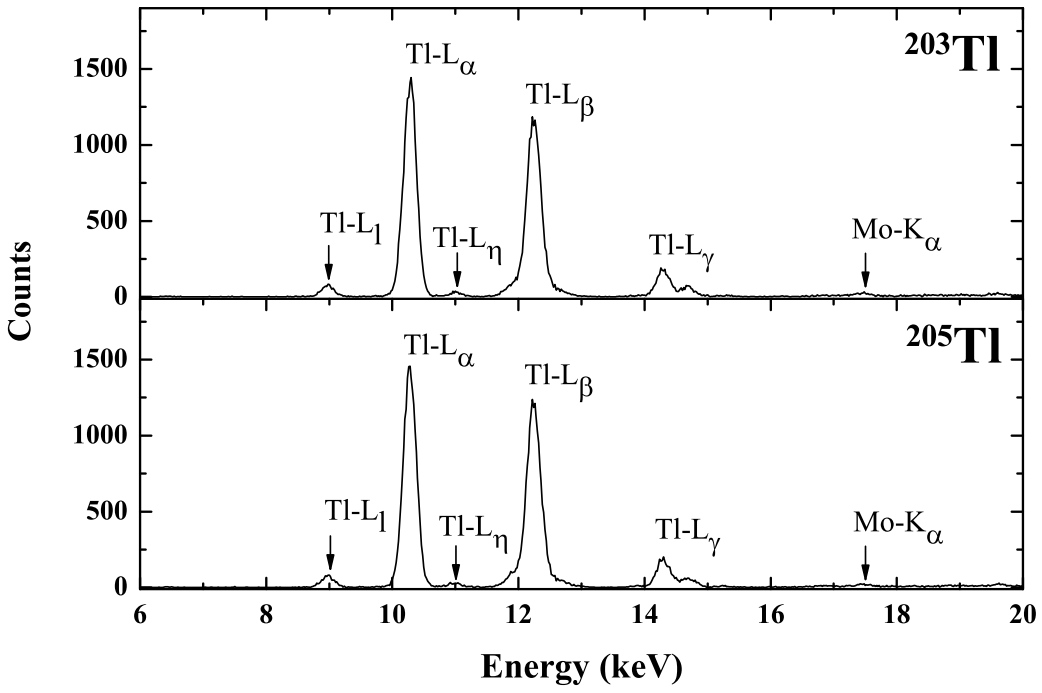

Figure 3.4: X-ray fluorescence spectra of ^{203}Tl and ^{205}Tl targets.

Fig. 3.4 shows the XRF spectra obtained from different targets, where X-rays corresponding to Tl is clearly visible, along with some trace of Mo. The latter might be due to the anode material of the X-ray tube. Table 3.1 represents the energies of the

fluorescent X-ray peaks of Tl and Mo. The isotopes of Tl can not be distinguished here as XRF is an atomic process.

Table 3.1: X-ray fluorescence peak energies for Tl and Mo.

Sr.No.	Peak	Energy (keV)
1	Tl-L_l	8.952
2	Tl-L_η	10.993
3	Tl-L_α	10.300
4	Tl-L_β	12.212
5	Tl-L_γ	14.200
6	Mo-K_α	17.400

In order to find thickness of prepared targets, XRF spectrum from 225 μg/cm^2 $TlCl_3$ standard target supplied by Micromatter, USA was collected and count rate per unit thickness of Tl was determined. While determining the count rate per unit thickness of Tl, mass fraction of Tl in $TlCl_3$ was taken into account. Thickness of the enriched target was obtained by dividing the observed count rate from enriched target with the count rate per unit thickness obtained from standard target. Taking 5 % uncertainty in thickness of standard target and considering statistical error in measurements, thickness obtained for ^{203}Tl and ^{205}Tl targets were 175 $\pm$ 9 and 156 $\pm$ 8 μg/cm^2, respectively. Though the amount of enriched material loaded for evaporation was scaled for 200 μg/cm^2 but the measured thickness was found to be less for both cases. This might be due to presence of some oxygen in the material used for deposition, which reduced the effective amount of Tl. Target thickness is determined just to make sure that the fusion products formed, after energy loss in target material, are detected with good energy and angular resolution. Target thickness does not appear explicitly in cross-section estimation.

3.2.2 RBS Characterizations

Rutherford back scattering (RBS) is an elastic collision between a high kinetic energy projectile and a stationary particle located in the target. We used 2 MeV α-particle beam from 1.7 MV tandem accelerator at IUAC, New Delhi for the RBS characterization of the fabricated targets. A PIPS detector (PD 150-16-100 AM) from CANBERRA was used to detect the back scattered α particles. This detector has an aperture solid angle of 1 msr. It was put at an angle of 170° with respect to beam. Detector calibration was done using a sample of gold deposited on glass. The beam was incident normal

to the target surface. The beam diameter was kept < 2 mm and it was ensured that the beam fell at the center of the target. To minimize the background, the beam after passing through the target and back scattered from any metal part in the chamber was not allowed to reach the detector.

The RBS spectra for both the targets are shown in Fig. 3.5 which shows that only carbon and oxygen peaks are present apart from Tl. Tl being an oxidizing element, the peak of oxygen is expected, whereas, carbon is present due to the backing. Our measurements will not be affected by the presence of the reaction products of the impurities (oxygen and carbon), as the desired reaction products are unambiguously separated from all other undesired particles by the recoil separator.

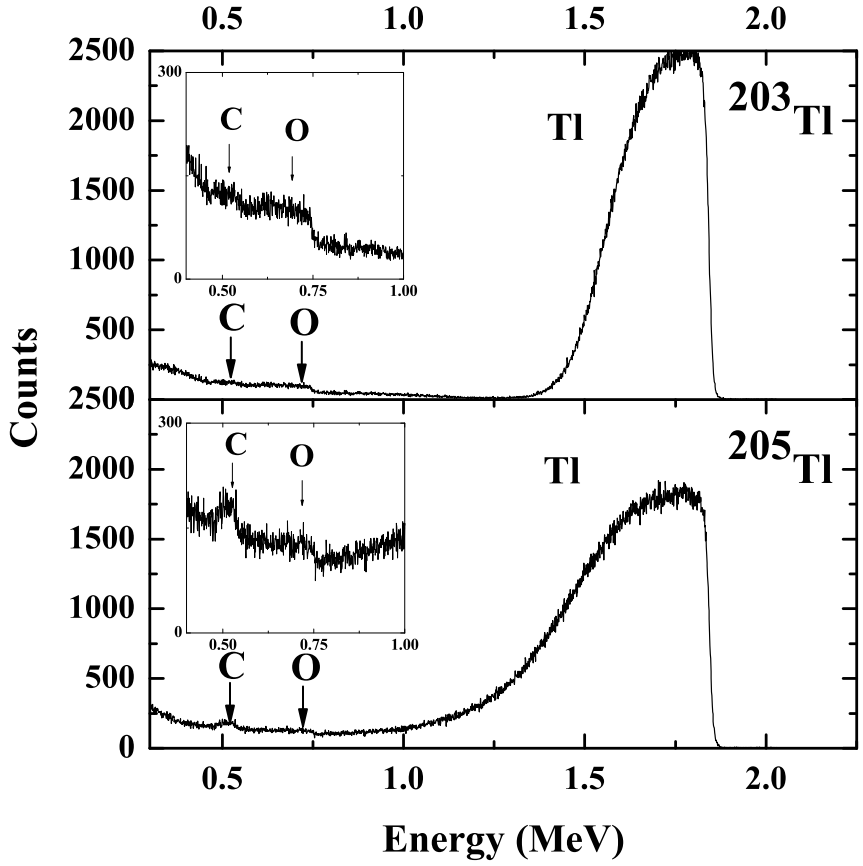

Figure 3.5: Rutherford back scattering spectra of ^{203}Tl and ^{205}Tl targets, using 2 MeV He^{+} ions detected at 170° with respect to beam. Carbon and oxygen peaks are shown in insets.

The RBS peaks and hence the elements, are identified using the scattered energy values from the target. Kinematic factor K is defined as the ratio of scattered projectile energy to incident projectile energy is given by the relation

$$K = \frac{E_1}{E_0} = \left[\frac{M_1 \cos\theta \pm \sqrt{{M_2}^2 - {M_1}^2 (\sin\theta)^2}}{M_1 + M_2} \right]^2 \tag{3.1}$$

where E_0 is the incident projectile energy and E_1 is the scattered projectile energy. M_1 and M_2 are projectile and target masses respectively and θ is the scattering angle of the projectile in lab frame. To identify the peaks and hence the elements, these scattered energy values are used.

Table 3.2 represents the kinematic factor K and corresponding scattered energies from different elements, for 2 MeV He^+ projectile scattered at 170°.

Table 3.2: Kinematic factor and Rutherford back scattered energies for 2 MeV He^+ ions scattered from different elements, at 170° with respect to beam.

Sr.No.	Element	K	Energy (MeV)
1	Tl	0.9252	1.8504
2	O	0.3625	0.7250
3	C	0.2536	0.5072

3.3 Fabrication of Ni pressure window foils for HYRA

In gas-filled recoil separators, we need to separate the gas-filled magnetic region from beam line vacuum. One can use a thin foil or differential pumping. The simplest is to use a thin foil. This foil can ideally be of any material, but should possess certain characteristics like strength to hold the pressure difference, ability to dissipate the heat produced due to bombardment of beam, low Z and minimum thickness in order to minimize the beam energy loss in it. Using thin carbon or nickel (Ni) foil for this purpose is a convention. In HYbrid Recoil mass Analyzer (HYRA) at IUAC, we have been successfully using Ni foils of thickness $\sim$ 1 - 1.5 mg/cm^2. These foils could survive several days with few pnA beam current. Fig. 3.6 shows a schematic diagram of the pressure window foil mounting position and its usage.

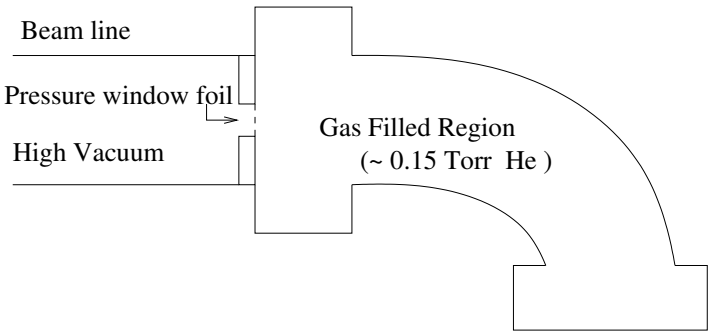

Figure 3.6: Schematic diagram to show the pressure window foil position and its usage.

3.3.1 Rolling of Ni foils

It was tried to roll the Ni foils down to a thickness below 1 mg/cm^2. The process of fabrication of thin Ni foils by rolling and the difficulties encountered are presented. Ni is hard and ductile, therefore it can be rolled but with greater effort.

Ni foils to be rolled were placed between highly polished mirror finished folded stainless steel plates and rolled by means of a set of the shaped rollers in a conventional mill. Ni foils were rolled from $\sim$ 22 mg/cm^2 to below 1 mg/cm^2, the thinnest being $\sim$ 450 μg/cm^2. With decreasing thickness pin holes started appearing in the foil, and a tendency to stick with the steel plate was developed in the foil. In order to reduce the chances for pin holes some precautions were taken. Stainless steel plates were cleaned thoroughly with alcohol, to reduce the stickiness and to keep them free from dust. This reduced the chances for pin holes. The pressure on the rollers was increased in small steps, so that foil doesn't stick to the plates, and a uniform thickness foil could be rolled. Whenever a foil stuck to the plates, it was first allowed to release the developed stress and then removed from plates carefully using alcohol or acetone, if required. Towards the lower thickness, whenever there was a tearing at the borders, they were trimmed immediately in order to stop the cracks from propagating further. Therefore the effective area of foil went on decreasing as we go towards lower thickness. Plates and foil were dipped in acetone to remove any dust particle in between the rolling. Below 1 mg/cm^2, most of the time the stainless steel plate had to be dipped in acetone or alcohol in order to float the rolled foil. Though all these precautions increased the survival chances of the foil considerably, still rolling a foil of desired thickness is an art which takes time and patience. Fig. 3.7 shows the photograph of one such rolled Ni foil. Thickness of these rolled foils were in the range $\sim$ 450 μg/cm^2 to 1 mg/cm^2.

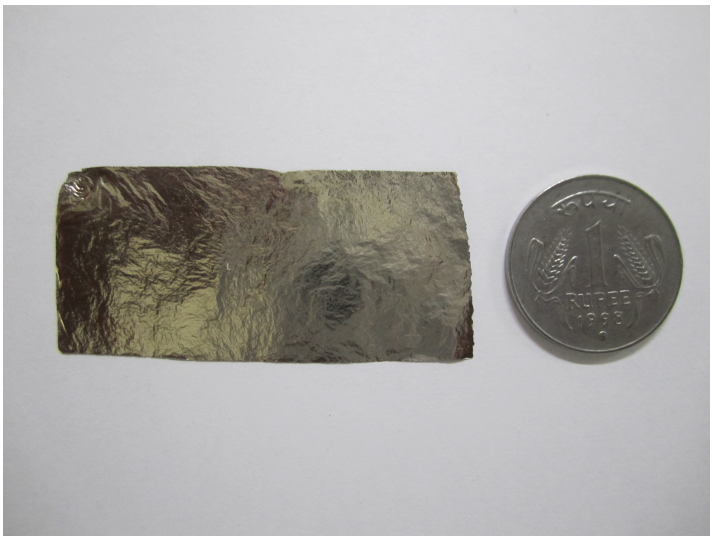

Figure 3.7: Rolled Ni foil of area 5.6 × 2.5 cm^2 and thickness ∼ 680 $\mu g/cm^2$.

3.3.2 Pressure testing of rolled foils

The thinnest foil of thickness ∼ 450 $\mu g/cm^2$ was pasted on an annular flange of 15 mm inner diameter and tested for pressure handling capability. Helium gas pressure on one side of the foil was maintained at 1.3 mbar and other side pressure was 1.7 × 10^{-5} mbar. Though by careful rolling, the number of pin holes could be reduced, it was not possible to make such a thin foil free from pin holes. As long as, the gas leakage through the pin holes is not as high that it is not able to maintain the desired pressure difference across the foil, it is acceptable. In an actual experiment we use the helium gas at a pressure lower than 1 mbar (0.15 Torr).

Bibliography

[1] H. L. Adair, Nucl. Instr. and Meth. **B40/41**, 1132 (1989).

[2] N. Madhavan *et al.*, Pramana - J. Phys. **75**, 317 (2010).

[3] J. Bristow, Proc. Phys. Soc. **51**, 349 (1939).

[4] R. D. Griffioen and R. D. Macfarlane, Phys. Rev. **133**, B1373 (1964).

[5] G. Ben-David, B. Arad, J. Balderman, and Y. Schlesinger, Phys. Rev. **146**, 852 (1966).

[6] R. Moreh and A. Wolf, Phys. Rev. **182**, 1236 (1969).

[7] R. Moreh, A. Nof, and A. Wolf, Phys. Rev. C **2**, 249 (1970).

[8] Y. L. Beyec, M. Lefort, and M. Sarda, Nucl. Phys. A **192**, 405 (1972).

[9] D. Aumann and G. Mullen, Nucl. Instr. and Meth. **115**, 75 (1974).

[10] H. L. Adair, Proc. of fourth INTDS, Rep ANL/PHY/MSD **76**, 1 (1976).

[11] V. Pankajakshan, K. Neelakandan, and C. Menon, Thin Solid Films **168**, 165 (1989).

[12] M. Lagunas-Solar, J. Jungermann, N. Peek, and R. Theus, International Journal of Applied Radiation and Isotopes **29**, 159 (1978).

[13] S.M.Qaim, R. Weinreich, and H. Ollig, International Journal of Applied Radiation and Isotopes **30**, 85 (1979).

[14] J. Gallant, D. Yaraskavitch, and N. Bray, Nucl. Instr. and Meth. **167**, 55 (1979).

[15] M. C. Lagunas-Solar, J. A. Jungerman, and D. W. Paulson, International Journal of Applied Radiation and Isotopes **31**, 117 (1980).

[16] A. Byrne, G. Dracoulis, K. Schiffer, P. Davidson, T. Kibedi, B. Fabricius, A. Baxter, and A. E. Stuchbery, Phy. Rev. C **42**, 42 (1990).

[17] P. Walker, D. Hinde, A. Byrne, G.D.Dracoulis, and W. Gelletly, Z. Phys. A **359**, 225 (1997).

[18] I. Ryzhov, G.A.Tutin, A. Mitryukhin, V. Oplavin, S. Soloviev, J.Blomgren, P. Renberg, J. Meulders, Y. E. Masri, T. Keutgen, R. Prieels, and R. Nolte, Nucl. Instr. and Meth. A **562**, 439 (2006).

[19] R. M. Lambrecht, M. Sajjad, R. H. Syed, and W. Meyer, Nucl. Instr. and Meth. A **282**, 296 (1989).

[20] J. Gehlot, S. R. Abhilash, S. Ojha, D. Mehta, D. Kabiraj, and A. M. Vinodkumar, Proceedings of the DAE Symp. on Nucl. Phys. **57**, 896 (2012).

[21] J. Gehlot, S. R. Abhilash, S. Ojha, D. Mehta, D. Kabiraj, and A. M. Vinodkumar, J. Radioanal. Nucl. Chem. **305**, 755 (2015).

Chapter 4

Data Analysis and Results

Evaporation residue cross-sections for the ^{16}O + ^{203,205}Tl reactions were measured at laboratory beam energies in the range of 82 - 113 MeV using a gas-filled separator. Transmission efficiency of the separator was estimated using a calibration reaction ^{16}O + ^{197}Au and by simulating the ER angular distributions. Statistical model calculations were performed for both the measured systems. These calculations over estimate the experimental evaporation residue cross-sections. This could be attributed to the presence of non compound nuclear fission. An estimation of non compound nuclear fission contribution was carried out. A comparison of the measured reactions with the neighbouring systems shows that a slight change in the entrance channel or the compound nucleus properties makes a large difference in evaporation residue cross sections.

4.1 Data analysis

4.1.1 ER cross-section

The first step towards experimental determination of ER cross-section is to identify the ERs unambiguously at the focal plane of the separator. This is achieved by creating a two dimensional spectrum of energy loss (ΔE) vs time of flight (TOF) (Fig. 2.24). The number of ER events selected from this spectrum has been used to obtain the ER cross section using the equation

$$\sigma_{\mathrm{ER}} = \frac{Y_{\mathrm{ER}}}{Y_{\mathrm{mon}}} \left(\frac{d\sigma}{d\Omega}\right)_{\mathrm{Ruth}} \Omega_{\mathrm{mon}} \frac{1}{\varepsilon_{HYRA}} \tag{4.1}$$

where σ_{ER} is the ER cross-section (in mb), $\mathrm{Y_{ER}}$ is ER yield at the focal plane of HYRA,

Y_{mon} is the average yield in monitor detectors, ε_{HYRA} is the transmission efficiency of the separator and Ω_{mon} is the solid angle (in sr) subtended by each monitor detector. $\left(\frac{d\sigma}{d\Omega}\right)_{\text{Ruth}}$ is the differential Rutherford scattering cross-section (in mb/sr) in the laboratory system at chosen scattering angle and energy. $\left(\frac{d\sigma}{d\Omega}\right)_{\text{Ruth}}$ is given by the formula

$$\left(\frac{d\sigma}{d\Omega}\right)_{Ruth} = 1.296\left(\frac{Z_P Z_T}{E_{lab}}\right)^2\left[\frac{1}{sin^4\left(\frac{\theta}{2}\right)} - 2\left(\frac{M_P}{M_T}\right)^2 + ...\right] \tag{4.2}$$

where Z_P and Z_T are the atomic numbers of the projectile and the target, respectively and θ is the monitor detector angle with respect to beam direction. M_P and M_T are the masses of the projectile and the target, respectively.

4.1.2 Transmission efficiency

In Eqn. (4.1), apart from the experimental observables, transmission efficiency (ε_{HYRA}) of the separator is an important factor, which needs to be known precisely in order to extract absolute ER cross-sections. Only a fraction of ERs, produced in a fusion reaction, reaches the focal plane and is recorded by the detector. Transmission efficiency of the separator is the ratio of the ERs detected at the focal plane of the separator to the total number of ERs produced at target site. It depends on several factors such as entrance channel mass asymmetry, beam energy, geometrical acceptance of the separator, target thickness (due to multiple scattering), helium gas pressure in the separator, focal plane detector size, and presence of some short-lived isomers [1]. Isomers with a half-life less than ER time of flight may result in Auger processes and thereby change the ER charge state in flight and may deviate its path drastically, and hence, affect the transmission (for vacuum mode separators). For gas-filled separators the dilute gas (He in this case), is expected to reset the charge state along the trajectory. Moreover, in gas-filled separators, the ERs with different charge states tend towards a mean charge state through multiple collisions in the dilute gas medium and on an average follow a mean trajectory. Hence, the presence of short-lived isomers is not expected to affect the transmission drastically for gas-filled separators.

The transmission efficiency is generally measured during the experiment, using a gamma detector at target site, via characteristic gamma detection in both coincidence and singles mode [2]. Such measurements involve coincidence studies between characteristic gamma rays at target site and ERs at focal plane. These measurements require longer beam time. In addition to this, we should keep in mind that the background at target site will also be a serious problem in accurate estimation of transmission

efficiency. Therefore, at times, it may be necessary to simulate the transmission efficiency or scaling it from a nearby similar reaction. In the present investigation, we have adopted the method of scaling using a nearby system. A calibration reaction forming ^{213}Fr through ^{16}O + ^{197}Au was used to experimentally estimate the transmission efficiency. For this, we have used the ER cross-section data from Brinkmann *et al.* [3] and calculated ε_{HYRA} using the relation

$$\varepsilon_{HYRA} = \frac{Y_{\rm ER}}{Y_{\rm mon}} \left(\frac{d\sigma}{d\Omega}\right)_{\rm Ruth} \Omega_{\rm mon} \frac{1}{\sigma_{ER}} \tag{4.3}$$

Substituting the ER counts (from ΔE vs TOF spectrum) and other quantities, the ε_{HYRA} value for ^{16}O+^{197}Au reaction was experimentally estimated. Here σ_{ER} is the ER cross section as obtained in the earlier work [3]. The estimated transmission efficiencies for ^{16}O + ^{197}Au are given in Table 4.1.

Table 4.1: HYRA transmission efficiency ($\varepsilon_{\rm HYRA}$) for the calibration reaction ^{16}O + ^{197}Au at different beam energies using ER data from Brinkmann *et al.* [3]

Reaction	$E_{\rm lab}$(MeV)	$\sigma_{\rm ER}$ (mb)	$\varepsilon_{\rm HYRA}$ (%)
^{16}O + ^{197}Au	93.4	168.3 ± 16.8	0.13 ± 0.03
	99.5	131.1 ± 13.1	0.15 ± 0.03
	105.6	98.9 ± 9.9	0.16 ± 0.03
	113.8	67.8 ± 6.8	0.16 ± 0.03

For scaling the efficiency to our measured reactions, we simulated ER angular distributions for the calibration reaction ^{16}O + ^{197}Au and for presently measured reactions *viz* ^{16}O + ^{203,205}Tl using the code PACE4 [4, 5]. Transmission efficiencies for the present systems were then scaled from the calibration reaction by comparing the fraction of their respective angular distributions passing through the geometrical acceptance of HYRA, i.e. 9.5°, in a way similar to our previous measurements [6–12]. Fig. 4.1 shows the angular distributions of ERs at different beam energies for the measured reactions *viz* ^{16}O + ^{203,205}Tl along with those for the calibration reaction, i.e. ^{16}O + ^{197}Au.

The variation of angular distributions are in accordance with the kinematics. With increasing energy, the angular distribution should be forward focused. The calibration

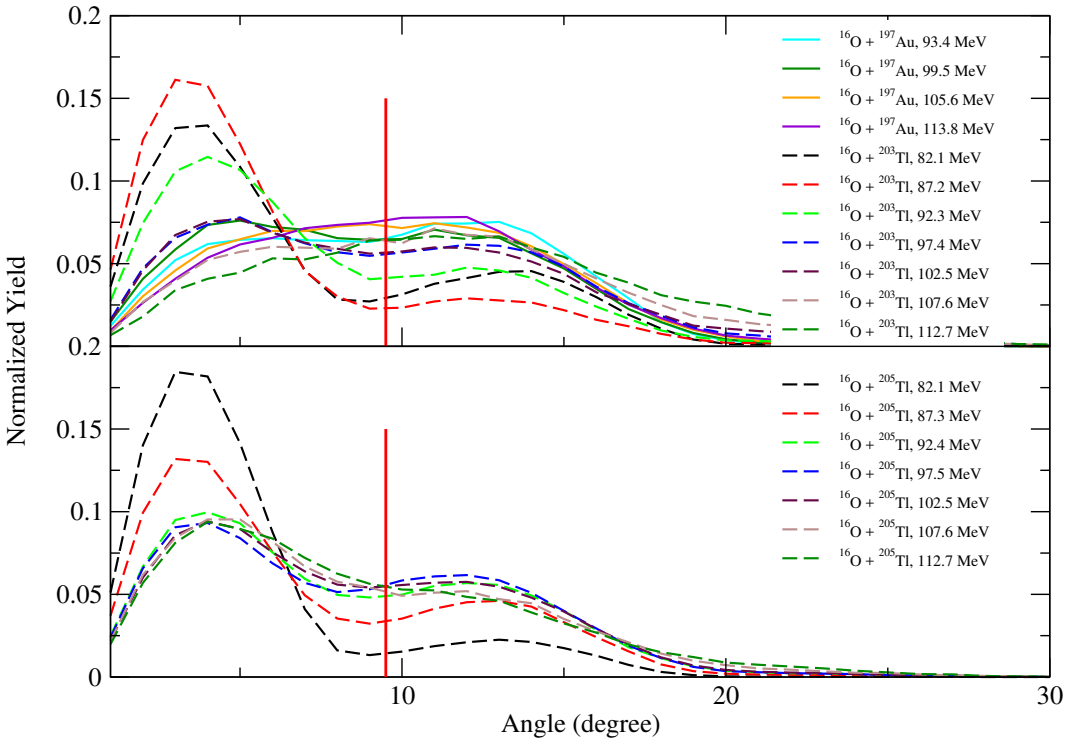

Figure 4.1: Angular distributions of ERs at different beam energies simulated using PACE4 [4, 5]. The vertical line at 9.5° denotes the HYRA angular acceptance.

reaction ^{16}O + ^{197}Au has more fraction of alpha-evaporation channels than non-alpha-evaporation channels, hence having broader distribution. At higher energies, ^{16}O + ^{203,205}Tl systems also have more alpha-evaporation channels and the shape of ER angular distribution is quite similar to that for ^{16}O + ^{197}Au reaction. Transmission efficiencies thus obtained for the reactions ^{16}O + ^{203}Tl and ^{16}O + ^{205}Tl are listed in Table 4.2.

4.1.3 Alpha decay effects on ER transmission efficiency

If the half-life of the α-decaying ER is less than its TOF, it may decay inside the separator and the push given by the emitted alpha particle may deflect the heavy recoil from its path and thus reduce its transmission through the separator. The α-decaying ERs produced in these reactions are mostly actinium, radium and francium isotopes. Statistical model code HIVAP [13, 14] was used to check the major decay channels and their relative population in the studied reactions in the measured energy range. Fig. 4.2 shows the individual ER yields for ^{16}O + ^{203}Tl and ^{16}O + ^{205}Tl reactions using HIVAP [13, 14] at different beam energies. ER channels with relative yield of more than 1% of the total ER were considered.

Table 4.2: HYRA transmission efficiency $\varepsilon_{\mathrm{HYRA}}$ for ^{16}O + ^{203}Tl and ^{16}O + ^{205}Tl reactions scaled from calibration reaction ^{16}O + ^{197}Au at different energies.

Reaction	E_{lab}(MeV)	$E_{c.m.}$(MeV)	E^*(MeV)	$\varepsilon_{\mathrm{HYRA}}$ (%)
^{16}O + ^{203}Tl	82.1	76.1	34.0	0.18 ± 0.04
	87.2	80.9	38.8	0.21 ± 0.04
	92.3	85.6	43.5	0.18 ± 0.04
	97.4	90.3	48.3	0.14 ± 0.03
	102.5	95.0	53.0	0.16 ± 0.03
	107.6	99.7	57.7	0.14 ± 0.03
	112.7	104.4	62.4	0.13 ± 0.03
^{16}O + ^{205}Tl	82.1	76.2	33.1	0.23 ± 0.03
	87.3	80.9	37.9	0.19 ± 0.04
	92.4	85.7	42.6	0.17 ± 0.03
	97.5	90.4	47.3	0.16 ± 0.03
	102.5	95.1	52.0	0.18 ± 0.04
	107.6	99.8	56.8	0.20 ± 0.04
	112.7	104.5	61.5	0.20 ± 0.04

The decay properties of these ERs are summarized in Table 4.3. For the ^{16}O + ^{203}Tl case, most of the ERs, as predicted by HIVAP, have sufficiently long half-lives to reach focal plane with hardly any loss due to decay. However, for the reaction ^{16}O + ^{205}Tl, the major exit channels at lower energies are 3n, 4n or α2n, producing significant number of the short lived ERs ^{218}Ac, ^{217}Ac and ^{215}Fr, respectively. Their half-lives are 1.08 μs, 69 ns and 86 ns, respectively [15], which are much less than the average TOF through the gas-filled separator HYRA, which is in the range 3.2 - 3.8 μs. These nuclei decay during the flight as per the radioactive decay law. As a result, they are not transmitted fully through the separator.

Let us consider the simplest case of an ER travelling along the central trajectory. If it under goes α-decay, the outgoing α-particle will impart a recoil kick to the residual ER. If the α-particle is emitted at an angle θ with respect to the initial direction of motion, and residual ER is deflected at an angle ϕ with respect to the initial direction, as shown in the Fig 4.3.

According to the law of conservation of momentum, equating the vertical compo-

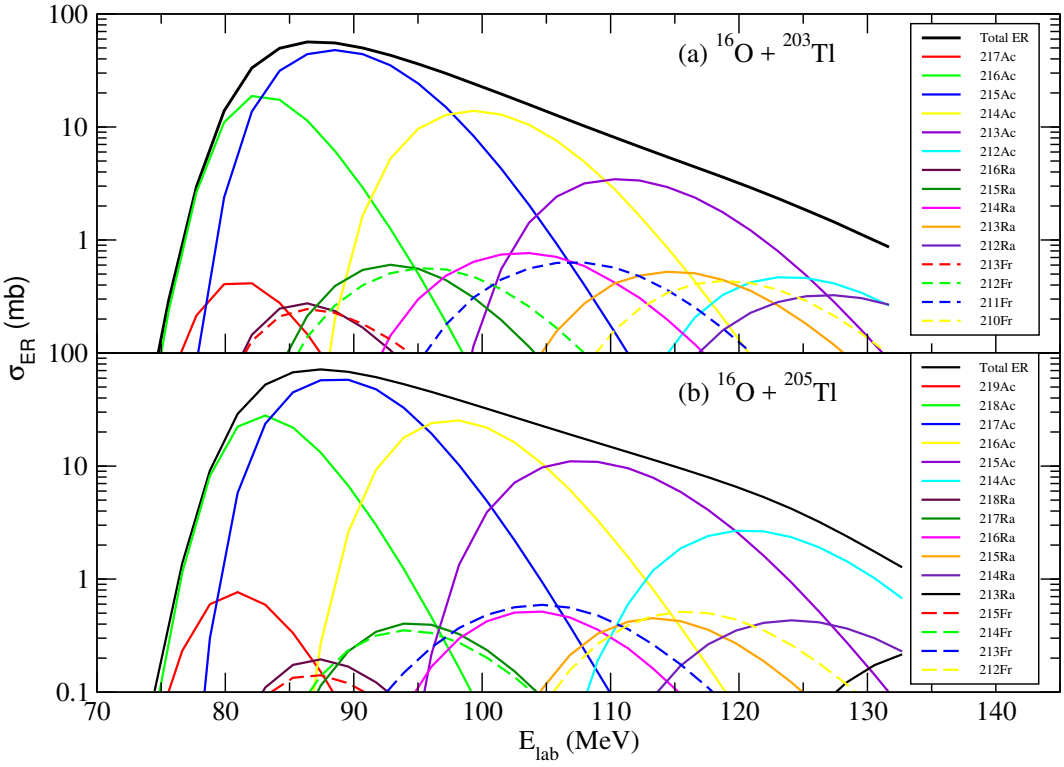

Figure 4.2: Yield of individual exit channels for (a) ^{16}O + ^{203}Tl and (b) ^{16}O + ^{205}Tl reactions at different beam energies using HIVAP [13, 14].

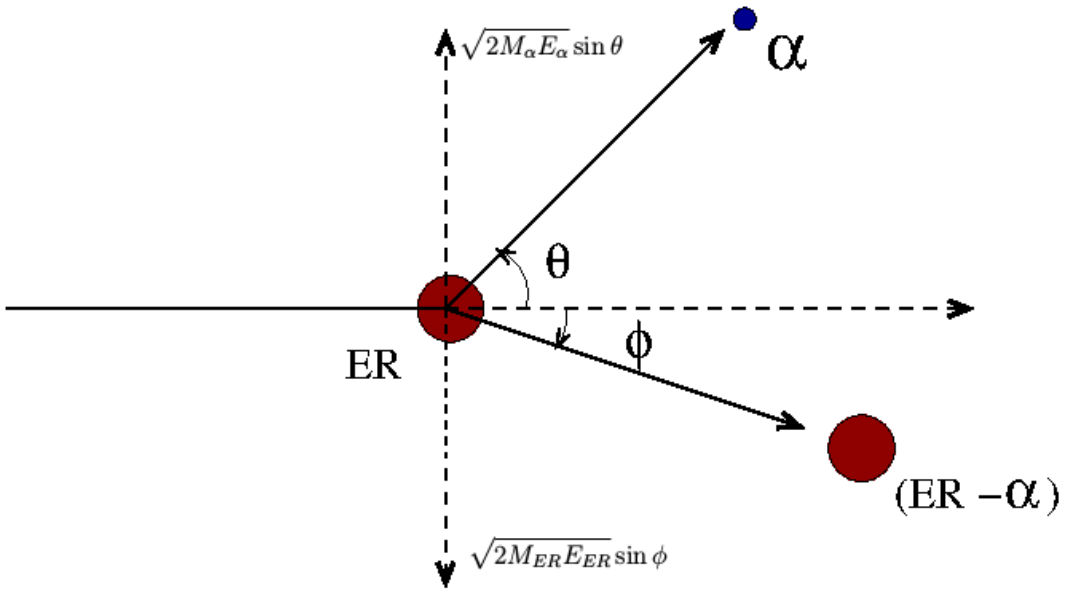

Figure 4.3: Schematic diagram of an ER under going α-decay.

nents of the individual momenta

$$\sqrt{2 \times M_\alpha \times E_\alpha} \times \sin\theta = \sqrt{2 \times M_{ER} \times E_{ER}} \times \sin\phi \tag{4.4}$$

Table 4.3: Decay properties of the ERs produced in ^{16}O + ^{203}Tl and ^{16}O + ^{205}Tl reactions [15].

ER	Half-life ($t_{\frac{1}{2}}$)	Decay mode	α-energy (MeV)	Intensity (%)
^{219}Ac	11.8 μs	α	8.664	100%
^{218}Ac	1.08 μs	α	9.205	100%
^{217}Ac	69 ns	α	9.650	100%
^{216}Ac	440 μs	α	8.992	10%
	440 μs	α	9.064	90%
^{215}Ac	0.17 s	α	7.600	99.48%
^{214}Ac	8.2 s	α	6.978	1.0%
	8.2 s	α	7.081	37.4%
	8.2 s	α	7.215	48.1%
^{213}Ac	738 ms	α	7.360	100%
^{212}Ac	0.93 s	α	7.379	$\approx$57%
^{218}Ra	25.2 μs	α		100%
^{217}Ra	1.6 μs	α	8.992	100%
^{216}Ra	182 ns	α		100%
^{215}Ra	1.66 ms	α	7.882	2.8%
	1.66 ms	α	8.171	1.3%
	1.66 ms	α	8.700	95.9%
^{214}Ra	2.46 s	α	7.137	99.78%
^{213}Ra	2.73 ms	α	6.521	4.6%
	2.73 ms	α	6.624	39%
	2.73 ms	α	6.732	36%
^{212}Ra	13.0 s	α	6.899	$\approx$85%
^{215}Fr	86 ns	α	9.360	100%
^{214}Fr	5.0 ms	α	7.605	1%
	5.0 ms	α	7.937	1%
	5.0 ms	α	8.358	4.8%
	5.0 ms	α	8.427	93.0%
^{213}Fr	34.6 s	α	6.775	99.23%
^{212}Fr	20.0 m	α	6.262	16.3%
	20.0 m	α	6.335	4.4%
	20.0 m	α	6.342	1.32%
	20.0 m	α	6.383	10.3%
	20.0 m	α	6.406	9.4%
^{211}Fr	3.1 m	α	6.537	87%
^{210}Fr	3.18 m	α	6.545	71%

where M_α, M_{ER}, E_α, E_{ER} are the masses and kinetic energies of the emitted α-particle and the recoiling residual ER, respectively. Initial kinetic energy of the ERs at the exit of the target foil, for these reactions in the measured energy range, is estimated to be $\sim$ 5.3 to 7.4 MeV and they are further slowed down by losing their energy in the He gas. Table 4.3 shows that the decay α energy, for short lived ERs, ranges from $\sim$ 9.0 to 9.65 MeV. We take the example of ^{218}Ac, which under goes α-decay and leaves residual ER ^{214}Fr. The decay α energy for ^{218}Ac is $\sim$ 9.2 MeV and the average ER kinetic energy for ^{218}Ac $\sim$ 5.3 MeV just after the target. Then according to Eqn. 4.4,

$$\sqrt{2 \times 4 \times 9.2} \times \sin\theta = \sqrt{2 \times 214 \times 5.3} \times \sin\phi \tag{4.5}$$

$$\phi = \sin^{-1}(0.180 \times \sin\theta) \tag{4.6}$$

If α-particle is emitted in a direction perpendicular to the direction of motion, i.e. if $\theta = 90°$, $\phi \sim 10.4°$, with $\theta = 45°$, $\phi \sim 7.3°$, and with $\theta = 0°$, $\phi = 0°$.

Thus the α-particles emitted at 90°to the direction of motion, give maximum deflection to the ERs while the α-particles emitted in extreme forward or backward direction will not deflect the ERs from their path. The deflected ER will experience an increasing spatial deviation from the trajectory, while moving down the travel path. It will eventually escape the focal plane detector, if the spatial deviation produced is more than half of the detector dimension (see Fig. 4.4). This travel path, required to miss the detector, is obviously longer for smaller angular deflections, and shorter for larger deflections.

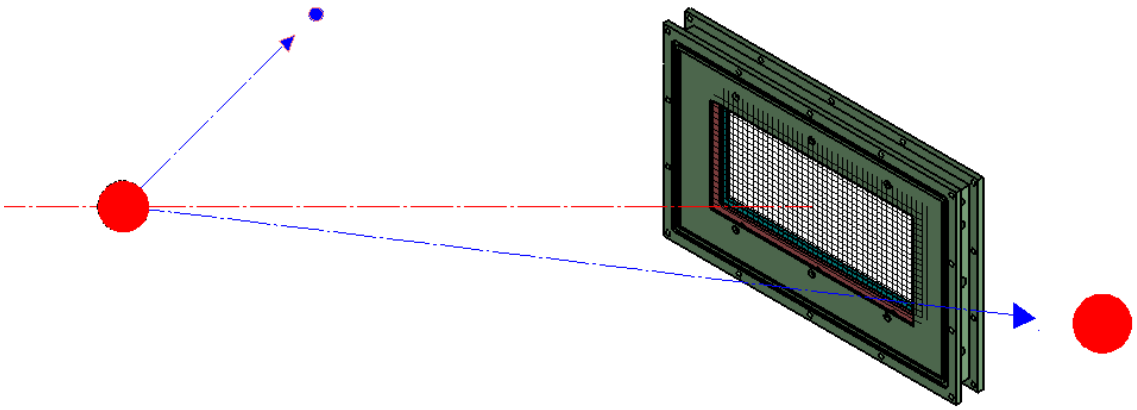

Figure 4.4: Alpha-decaying ER escaping the detector after α-decay.

Considering the dimensions of the MWPC used in these measurements (detector dimensions are 15×5 cm^2 with actual active area limited to 11×5 cm^2 due to the size of the foil supporting flange), we find that, even for an angular deflection as small as 1° (corresponding to an α emitted at $\sim 5.6°$), this travel path is ~ 3.15 m for X dimension and even less i.e. ~ 1.43 m for Y dimension. Here we see that the maximum angular deflection produced goes up to $\sim 10.4°$, which requires only $1/10^{th}$ of this travel path to go out of the detector dimension. That means even if the ER undergoes α-decay at a distance less than half a meter, prior to the focal plane, it is supposed to be missed. Here most of the ERs having half lives less than their TOF, decay in the early stage of ~ 8 meter long flight path of the separator.

Hence, for an ER traveling along the central trajectory, the push given by emitted α, with an energy for the present case (~ 9 MeV), is sufficient to deflect the ER away from the view of the focal plane detector. Only the ERs decaying at very end of the flight path manage to be detected in the focal plane detector. Therefore, as an extreme approximation, it is assumed that any ER decaying in-flight will not reach the focal plane detector. The transmission loss due to in-flight decay of short-lived ERs is compensated considering their relative populations, respective half-lives and the TOFs through the separator. In other words the reduction in transmission efficiency due to the in-flight α-decay is accounted properly.

The number of ERs reaching at focal plane is given by

$$N(t) = N(0)\exp(-\lambda t) \tag{4.7}$$

where $N(0)$ is the initial number of an individual exit channel ERs entering the geometrical acceptance of the separator, $N(t)$ is the number of ERs reaching focal plane, surviving the in-flight decay, after time t which is the TOF of the ER through HYRA. λ is the decay constant which is calculated using half-life of the ER. This gives the fraction of the individual exit channel ERs surviving the α-decay and reaching the focal plane (or getting lost due to decay). Then the fraction of total ERs getting transmitted to focal plane is estimated, considering transmissions of individual exit channel ERs and their relative populations, as percentage of total ERs produced. This gives another factor of efficiency which need to be multiplied with the geometrical efficiency listed in Table 4.2 to have absolute efficiency. Table 4.4 summarizes the transmission fraction of the total ERs entering the separator, which survive the in-flight decay and reach the focal plane.

To summarize, the first order approximations taken for estimating the transmission efficiency of the separator are

Table 4.4: Fraction of ERs reaching focal plane, surviving the in-flight alpha-decay $\eta_{\alpha\text{-decay}}$ at different energies.

Reaction	E_{lab}(MeV)	$E_{c.m.}$(MeV)	E^*(MeV)	$\eta_{\alpha\text{-decay}}$ (%)
$^{16}O + {}^{203}Tl$	82.1	76.1	34.0	97.9
	87.2	80.9	38.8	99.2
	92.3	85.6	43.5	99.8
	97.4	90.3	48.3	100
	102.5	95.0	53.0	100
	107.6	99.7	57.7	100
	112.7	104.4	62.4	100
$^{16}O + {}^{205}Tl$	82.1	76.2	33.1	10.9
	87.3	80.9	37.9	4.5
	92.4	85.7	42.6	22.4
	97.5	90.4	47.3	66.9
	102.5	95.1	52.0	89.4
	107.6	99.8	56.8	95.9
	112.7	104.5	61.5	98.3

(i) All the ERs entering to HYRA angular aperture are supposed to reach to the focal plane or more precisely they are transported with an efficiency similar to the nearby calibration system.

(ii) ERs decaying in-flight are not reaching the focal plane detector.

(iii) The internal conversion processes due to isomer decay are compensated or reset by collisions in dilute He gas.

Though the work done is fairly logical and requires an intense effort to deal with individual exit channels at every energy. However, a detailed Monte Carlo simulation for estimating the transmission efficiency would be ideal.

The ER cross-sections thus obtained from the experiment are summarized in Table 4.5. The overall errors in the obtained cross sections are less than 20%

Table 4.5: ER cross-section σ_{ER} for ^{16}O + ^{203}Tl and ^{16}O + ^{205}Tl reactions at different energies.

Reaction	E_{lab}(MeV)	$E_{c.m.}$(MeV)	E^*(MeV)	σ_{ER} (mb)
^{16}O + ^{203}Tl	82.1	76.1	34.0	7.8 ± 1.6
	87.2	80.9	38.8	13.1 ± 2.6
	92.3	85.6	43.5	16.8 ± 3.4
	97.4	90.3	48.3	26.4 ± 5.3
	102.5	95.0	53.0	16.4 ± 3.3
	107.6	99.7	57.7	11.8 ± 2.4
	112.7	104.4	62.4	8.5 ± 1.7
^{16}O + ^{205}Tl	82.1	76.2	33.1	54.6 ± 10.9
	87.3	80.9	37.9	67.9 ± 13.6
	92.4	85.7	42.6	53.9 ± 10.8
	97.5	90.4	47.3	32.8 ± 6.6
	102.5	95.1	52.0	23.7 ± 4.7
	107.6	99.8	56.8	20.4 ± 4.1
	112.7	104.5	61.5	14.8 ± 3.0

4.2 Statistical model calculations

Experimental ER cross sections were analyzed using HIVAP code [13, 14] which incorporates a potential-barrier passing model with standard statistical model (SSM). We have used the standard parameter set suggested by Reisdorf-Schadel [14]. Table 4.6 gives a list of the standard parameter set suggested by Reisdorf-Schadel. ER cross sections calculated for strongly fissile CN at energies well above the fusion barrier [16], are relatively insensitive to the form of the nuclear potential [17, 18] and are mainly determined by SSM parameters which describe the de-excitation of CN. The macroscopic parameters of the nuclear level densities in fission and evaporation channels are provided by ratios of level densities, $\widetilde{a}_f/\widetilde{a}_n \geq 1$, due to different shapes at the saddle and equilibrium states [13, 14]. $\widetilde{a}_f$ is the level density parameter at fission saddle point and $\widetilde{a}_n$ is after neutron evaporation. A damping constant of 18.5 MeV [13, 14, 19] was used to take care of ground state shell effects which have been neglected at the saddle point. Empirical masses [20] were used to calculate ground state shell corrections, excitation, and separation energies. As shown by Sagaidak *et al.* [21], calculations performed in this work, at above fusion barrier energies, depend only on one adjustable

scaling parameter k_f of the Lquid drop (LD) fission barrier. i.e., the fission barrier is given by

$$B_f(\ell) = k_f B_f^{LD}(\ell) - \delta W_{g.s.} \tag{4.8}$$

where $B_f^{LD}(\ell)$ is the rotating liquid drop fission barrier and $\delta W_{g.s.}$ is the difference between the empirical and liquid drop masses.

Table 4.6: Reisdorf and Schdel Parameter set for the HIVAP code [13, 14].

Variable	Description	Value
LEVELPAR	Scale parameter for the level density	1.153
AF/AN	Level density ratio parameter value	1
BARFAC	Scale parameter for the fission barrier	1
EDAMP	Shell effect damping energy (MeV)	18.0
DELT	Nuclear pairing correction energy (MeV)	11.0
V0	Initial value of the nuclear potential (MeV)	70.0
R0	Nuclear radius parameter (fm)	1.12
D	Fuzziness in the nuclear radius parameter (fm)	0.75
Q2	Nuclear quadrupole moment (fm^2)	1050
CRED	Scale parameter for the interaction barrier	1.0
SIGR0	Fluctuation of the interaction barrier (% of R0)	3.0
CUTOFF	Integration limits in (SIGR0) for barrier fluctuations	5.0
XTH	Extra push theory threshold fissility parameter	0.7
APUSH	Slope coefficient from extra push theory	18.0
FPUSH	Angular momentum coefficient from extra push theory	0.75

4.3 Results and Discussion

In Fig. 4.5 and Fig. 4.6, we plot ER excitation functions for ^{16}O + ^{205}Tl and ^{16}O + ^{203}Tl respectively. Statistical model calculations, using HIVAP [13, 14] ($k_f = 1$), over predict the experimental ER cross-sections, which might be due to the presence of non compound nuclear fission (NCNF) in these reactions. A reduced fission barrier ($k_f < 1$) may be required to reproduce the experimental ER cross-sections. However, this

alone doesn't confirm the presence of NCNF. The reduced fission barrier is rather a measure of the product $P_{CN} \times P_{surv}$ being less than unity.

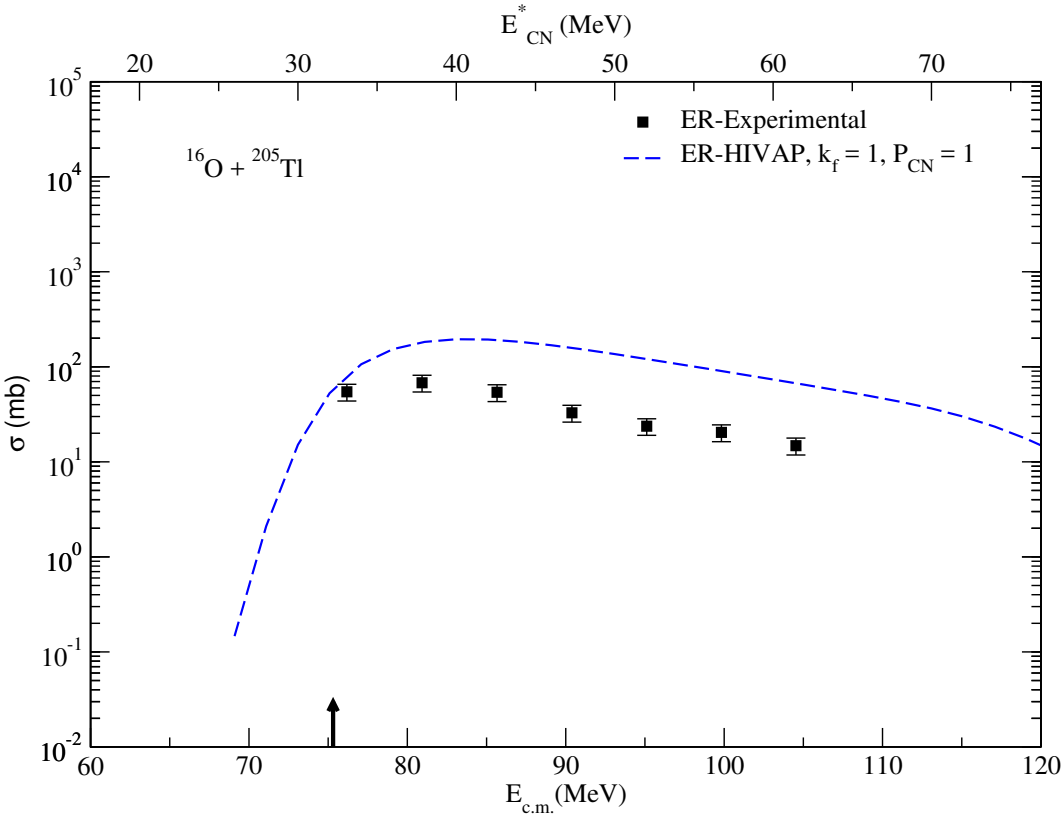

Figure 4.5: Experimental ER cross-sections for ^{16}O + ^{205}Tl reaction along with HIVAP calculations.

NCNF is usually not expected in reactions induced by ^{16}O and projectiles lighter than it. However, a recent systematic study [22] hints that NCNF contribution may exist even in ^{16}O-induced reactions. The authors have shown the variation of $\langle P_{CN} \rangle$ with entrance channel mass asymmetry η, charge product $Z_p Z_t$ and CN fissility χ_{CN}. None of these parameters were found adequate to be used as a single scaling variable to determine $\langle P_{CN} \rangle$. They identified the approximate boundaries where $\langle P_{CN} \rangle$ starts deviating from unity. These approximate boundaries where $\langle P_{CN} \rangle$ starts deviating from unity were defined by the straight lines

$$\chi_{CN} = 0.727 - 3.9 \times 10^{-5} Z_p Z_t \tag{4.9}$$

and

$$\chi_{CN} = 0.062\eta + 0.651 \tag{4.10}$$

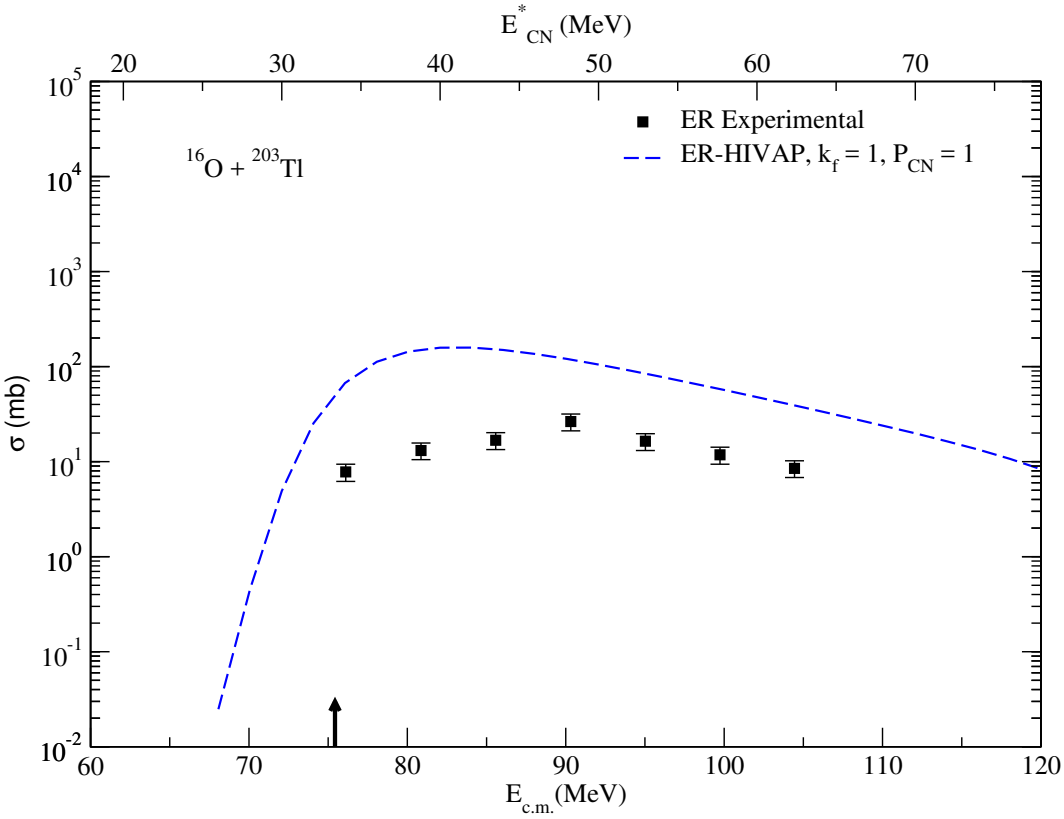

Figure 4.6: Experimental ER cross-sections for ^{16}O + ^{203}Tl reaction along with HIVAP calculations.

$\langle P_{CN} \rangle$ was found to be < 1 for the reactions located above these lines (Eqns. 4.9 and 4.10) in Z_pZ_t vs χ_{CN} and η vs χ_{CN} plots respectively for the systematics. i.e. for $\chi_{CN} >$ Eqns. 4.9 and 4.10, there is a presence of NCNF speculated. The presently measured reactions ^{16}O + ^{203}Tl and ^{16}O + ^{205}Tl, with $Z_pZ_t = 648$, $\chi_{CN} = 0.758$, 0.755 and $\eta = 0.854$ and 0.855, respectively, lie beyond these boundaries, indicating a probable contribution from NCNF. Here η is given by $\eta = \frac{|A_p - A_t|}{A_p + A_t}$, A_p and A_t being mass numbers of projectile and target, respectively. χ_{CN} is calculated using the following equation as given in reference [23].

$$\chi_{\mathrm{CN}} = \frac{Z^2}{A} \Big/ \left(\frac{Z^2}{A}\right)_{\mathrm{crit}} \tag{4.11}$$

where Z and A are atomic number and mass number of the compound nucleus, respectively and

$$\left(\frac{Z^2}{A}\right)_{\mathrm{crit}} = 50.883(1 - 1.7826\ \mathrm{I}^2) \tag{4.12}$$

where

$$I = \frac{(A - 2Z)}{A} \tag{4.13}$$

is the relative neutron excess of the compound nucleus.

In order to quantify the contribution from NCNF, we followed a method similar to the one prescribed by Sagaidak *et al.* [21]. The two reactions ^{12}C + ^{209}Bi [24–26] and ^{16}O + ^{205}Tl, produce the same CN, ^{221}Ac. The fission barrier scaling factor k_f is fixed using the asymmetric reaction ^{12}C + ^{209}Bi, where NCNF is least expected. The experimental cross-sections are in considerable agreement with HIVAP calculations with $k_f = 0.9$, $P_{CN} = 1$ (Fig. 4.7). In most of these measurements [25, 26], projectile energy was reduced using thick degrader foils, thereby causing large uncertainties in projectile energy at lower energies.

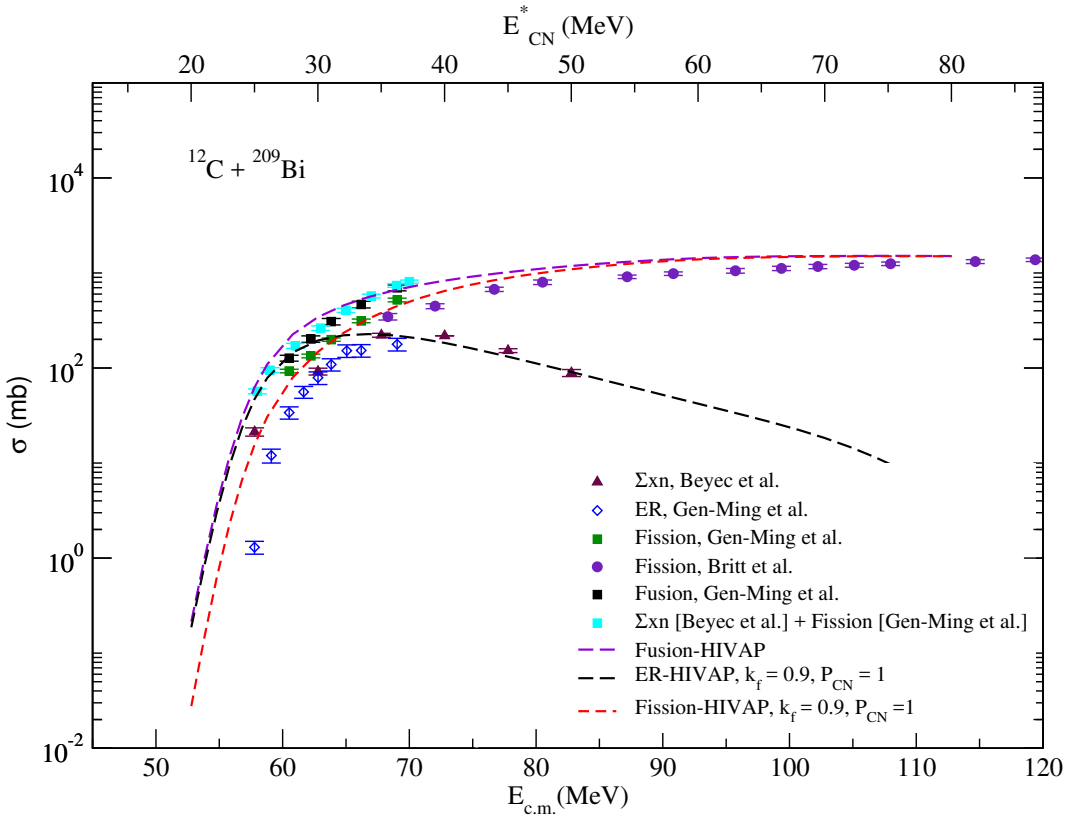

Figure 4.7: Experimental ER and fission cross-sections for ^{12}C + ^{209}Bi reaction (Beyec *et al.* [24], Gen-Ming *et al.* [26], Britt *et al.* [25]) along with HIVAP calculations.

We calculated the ER cross-section for ^{16}O + ^{205}Tl with the same fission barrier scaling ($k_f = 0.9$, similar to ^{12}C + ^{209}Bi reaction). However P_{CN} =1 is not able to explain the observed ER cross-section. A value $P_{CN} = 0.6$ is able to reproduce

the experimental results very well (Fig. 4.8). Since the ^{16}O + ^{203}Tl and ^{16}O + ^{205}Tl systems are very nearly identical, we took the same barrier scaling for ^{16}O + ^{203}Tl also and extracted the similar value of P_{CN} (Fig. 4.9).

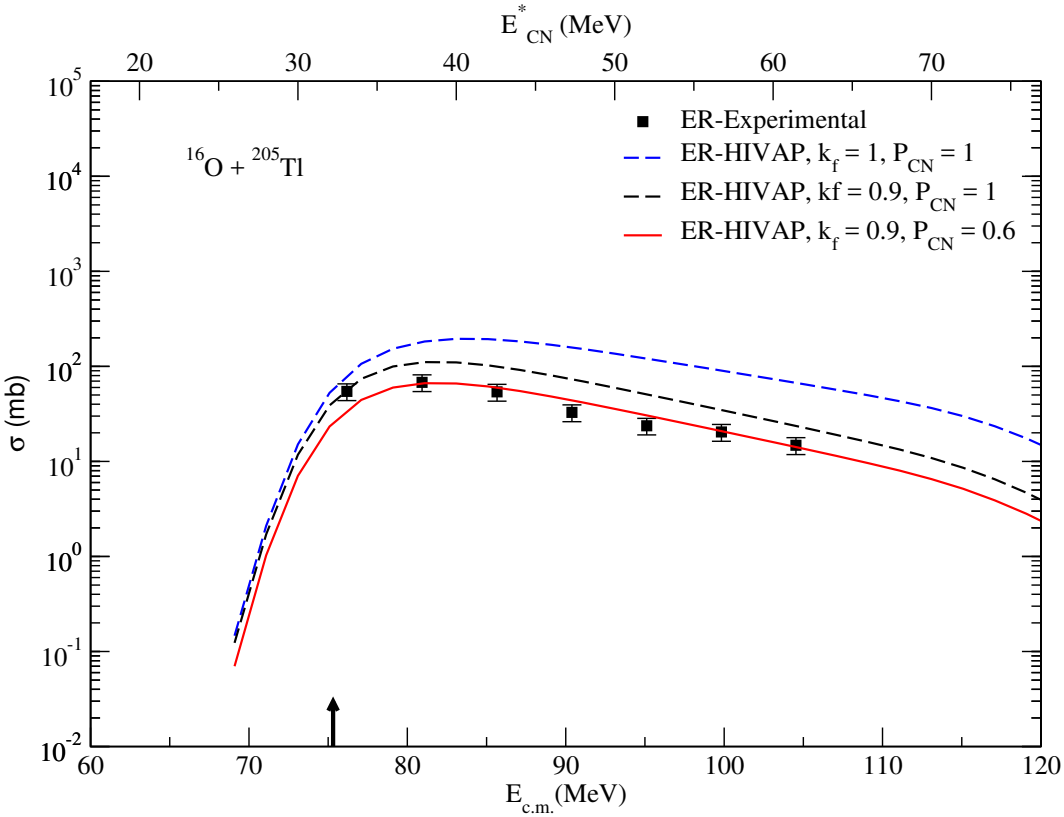

Figure 4.8: Experimental ER cross-sections for ^{16}O + ^{205}Tl reaction along with HIVAP calculations with reduced fission barrier.

In order to see the change in P_{CN} due to change in k_f, we varied k_f for ^{12}C + ^{209}Bi reaction (keeping the HIVAP predictions within the acceptable limits of the experimental cross-sections) from 0.89 to 0.91. Calculations for ^{16}O + ^{205}Tl with $k_f = 0.89$ gives $P_{CN} \sim 0.65$ and with $k_f = 0.91$, $P_{CN} \sim 0.55$. Accordingly, we have considered $P_{CN} = 0.6 \pm 0.05$ for the systems studied.

In both cases the P_{CN} so obtained is less than 1, implying there is a possible contribution from NCNF. Considering the scarcity of such measurements with lighter beams and the poor energy definition of the projectile (^{12}C), in ^{12}C + ^{209}Bi reaction [24–26], the conclusion needs to be established by studying these reactions using other probes. Also more studies are required on few other systems to unambiguously establish the contribution from NCNF.

One can notice in Fig. 4.8 and Fig. 4.9, that the measured cross-sections for ^{16}O + ^{205}Tl agree with the HIVAP ($k_f = 0.9$, $P_{CN} = 0.6$) predictions, for all energies studied

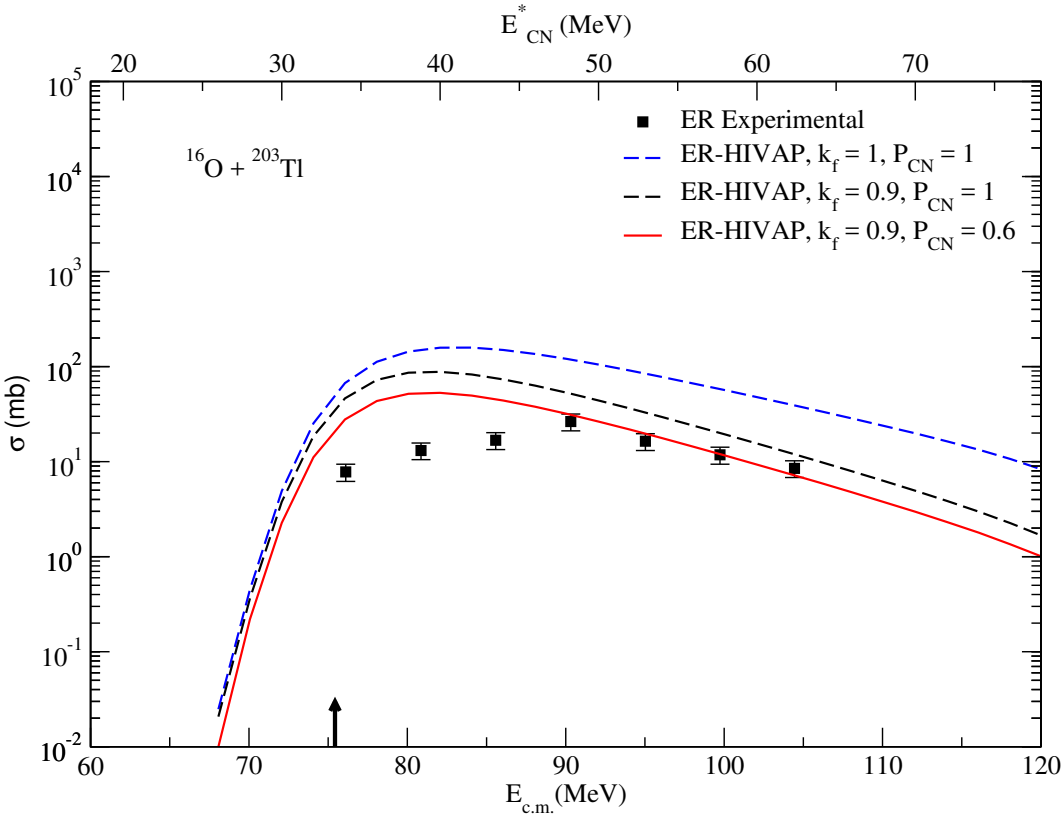

Figure 4.9: Experimental ER cross-sections for ^{16}O + ^{203}Tl reaction along with HIVAP calculations with reduced fission barrier.

while the measured values for ^{16}O + ^{203}Tl are substantially less than statistical model predictions near the Coulomb barrier energies. Also, one can infer from Table 4.5, the experimental ER cross-section for ^{16}O + ^{203}Tl is significantly lower than that of ^{16}O + ^{205}Tl near the Coulomb barrier energies. Though more studies are needed to understand this difference in this energy region, we find similar examples in the literature [3, 27, 28]. When we compare the ER cross-sections of ^{16}O + ^{208}Pb [3, 28] with that of ^{16}O + ^{204}Pb [27], we see a similar dip in the ^{16}O + ^{204}Pb case near the Coulomb barrier. The reduced ER cross-sections for both these systems are shown in Fig. 4.10, and one could observe this similar deviation between ^{16}O + ^{204}Pb and ^{16}O + ^{208}Pb.

4.3.1 Comparison with the nearby systems

We have made a comparison (Fig. 4.10) of reduced ER cross-sections ($\widetilde{\sigma}_{ER} = \frac{\sigma_{ER}}{\pi\lambda^2}$) of the presently measured systems with the ^{12}C, ^{16}O and ^{19}F induced reactions in the similar mass region. Here λ is the reduced de Broglie wavelength.

Comparison of the measured systems with the neighbouring systems shows the effect of mass asymmetry in the entrance channel on σ_{ER} and a probable contribution from

NCNF. The comparison also shows that a slight change in the entrance channel or the CN properties makes a large difference in ER cross-sections. More measurements are needed to have a better understanding of nuclear reaction dynamics.

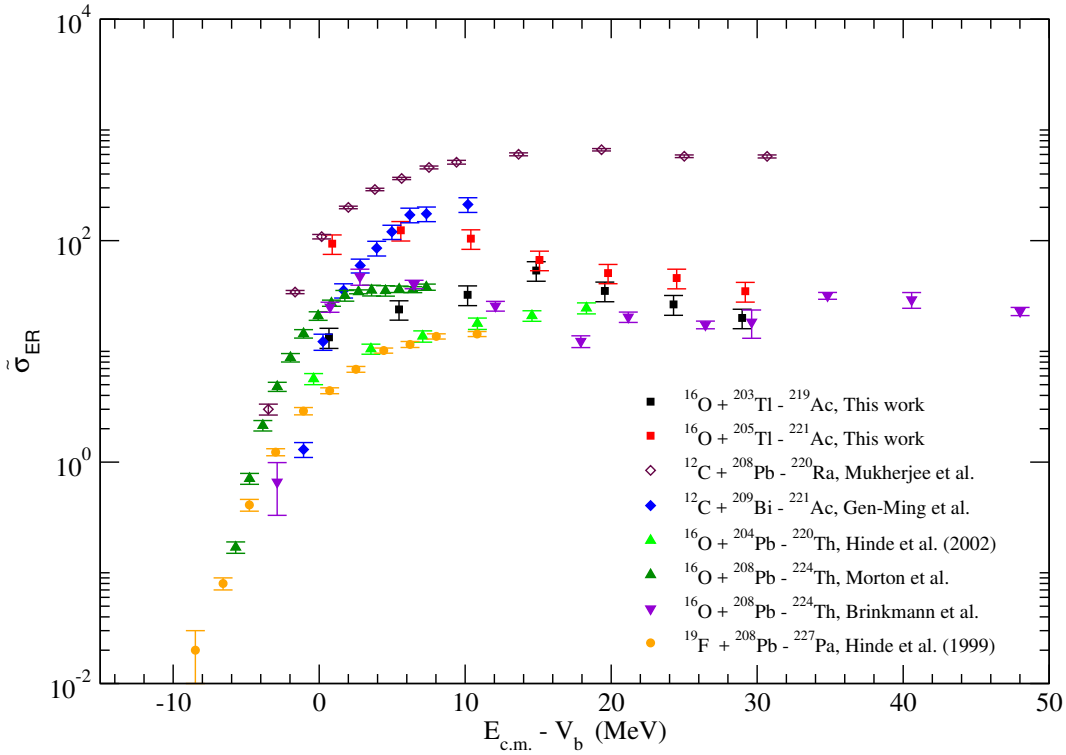

Figure 4.10: Comparison of the reduced ER cross-sections for ^{16}O + ^{203}Tl and ^{16}O + ^{205}Tl reactions with nearby systems (Brinkmann *et al.* [3], Gen-Ming *et al.* [26], Hinde *et al.*(2002) [27], Morton *et al.* [28], Hinde *et al.*(1999) [29], Mukherjee *et al.* [30]).

Bibliography

[1] S. Nath, P. V. M. Rao, S. Pal, J. Gehlot, E. Prasad, G. Mohanto, S. Kalkal, J. Sadhukhan, P. D. Shidling, K. S. Golda, A. Jhingan, N. Madhavan, S. Muralithar, and A. K. Sinha, Phys. Rev. C **81**, 064601 (2010).

[2] P. D. Shidling, N. M. Badiger, S. Nath, R. Kumar, A. Jhingan, R. P. Singh, P. Sugathan, S. Muralithar, N. Madhavan, A. K. Sinha, S. Pal, S. Kailas, S. Verma, K. Kalita, S. Mandal, R. Singh, B. R. Behera, K. M. Varier, and M. C. Radhakrishna, Phys. Rev. C **74**, 064603 (2006).

[3] K.-T. Brinkmann, A. L. Caraley, B. J. Fineman, N. Gan, J. Velkovska, and R. L. McGrath, Phys. Rev. C **50**, 309 (1994).

[4] O.B.Tarasov and D.Bazin, Nucl. Instr. and Meth B **266**, 4657 (2008).

[5] A. Gavron, Phys. Rev. C **21**, 230 (1980).

[6] E. Prasad, K. M. Varier, N. Madhavan, S. Nath, J. Gehlot, S. Kalkal, J. Sadhukhan, G. Mohanto, P. Sugathan, A. Jhingan, B. R. S. Babu, T. Varughese, K. S. Golda, B. P. Ajith Kumar, B. Satheesh, S. Pal, R. Singh, A. K. Sinha, and S. Kailas, Phys. Rev. C **84**, 064606 (2011).

[7] G. Mohanto, N. Madhavan, S. Nath, J. Gehlot, I. Mukul, A. Jhingan, T. Varughese, A. Roy, R. K. Bhowmik, I. Mazumdar, D. A. Gothe, P. B. Chavan, J. Sadhukhan, S. Pal, M. Kaur, V. Singh, A. K. Sinha, and V. S. Ramamurthy, Phys. Rev. C **88**, 034606 (2013).

[8] V. Singh, B. R. Behera, M. Kaur, A. Kumar, K. P. Singh, N. Madhavan, S. Nath, J. Gehlot, G. Mohanto, A. Jhingan, I. Mukul, T. Varughese, J. Sadhukhan, S. Pal, S. Goyal, A. Saxena, S. Santra, and S. Kailas, Phys. Rev. C **89**, 024609 (2014).

[9] R. Sandal, B. R. Behera, V. Singh, M. Kaur, A. Kumar, G. Kaur, P. Sharma, N. Madhavan, S. Nath, J. Gehlot, A. Jhingan, K. S. Golda, H. Singh, S. Mandal, S. Verma, E. Prasad, K. M. Varier, A. M. Vinodkumar, A. Saxena, J. Sadhukhan, and S. Pal, Phys. Rev. C **91**, 044621 (2015).

[10] K. Sudarshan, R. Tripathi, S. Sodaye, S. K. Sharma, P. K. Pujari, J. Gehlot, N. Madhavan, S. Nath, G. Mohanto, I. Mukul, A. Jhingan, and I. Mazumdar, Phys. Rev. C **95**, 024604 (2017).

[11] A. Shamlath, E. Prasad, N. Madhavan, P. V. Laveen, J. Gehlot, A. K. Nasirov, G. Giardina, G. Mandaglio, S. Nath, T. Banerjee, A. M. Vinodkumar, M. Shareef, A. Jhingan, T. Varughese, D. Kumar, P. S. Devi, Khushboo, P. Jisha, N. Kumar, M. M. Hosamani, and S. Kailas, Phys. Rev. C **95**, 034610 (2017).

[12] P. Sharma, B. R. Behera, R. Mahajan, M. Thakur, G. Kaur, K. Kapoor, K. Rani, N. Madhavan, S. Nath, J. Gehlot, R. Dubey, I. Mazumdar, S. M. Patel, M. Dhibar, M. M. Hosamani, Khushboo, N. Kumar, A. Shamlath, G. Mohanto, and S. Pal, Phys. Rev. C **96**, 034613 (2017).

[13] W. Reisdorf, Z. Phys. A **300**, 227 (1981).

[14] W. Reisdorf and M. Schadel, Z. Phys. A **343**, 47 (1992).

[15] http://www.nndc.bnl.gov/ .

[16] R. Bass, Lect. Notes Phys. **117**, 281 (1980).

[17] A. B. Quint, W. Reisdorf, K. H. Sehmidt, P. Armbruster, F. P. Hessberger, S. Hofmann, J. Keller, G. Munzenberg, H. Stelzer, H.-G. Clerc, W. Morawek, and C. C. Sham, Z. Phys. A **346**, 119 (1993).

[18] R. N. Sagaidak, in Proceedings of the International Con- ference on Shells-50, Dubna, 1999, edited by Yu. Ts. Oganes- sian and R. Kalpakchieva World Scientific, Singapore, 2000, p. 199. .

[19] A. V. Ignatyuk, G. M. Smirenkin, and A. Tishin, [Sov. J. Nucl. Phys. 21, 255, 1975], Yad. Fiz. **21**, 485 (1975).

[20] G. Audi and A. Wapstra, Nucl. Phys. A **595**, 509 (1995).

[21] R. N. Sagaidak, G. N. Kniajeva, I. M. Itkis, M. G. Itkis, N. A. Kondratiev, E. M. Kozulin, I. V. Pokrovsky, A. I. Svirikhin, V. M. Voskressensky, A. V. Yeremin, *et al.*, Phys. Rev. C **68**, 014603 (2003).

[22] T. Banerjee, S. Nath, and S. Pal, Phys. Rev. C **91**, 034619 (2015).

[23] J. Blocki, H. Feldmeier, and W. J. Swiatecki, Nucl. Phys. A **459**, 145 (1986).

[24] Y. Le Beyec *et al.*, Nucl. Phys. A **192**, 405 (1972).

[25] H. C. Britt and A. R. Quinton, Phys. Rev. **120**, 1768 (1960).

[26] J. Gen-Ming, X. Yuan-Xiang, Z. Yong-Tai, S. Wen-Ging, S. Xi-Jun, G. Jun-Sheng, L. Guo-Xing, Y. Ju-Sheng, S. Chi-Chang, and J. D. Garrett, Nucl. Phys. A **349**, 285 (1980).

[27] D. J. Hinde, M. Dasgupta, and A. Mukherjee, Phys. Rev. Lett. **89**, 282701 (2002).

[28] C. R. Morton, D. J. Hinde, J. R. Leigh, J. P. Lestone, M. Dasgupta, J. C. Mein, J. O. Newton, and H. Timmers, Phys. Rev. C **52**, 243 (1995).

[29] D. J. Hinde, A. C. Berriman, M. Dasgupta, J. R. Leigh, J. C. Mein, C. R. Morton, and J. O. Newton, Phys. Rev. C **60**, 054602 (1999).

[30] A. Mukherjee, D. J. Hinde, M. Dasgupta, K. Hagino, J. O. Newton, and R. D. Butt, Phys. Rev. C **75**, 044608 (2007).

Chapter 5

Summary and Conclusions

The complexity involved in the heavy ion nuclear reactions have attracted interest since several decades. The advent of heavy ion particle accelerators have paved the way to unveil various nuclear physics phenomena. The nuclear reaction dynamics is not fully understood so far especially for the heavy nuclei (A $\geq$ 200 amu). In heavy mass region like this the non compound nuclear processes overlaps with the CN processes. ERs being the true signature of CN formation can give information about non compound nuclear processes and shell effects. We have measured ER cross section for two reactions ^{16}O + ^{203,205}Tl.

For this study, isotopic targets of ^{203}Tl and ^{205}Tl of thickness 156 - 175 μg/cm^2 were prepared successfully on thin carbon backing. X-ray fluorescence (XRF) and Rutherford back scattering (RBS) techniques were used for detecting contaminations if any. Except for carbon and oxygen, no other elements were detected. Carbon contamination was due to the backing foil and oxygen because of the oxidizing nature of Tl. However, these small contaminations did not pose any problem for the measurements, as the gas filled separator used in these measurements, could very well separate the ERs and the products arising due to the fusion of beam with these impurities. XRF technique was used to estimate thickness of the targets.

The heavy ion reaction measurements with the fabricated Thallium targets have been performed at the 15 UD tandem accelerator facility of IUAC, New Delhi. We have studied the nuclear reactions ^{16}O + ^{203}Tl and ^{16}O + ^{205}Tl to obtain the evaporation residue cross sections in the range of 82-113 MeV energy i.e. near and above the Coulomb barrier using the gas-filled recoil separator HYRA. A pulsed beam of ^{16}O with lab energies in the range of 82–113 MeV have been used in present measurements. Two SSBD monitor detectors placed in the target chamber, at 25° with respect to the beam direction, were used for beam centering and absolute normalization of ER cross section. First stage of the HYbrid Recoil mass analyzer operated in gas filled mode is used to

separate the ERs from the beam like and other background particles. To record the ERs, an MWPC followed by a double-sided silicon strip detector is used at the focal plane of HYRA. Energy loss ΔE of the ERs is recorded from MWPC cathode. ERs could be selected by making coincidence plot of ΔE vs TOF.

As a first attempt with our setup, we tried to identify individual ER channel separately via alpha decay tagging using DSSD. However, it was not possible to identify individual ER channels separately due to some technical limitations, e.g. ERs produced at certain beam energies could not reach to the detector medium due to huge energy loss in its dead layer. Moreover, it was not possible to distinguish the ERs, their alpha decay or the delayed alpha decay of previously embedded ER (inside DSSD), as the alpha decay energies in these nuclei are very close lying. With the present detector and electronics resolution, it was not possible to unambiguously identify individual ER channel or their alpha decay. Therefore the individual ER channel cross sections could not be evaluated.

The transmission efficiency of the separator, required for cross section estimation, was obtained by scaling it from a nearby similar reaction ^{16}O + ^{197}Au producing the CN ^{213}Fr. The efficiency for the calibration reaction was experimentally obtained using the ER cross section data from the literature. This efficiency was scaled to the presently measured reactions by comparing the fractions of their respective ER angular distributions entering the geometrical acceptance of HYRA.

The population of alpha decaying ERs may affect the measurement of ER cross sections if they have half lives less than their time of flight through the separator. Statistical model code HIVAP is used to obtain the major ER channels and their relative populations in the considered energy range for the studied reactions. It is found that the ERs produced in ^{16}O + ^{203}Tl reaction have sufficient half lives to reach the focal plane of the separator. However, in case of ^{16}O + ^{205}Tl, at lower energies, a significant number of ERs have half lives much less than their average times of flight through the separator. Such an ER decays in flight and the recoil push given by the decay alpha deflects the residual ER from its path, and hence reduces its transmission through the separator. Transmission loss of such ERs is estimated logically, considering their relative populations, respective half-lives and the TOFs through the separator. This transmission loss is accounted for in the final transmission efficiency for ER cross section estimation. Such a treatment of short lived alpha decaying ERs is done for the first time for our setup.

The measured ER cross sections are compared with the theoretical calculations using the HIVAP code which incorporates a potential-barrier passing model with standard statistical model. These calculations overestimate the evaporation residue cross sec-

tions. A fission barrier reduction reproduce the experimental cross section. Therefore the fission barrier scaling factor k_f was fixed at 0.9, by reproducing the ER, fission and fusion cross sections of the reaction $^{12}C + ^{209}Bi$ forming the CN ^{221}Ac, same as that produced in the reaction $^{16}O + ^{205}Tl$. By introducing the fission barrier scaling factor $k_f = 0.9$ and compound nucleus formation probability $P_{CN} = 0.6$, HIVAP calculations agree with the experimental values for both the reactions in the present study. This suggests that significant contribution from non compound nuclear fission processes are probably responsible for the observed evaporation residue cross section reduction. In most of the reported measurements for $^{12}C + ^{209}Bi$, projectile energy was reduced using thick degrader foils, thereby causing large uncertainties in projectile energy at lower energies. Considering this as well as the shortage of such measurements, aimed at non compound nuclear fission using lighter beams, more studies in the same line will be useful.

A comparison of the presently measured systems was done with the ^{12}C, ^{16}O and ^{19}F induced reactions in the similar mass region. Comparison of reduced evaporation residue cross sections with neighbouring systems shows that a slight change in the entrance channel or in the properties of compound nucleus makes a significant difference in the observed cross sections. More studies are further required to get a thorough picture of non compound nuclear fission contribution and the physics there of.

In a heavy ion nuclear reaction, the statistical and dynamical aspects of fusion-fission process can be explained by studying the evaporation residues and fission products formed in the reaction. Therefore, for the sake of completeness, the measurements on fission fragment distributions of the presently studied systems will be carried out. An experimental run for these measurements is already sanctioned at IUAC, New Delhi. Other studies like spin distribution or transfer measurements for the same systems may be useful.

Moreover, due to the technical difficulty in unambiguous identification of individual ERs, the individual ER cross section could not be measured in the first attempt. A second attempt to this problem, with an improved setup in future, can give useful information about the stabilizing effects of $N = 126$ shell closure, if any.

As discussed in the thesis, the transmission efficiency of the separator is a very important factor in the estimation of absolute ER cross sections. It depends on several experimental parameters such as entrance channel mass asymmetry, beam energy, geometrical acceptance of the separator, target thickness (due to multiple scattering), helium gas pressure in the separator, focal plane detector size, and presence of some short-lived isomers. The experimental measurement of transmission efficiency, via characteristic

gamma detection, requires coincidence measurements which needs longer beam time and sometimes faces the problem of background at the target site. The method of scaling the efficiency from a nearby system requires a suitable calibration reaction with measured cross section, which may not be possible always. Hence, a Monte Carlo simulation of the transmission efficiency for the present setup will be ideal. This will require an event by event treatment of ERs in gas filled magnetic region considering all possible aspects.

With the acquired knowledge in fabrication and testing the multi wire proportional counters, there is a plan to develop a time of flight system at the focal plane of the separator which will upgrade the detection system.